

DISSERTATION

Multiscale Modeling of Ion Implantation Damage in Silicon

ausgeführt zum Zwecke der Erlangung des akademischen Grades
eines Doktors der technischen Wissenschaften

unter der Leitung von
a.o.Univ.Prof. Dr. Gerhard Hobler
am Institut für Festkörperelektronik
E362

eingereicht an der Technischen Universität Wien
Fakultät für
Elektrotechnik und Informationstechnik

von

Dipl. Ing. Kovač Dalibor
Matrikelnummer 0425115
Suchenwirtplatz 9/33 1100 Wien

Wien, im April 2007.

Kurzfassung

Obwohl Ionen-Implantation eine gut etablierte Dotierungstechnik ist, werden dabei unweigerlich Schäden generiert, die das Dopanden-Profil während der Ionenimplantation und in nachfolgenden Ausheilen verändern. Während des Ausheilens trägt der Schaden zum Clustern der Dopanden bei und führt zu vorübergehend beschleunigter Diffusion, was nur mit Hilfe eines genauen Modells der Gitterschäden vorausgesagt werden kann. Es gibt mehrere Standard-Simulationsmodelle für die Simulation des Ionen-Implantations-Prozesses, von quantum-mechanischem ab-initio, Molekular-Dynamik (MD), Binary-Collision (BC), kinetischem Monte-Carlo, bis zu Kontinuumsmodellen. Jedoch kann kein einzelner Simulationsansatz den gesamten Prozess alleine simulieren. Um dieses Problem zu lösen, ist es wichtig, die bestehenden Methoden zu verbessern und in einem hierarchischen Schema für die verschiedenen Stadien des Prozesses zu kombinieren. Das Ziel dieser Dissertation ist es, den Umfang der quantitativ modellierbaren Probleme zu erweitern, bestehende Methoden zu kombinieren und neue Ansätze vorzustellen.

Um den Amorphisierungs-Prozess bei der Implantation schwerer Ionen zu erklären, wird ein Modell für amorphe Einschlüsse präsentiert. Das Modell benutzt Binary-Collision-Simulation, um die räumliche Verteilung der abgegebenen Energie zu erzeugen, sowie die numerische Lösung der Wärmeleitungsgleichung zur Beschreibung des Abkühlungsprozesses. Die Wärmeleitungsgleichung wird modifiziert, um die Schmelzwärme zu berücksichtigen, falls die Schmelztemperatur an eine beliebigen Ort im Raum überschritten wird. Der Raum wird durch Verwendung der Finite-Volumen-Methode diskretisiert, wobei die Gitterpunkte mit den kristallographischen Gitterplätzen übereinstimmen, was eine Lösung der Anfangsbedingungen und der resultierenden amorphen Zonen auf atomarer Ebene ermöglicht. Atome werden als geschmolzen betrachtet, falls sowohl das Atom als auch die vier nächsten Nachbarn die Schmelztemperatur überschreiten. Darüber hinaus wird der lokale Zusammenbruch des Gitters berücksichtigt, sobald die Schädigung einen Schwellwert überschreitet. Aus den erhaltenen

Ergebnissen kann geschlossen werden, dass das Berücksichtigen des Gitterzusammenbruchs bei Überschreiten eines kritischen Wertes der Schädigung eine entscheidende Rolle für den Amorphisierungsprozess spielt. Die Ergebnisse, die mit Hilfe dieses Modells erzielt wurden, stimmen sehr gut mit veröffentlichten, experimentellen Daten von P, As, Te und Tl-Implantation in Si und mit Daten zum poly-atomaren Effekt bei kryogenen Temperaturen überein.

Im Rahmen dieser Dissertation wurde ein Code zur Simulation von Rutherford-Rückstreuung-Spektrometrie mit Channeling (RBS/C) geschrieben. Der Code nützt das Prinzip der close-encounter-probability (Wahrscheinlichkeit, dass sich das Atom nahe der ungestreuten Ionentrajektorie befindet) und die Rutherford-Streuquerschnitte. Um das Schadens-Modell für die Interpretation der simulierten RBS/C Spektren zu verbessern, wird ein neues, atomistisches Schadens-Modell vorgeschlagen. Mittels klassischer Molekular-Dynamik-Simulation und ab-initio Rechnungen bestimmen wir sowohl die Koordinaten des split- $\langle 110 \rangle$ Interstitials, der zwei-, drei, und vier-Interstitial-Cluster, des tetrahedrischen Interstitials, als auch die Verzerrung der Nachbaratome, die durch die Anwesenheit dieser Defekte hervorgerufen wird. Durch Verwendung dieser Koordinaten in Binary-Collision-Simulationen von RBS/C Spektren wird der Einfluss der Berechnungsmethode, der Kanalrichtung und des Defektyps auf die RBS/C Ausbeute untersucht. Die Variation der rückgestreuten Ausbeute mit dem angenommenen Defekt-Typ ist größer mit den Defekt-Koordinaten, die mittels empirischem Potential erhalten wurden, als mit den durch ab-initio Rechnung ermittelten. Die Simulationsergebnisse veranschaulichen sowohl den Einfluss der verzerrten Regionen rund um die Defekte, als auch die Wichtigkeit des korrekten Defekt-Modells in der multi-axialen Analyse von Si. Darüber hinaus wurde der Effekt der wechselseitigen Defekt-Beeinflussung als Funktion der Defekt Konzentration für alle verfügbaren Defekt-Typen untersucht. Die Schlussfolgerung daraus ist, dass das Modell basierend auf Punktdefekten und den umgebenden, verzerrten Regionen bis zu einer Konzentration von 6-7% der atomaren Dichte von Si verwendet werden kann. Das vorgeschlagene Modell verbessert die physikalische Beschreibung von Schäden in Si mit einem geringen Niveau an Unordnung und könnte für die Modellierung von leichten Implantationschäden benutzt werden.

Abstract

Although ion implantation is a well-established doping technique, it inevitably leads to damage generation, which affects dopant profiles during the ion implantation process as well as during the post-implant annealing step. Upon annealing, the damage contributes to dopant clustering and results in transient enhanced diffusion, which can only be predicted with an accurate damage accumulation model. Beside undoubted success achieved in the field of damage modeling, many processes are not quantitatively modeled up to date. A variety of standard simulation models is widely used for the simulation of the ion implantation process, from quantum mechanical ab-initio, molecular dynamics (MD), binary collision (BC), kinetic Monte Carlo (kMC) to continuum models. But, no single simulation approach can simulate the whole process alone. In order to solve this problem it is important to improve and combine existing methods in a hierarchical scheme at different stages of process evolution. The aim of this thesis is to extend the range of problems which can be modeled quantitatively, combining the available and proposing new simulation methods.

In order to explain the amorphization process upon heavy ion implants an amorphous pocket model is proposed. The model uses binary collision simulations to generate the spatial distribution of deposited energy and the numerical solution of the heat transport equation to describe the quenching process. The heat equation is modified to consider the heat of melting when the melting temperature is crossed at any point in space. Space is discretized with the finite volume method on grid points that coincide with the crystallographic lattice sites, what allows us to resolve the initial conditions and the resulting amorphous zones at the atomic level. Atoms are assumed to be molten if the atom as well as its four nearest neighbors cross the melting temperature. In addition the local collapse of the crystal lattice once the damage level exceeds a threshold is taken into account. From the obtained results it can be concluded that considering the local lattice collapse when a damage level exceeds a threshold plays a crucial role for the amorphization process. The results obtained with this model are in

very good agreement with published experimental data on P, As, Te and Tl implantations in Si and with data on the polyatomic effect at cryogenic temperature. Compared to the molecular dynamics approach the proposed model has the advantage of being capable to cover a much wider implant energy range with much lower computational cost.

Within the framework of the thesis a Rutherford backscattering spectrometry channeling (RBS/C) simulation code has been written. The code uses the principle of the close encounter probability and the Rutherford scattering cross section. In order to improve the damage models used for the interpretation of simulated RBS/C spectra a new atomistic model of damage is proposed. Using classical molecular dynamics simulations and ab-initio calculations we determine the coordinates of the split- $\langle 110 \rangle$ interstitial, of the di-, tri-, and four-interstitial cluster, and of the tetrahedral interstitial as well as the strain on neighboring atoms induced by the presence of these defects. Introducing these coordinates in binary collision simulations of RBS/C spectra we investigate the influence of the calculation method, of the channeling direction, and of the defect type on RBS/C yield. We show that the RBS/C yield calculated from empirical potentials may significantly deviate from that obtained using atomic coordinates from ab-initio calculations. The variation of the backscattering yield with the assumed defect type is larger with the defect coordinates obtained by the empirical potential than by the ab-initio calculations. The simulation results illustrate the influence of the strained regions around the defects, as well as the importance of the correct defect model in multi-axial analysis of Si. In addition the effects of mutual defect interaction versus damage concentration for all available defect types are investigated. The conclusion is that the model based on isolated point defects and their strained fields can be used up to a concentration of 6-7% of the Si atomic density. The proposed model improves the physical description of damage of Si containing low levels of disorder and could be used for modeling of light ion implant damage.

Acknowledgments

Here I would like to acknowledge all those people who helped to make this thesis possible.

I would like to thank sincerely Prof. Gerhard Hobler for giving me the opportunity to do my PhD study at the institute, for constant support, unlimited patience and many fruitful discussions.

Furthermore, many thanks to Prof. Leopold Palmetshofer, for his support and guide during the interesting experiments at JKU Linz.

Without pleasant working atmosphere, thanking to colleagues at the Solid State Electronics institute, the work could not be successful.

Thank to George Kresse for supplying the VASP code.

This work was supported by the Austrian Science Fund with project No. P15872-N08.

I also thank to my parents Danica and Ratko for their support in every sense.

Finally, I would like to thank to my girlfriend Ivana Dokić for her sincere patience and emotional support during the years.

Contents

Kurzfassung	i
Abstract	iii
Acknowledgments	v
1 Introduction	1
1.1 Motivation	1
1.2 Scope and Outline of the Thesis	3
1.3 Status of Research	4
1.3.1 Limitations of the displacement energy model	4
1.3.2 Experimental findings	6
1.3.3 Atomistic modeling	11
2 Simulation Methods	16
2.1 Introduction	16
2.2 Ab-initio methods	17
2.3 Binary Collision Approach	18
2.4 Molecular Dynamics	20
2.5 Kinetic Monte Carlo	21
2.6 Continuum models	23
2.7 Multi-scale approach	24
2.8 Conclusion	26
3 Amorphous Pockets	27
3.1 Introduction	27
3.2 Energy spikes in Si due to heavy ion bombardment	29
3.2.1 Ion mass effect	29

3.2.2	Polyatomic effect	33
3.3	Existing amorphization models	35
3.4	Amorphous pocket model based on the numerical solution of the heat conduction equation and lattice collapse	43
3.4.1	Numerical model of the heat transport equation	44
3.4.2	Program details	55
3.5	Results and discussion	67
3.5.1	Ion Mass Effect	67
3.5.2	Polyatomic effect	72
3.6	Conclusions	77
4	Rutherford Backscattering Spectroscopy	79
4.1	Introduction	79
4.2	Binary collision simulation of RBS	83
4.2.1	Trajectory of incoming particle	85
4.2.2	Rutherford scattering event	86
4.2.3	Energy loss due to Rutherford scattering	91
4.2.4	Outgoing particle path	92
4.2.5	A count in energy spectrum	95
4.3	Atomistic model of damage in RBS/C simulations	95
4.3.1	Atomic-scale defect models	96
4.3.2	Building a large supercell	99
4.4	Investigation of the impact of defect model on Monte Carlo simulation of RBS/C spectra	100
4.4.1	Computational details	102
4.4.2	Results and discussion	103
4.5	Influence of defect relaxation and mutual interaction	115
4.5.1	Introduction	115
4.5.2	Results	115
4.6	Conclusions	119
5	Conclusion and Outlook	121
A	Acronyms and Symbols	124
A.1	List of Acronyms	124
A.2	List of Frequently Used Symbols	125

Chapter 1

Introduction

1.1 Motivation

Ion implantation has been the dominant tool adopted in microelectronics industry for introducing dopants into silicon for several decades. It is unique technique for controlling the distribution of dopants and damage formation in materials by varying the ion energies, species, doses and dose rates. For example, a typical modern CMOS process employs a dozen of ion implant steps to form isolation wells, source/drains, channel-stops, threshold voltage adjusts, buried layers and other doped areas of p- and n-channel MOS transistors [1]. Short process times, good homogeneity and reproducibility of the profile and precise dose control are some of the advantages of ion implantation which promise to keep it as a mainstay in the semiconductor industry for the future.

During ion implantation the impurity ions are accelerated to energies ranging from fraction of keV up to several MeV and are directed onto the surface of the semiconductor. As the ions enter the crystal, they gave up their energy to the lattice atoms before they come to rest at some depth in the crystal. The energy loss of ions passing through matter can be divided into two components: electronic stopping (inelastic scattering with electron shells of target atoms) and nuclear stopping (elastic scattering with target atom's nuclei). However, one of the major disadvantages of implantation is lattice damage, which results from the collisions between the energetic ions and the lattice atoms. This damage can take the form of a non-equilibrium excess of vacant lattice sites (vacancies) and interstitial atoms (interstitials), vacancy or interstitial clusters,

dopant-interstitial and dopant-vacancy clusters, and locally amorphized regions of the crystalline silicon target. For sufficiently high doses continuous amorphous layers are formed. The spatial distribution and form of damage, as well as amorphous to crystalline transformation is critically dependent on the implantation parameters and is controlled by a competition between damage annealing and damage accumulation [2]. The Si substrate needs to be subsequently annealed in order to electrically activate the dopants and to repair the lattice damage. Annealing is done at temperatures high enough to allow the dopant atoms to diffuse to substitutional sites, and for the lattice defect to recombine. During annealing defects interact with the dopant atoms and induce transient-enhanced diffusion (TED) of the dopant over long distances. If they survive into the final device they can form relatively stable dislocation arrays which degrades electrical performances of devices, if they are present in active zones. In addition defects disrupt the periodicity of the crystal, introduce local strain, and result in new energy levels which are often somewhere in the bandgap, modifying the electronic structure of the material [3].

Implantation damage affects the final doping profiles in two ways, as as-implanted damage due to the dechanneling effect, and as the source for transient enhanced diffusion during the subsequent thermal annealing [1]. Thus, the modeling of the ion implantation damage process is motivated by two objectives. One is to simulate the defect dechanneling effect so that the impurity profiles as a function of dose can be predicted. The other objective is to predict the damage profiles so they can be used to quantitatively model the thermal annealing step. This has caused the 2005 edition of the International Technology Roadmap for Semiconductors [4] to identify accurate modeling of implantation damage, thermal annealing, reaction of dopant atoms and defects as one of key challenges in the field of modeling and simulation. As the size of the active area of devices shrinks a need for the understanding and modeling of the damage creation arises.

Although much research has been devoted over the years to these subjects, many questions are still under debate and quantitative modeling is in many cases not possible. For this purpose, simulation tools can be very helpful in optimizing the fabrication process of Si devices. This field is experiencing a rapid growth supported by significant increase in computing power from one side and decreasing in computer costs from the other side, which is not case for the experimental facilities.

1.2 Scope and Outline of the Thesis

The scope of this thesis is to develop simulation tools which can qualitatively and quantitatively explain physical processes closely related to ion implantation induced damage. We propose a new amorphization model based on the numerical solution of the heat transport equation and use it to investigate the ion-mass and poly-atomic effect. For the purpose of ion beam analysis and defect quantification a Rutherford backscattering spectroscopy module as a part of the binary collision Monte Carlo code IMSIL is written and tested. For quantitative interpretation of RBS/C spectra a new atomistic model of damage is developed.

The thesis is organized in the following chapters.

- **Chapter1:** Gives an overview of the status of research and introduces the standard models used in existing simulation tools. The limitation and need for the improvement of these models are briefly discussed. In addition simulation models beyond the standard models are also discussed.
- **Chapter2:** Introduces and explains simulation techniques widely used in modeling of the ion implantation process. In this Chapter the advantages and the limitations of the particular method are discussed. Since no particular approach can model the whole implantation process alone, the emphasis is on the multiscale modeling where different simulation techniques are coupled in order to overcome limitations of the particular model itself.
- **Chapter3:** Gives an overview of existing amorphization models and discuss their predictive capabilities and limitations. A new amorphization model based on the numerical solution of the heat equation to treat the heat quenching upon ion implantation is proposed. The physical background and the implemented numerical solution of the model are explained. The model is tested on the experimental data on the ion mass and polyatomic effect.
- **Chapter4:** Within the framework of the thesis a Rutherford backscattering spectrometry channeling (RBS/C) simulation code is written. The implemented RBS/C code is explained in detail. The configurations and coordinates of small interstitial clusters are calculated by molecular dynamics (MD) simulations and

ab-initio calculations. Using the results from these simulations a new atomistic model of damage is proposed. Within this approach the impact on the simulated RBS/C spectra of the particular defect type, of the calculation method, and of the beam-target alignment is investigated. The influence of mutual defect interactions at high damage concentrations is also investigated.

- **Chapter5:** The conclusion section summarizes the performed work and gives recommendations for the future work.

1.3 Status of Research

In this section we review the state of the art in modeling of as-implanted silicon damage. We start with the limitations of the standard model in Section 1.3.1. We continue with an overview of experimental findings on the dependence of the amount of damage on implant parameters (Section 1.3.2). In Section 1.3.3 recent efforts in atomistic modeling are presented.

1.3.1 Limitations of the displacement energy model

The standard model of damage formation is based on the concept of a “displacement energy”, which means that a target atom is recoiled and thus permanently displaced from its lattice site if the energy transferred to it in a collision exceeds a fixed value, the displacement energy [5]. After the recoil has lost its energy due to electronic and nuclear stopping it comes to rest in the host lattice, creating an interstitial. The distribution of displaced atoms can be calculated by simulating the collision cascades in the binary collision approach (BCA), following each recoil with energy above the displacement energy. In this approach the movement of an atom is treated as a series of successive binary collisions between the ion and the host lattice atoms. If the spatial distribution is not of interest, the number of displaced atoms can be estimated from the energy deposited into nuclear collisions using the modified Kinchin Pease formula [6]. The standard model has been applied to silicon target with limited success [7]. Investigating the dose dependence of the channeled dopant profiles various extensions to the standard model have been developed [1, 8]. In the model proposed by

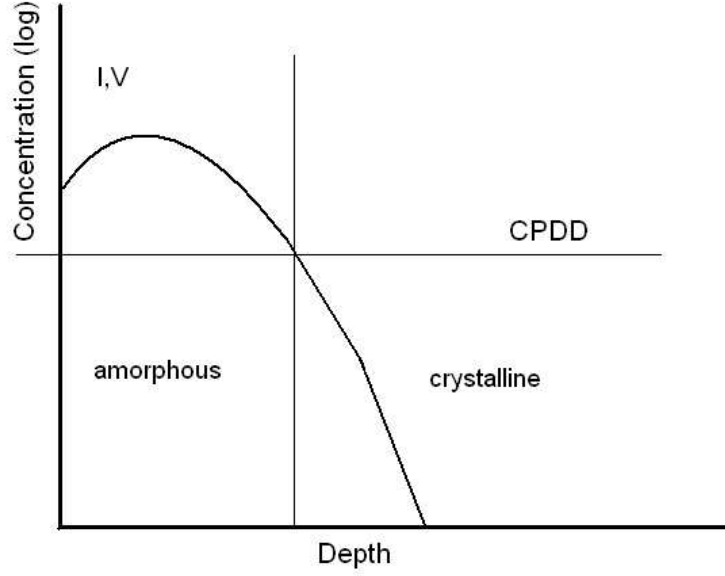


Figure 1.1: *Damage concentration as a function of depth. Critical point defect density (CPDD) determines the position of the a/c interface.*

Hobler [8] the amount of damage generated in the standard model is corrected by an empirical factor f_{rec} , which depends only on the ion species and not on other implant parameters. The factor is interpreted as describing defect recombination within a recoil cascade ($f_{rec} < 1$) or as describing the more efficient damage generation ($f_{rec} > 1$) in dense cascades due to spike effects. In the extended standard model it is assumed that the lattice turn amorphous if a critical point defect density (CPDD) was exceeded [9]. Fig. 1.1 shows a typical damage profile and the influence of the value of CPDD for the determination of the a/c interface what in turn influences the damage that remain upon thermal annealing. It is assumed that upon moderate thermal annealing the amorphous layer recrystallizes, while in non-amorphized part of the target the EOR defects remain. Due to the shape of the damage profile a small change in the CPDD value leads to a large variation in the remaining damage profile. Therefore, the CPDD determines not only the position of the a/c interface but also, the amount of the damage remaining beyond the a/c interface. The CPDD can be obtained from measured depths of amorphous layers. Beside being successful in predicting dopant profiles [8, 10, 11] the extended standard model still has limitations. First, the range

of the reported critical point defect density is uncertain within a factor of 10 [7] what influences the defect concentration as discussed above. Second, the model describes the damage in the form of Frenkel pairs (interstitials + vacancies) and is therefore not able to predict the more complex types of the damage generated, which is important for the quantitative prediction of subsequent thermal annealing [7, 12].

1.3.2 Experimental findings

1.3.2.1 Ion mass effect

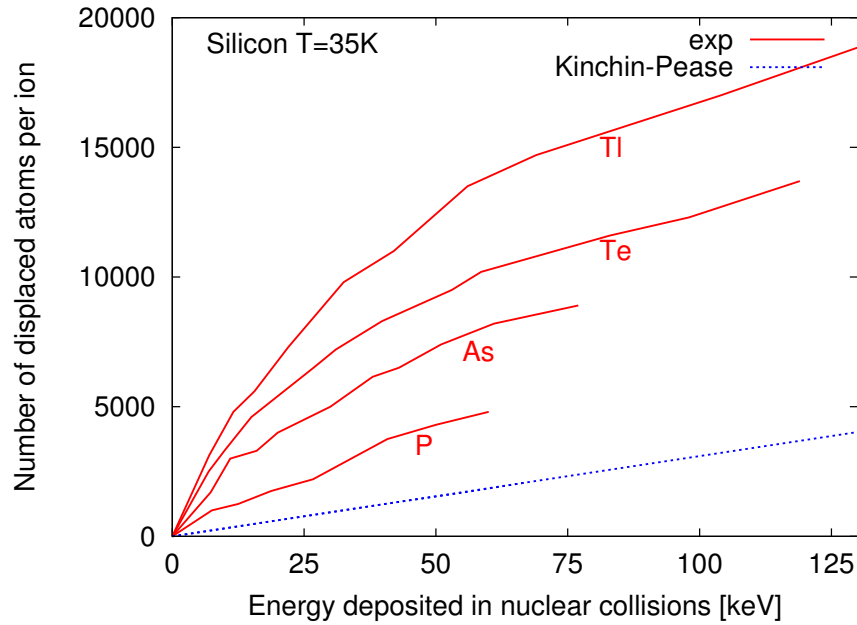


Figure 1.2: The number of displaced atoms per ion for different ion masses as function of the energy deposited in nuclear collisions [13]. Experimental results - solid lines [6]. The dashed line denotes the prediction of the modified Kinchin-Pease model [5].

At cryogenic temperatures, where dynamic annealing is assumed to be absent, it has been found that heavy ion implantation creates more damage than light ions for the same amount of the energy deposited into nuclear processes [6, 13–15]. Fig. 1.2

shows the number of displaced atoms measured by RBS/C as a function of the energy deposited in nuclear collisions, which is a monotonic function of implant energy [6]. The dotted line represents the prediction of the classical displacement energy concept calculated according to the modified Kinchin-Pease formula [5]. The discrepancy between the results predicted by the Kinchin Pease model and the experimental finding increases with ion mass, as it is shown in Fig. 1.2. The change in damage morphology is also observed by transmission electron microscopy (TEM) proving the fact that heavy ions and medium mass ions at low temperatures create amorphous pockets, while light ions and medium-mass ions at room temperature do not [16–18].

1.3.2.2 Polyatomic effect

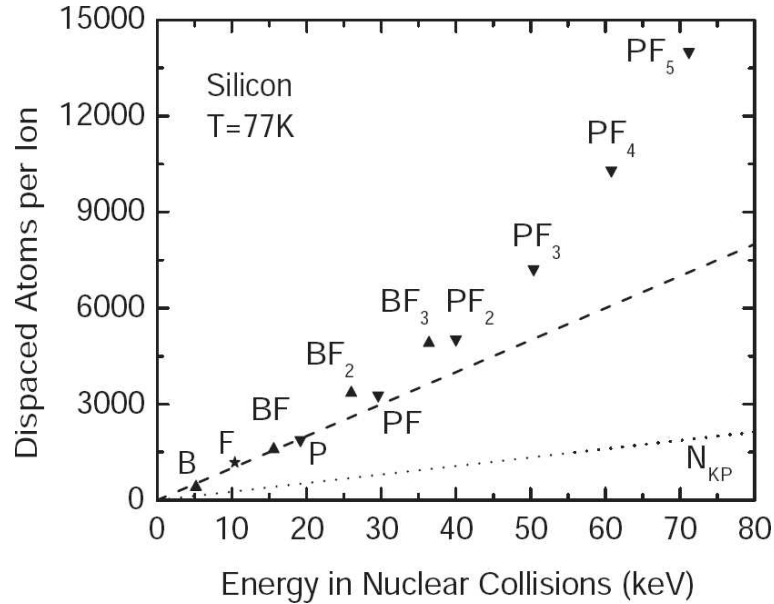


Figure 1.3: Number of displaced atoms as measured with RBS/C after implantation of B, F, BF_n ($0 \leq n \leq 3$) and PF_n ($0 \leq n \leq 5$) at 77K. The number of displaced atoms increases more than linearly (dashed line). The predictions of the standard model using the modified Kinchin Pease formula are shown by the dotted line [19].

It has been shown experimentally that poly-atomic ions cause more damage than

the same atoms implanted separately [13, 19, 20]. Fig. 1.3 shows the number of displaced atoms after BF_n ($0 \leq n \leq 3$) and PF_n ($0 \leq n \leq 5$) molecular implantations as a function of the energy deposited in nuclear collisions per molecular ion [19]. Without the polyatomic effect the number of displaced atoms per ion should increase linearly with the energy (dashed line). From Fig. 1.3 the increase in the efficiency of damage generation with increasing molecule size can be clearly seen.

1.3.2.3 Dose-rate effect

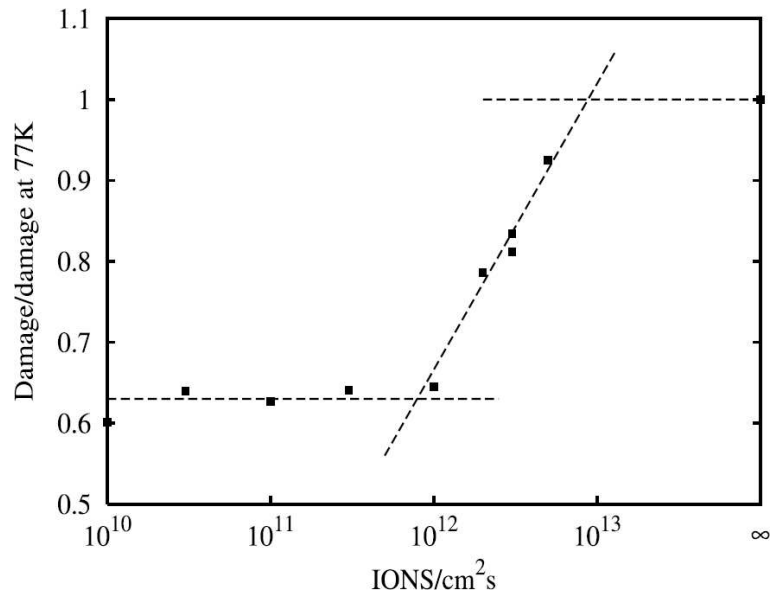


Figure 1.4: *Relative amount of damage caused by the N implantation at room temperature with respect to the LNT implant as a function of dose-rate, for a constant dose [21].*

Except at low temperatures the amount of damage increases with dose rate, generally with a power of less than 1/2. It becomes weaker with increasing ion mass [21–27]. The amount of damage created by a room temperature N implant with respect to the damage at LNT implant is presented in Fig. 1.4, illustrating the dose-rate effect. It is assumed that, for constant implantation dose, the amount of damage is independent of dose-rate at liquid nitrogen temperature (LNT).

1.3.2.4 Ion-beam induced interfacial amorphization -IBIIA

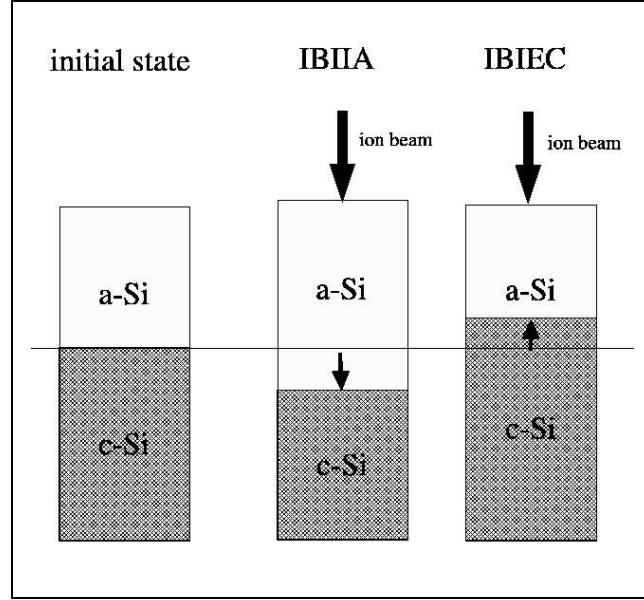


Figure 1.5: Illustration of IBIIA (ion beam induced interfacial amorphization) and IBIEC (ion beam induced epitaxial crystallization) effect [12] .

Ion beam induced interfacial amorphization (IBIIA) denotes the growth of a pre-existing amorphous layer upon ion bombardment under conditions where the ions cannot amorphize themselves an initially homogenous crystalline target [28–30]. Fig. 1.5 shows the principles of the IBIIA and its reverse effect, the ion beam induced epitaxial crystallization (IBIEC) effect. Depending on substrate temperature the amorphous layer can grow (IBIIA) or shrink (IBIEC) due to the influence of the ion beam. The conditions for ion-beam induced interfacial amorphization (IBIIA) have been extensively evaluated against its reverse effect, ion-beam induced epitaxial crystallization (IBIEC), but less attention has been paid to when IBIIA dominates over bulk amorphization [28, 31, 32].

1.3.2.5 Temperature dependence

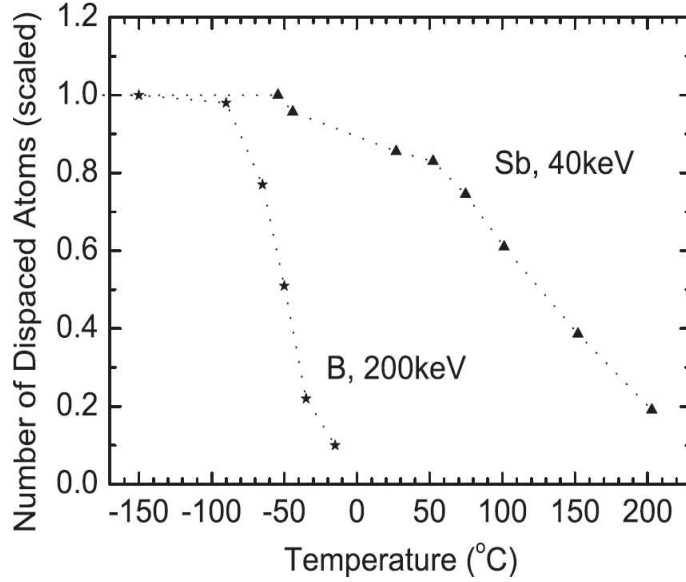


Figure 1.6: Scaled number of displaced atoms as a function of implant temperature as measured by RBS/C: 200 keV B [33] and 40 keV Sb [34].

At temperatures above ~ 150 K the amount of damage formation decreases with temperature, for light ions more rapidly than for heavy ions [33]. Fig. 1.6 shows scaled numbers of displaced atoms as a function of implant temperature measured by RBS/C for 200 keV B [33] and 40 keV Sb [34] implantations. The temperature dependence of disorder produced in Si by 200 keV B implantations is very strong from about -85° to room temperature in contrast to only slightly temperature dependent disorder produced in Si by 40 keV Sb implants. This suggests that the ion mass effect increases with temperature. A related effect is the increase of the critical temperature beyond which the target cannot be amorphized at any dose, with ion mass [35].

1.3.3 Atomistic modeling

A variety of atomistic simulation have been performed recently in order to overcome the limitations of the standard model [1, 2, 21, 36–54].

1.3.3.1 Damage morphology and distributions

MD study performed by Nordlund et al. [36] has shown that the amorphous pockets has on average a little less atoms than perfect Si. Studying the implantation damage by MD simulations M.-J. Caturla et al. have found that light ions mainly produce point defects and small clusters, while heavy ions create amorphous pockets [2]. They have also investigated the influence of the size of the amorphous zone on recrystallization and have indicated that the activation energy increase with the size of the pockets, i.e. larger pockets tend to be more stable [2]. T. Motooka has proposed a homogeneous amorphization model based on divacancy and di-interstitial (D-D) pairs to study the ion induced damage. It has been shown that the lattice becomes unstable when the concentration of D-D pairs exceeds 30% [37–39]. An atomistic approach based on a Monte Carlo diffusion code coupled to a binary collision program is used to simulate the ion implantation and annealing process [40–44]. The model proposed by L. Pelaz et al. uses the damage structures known as interstitial-vacancy (I-V) pairs or bond defects. The amorphization of material is assumed to occur when the local concentration of I-V pairs exceeds 25% [41]. Recrystallization of the I-V pairs is simulated by kMC under the assumption that the recombination energy of the I-V pair decreases as the number of neighboring I-V pairs increases. Within this model the superlinear dependence of damage accumulation with dose [41], the dependence of the recrystallization behavior on amorphous-crystal interface morphology [43] are simulated. M. Jaraiz et al. have proposed a model [40] based on the interstitial and vacancy clusters which includes the treatment of the formation and ripening of these clusters. The obtained results explain the success of the “+1” model, used to simulate diffusion of dopants after ion implantation [40]. Further model based on the damage structures known as amorphous pockets (AP), which are three dimensional agglomerates of interstitials and vacancies (I-V pairs) is proposed [55–57]. AP recrystallization rate is characterized by their effective size where larger pockets have larger activation energy what is in agreement with the MD results [2]. This model has been able to reproduce experimental observations

of the extent of the amorphous layer upon ion implantation, and the difference between the dynamic and post-cryogenic implant annealing [55, 56]. Further studies based on the coupled BC/kMC approach have been performed to study as-implanted damage [1]. On the other hand, neither of these models intended to compare its results with the experimental dependencies discussed in Section 1.3.2. Furthermore, these studies have only transferred point defects from BC to kMC simulation not taking into account the atomic structure and the correct coordinates of eventual more complicated defect types, beside I-V pairs. It is also questionable whether the whole damage accumulation and recrystallization process can be based on a single defect type like it is done in these approaches. The model proposed by G.Otto et al. uses also coupled BC/kLMC technique but considers the atom positions of each defect as well as the lattice strain around the defects in the BC simulations [12, 21, 45, 47]. This model was able to explain the temperature dependence of implantation damage around room temperature and below, the difference between dynamic annealing during the implant and post-implant annealing [45] and the dose rate effect of light ion implantation [21]. It has been also shown that the dynamic annealing during ion implantation and post-implant annealing may be modeled within this model [47]. I. Santos et al. [58] have recently proposed an improved BCA simulator based on the damage studies at the subthreshold energies performed by MD simulations. Simulating many collision cascades by MD authors have been able to assign the efficiency of the damage production for each group of atoms as a function of energy density. These results have been applied to incorporate the effect of low-energy (subthreshold) interactions in BCA models. The obtained results are rather similar with the MD results, but obtained with significantly lower computational time. On the other hand, the proposed model assumes the spherical melting what is questionable for silicon.

1.3.3.2 Atom positions of defects

One distinctive features of RBS/C is the possibility to identify atomic location of defects and host impurities by performing measurements under varying beam-target alignment conditions. The interpretation of data requires the support of Monte Carlo binary collision simulation of ion-channeling spectra. More qualitative analysis, such as the evaluation of the number of defects introduced by irradiation, requires a microscopic model of damage and its effect on the backscattering yield of the analyzing ions.

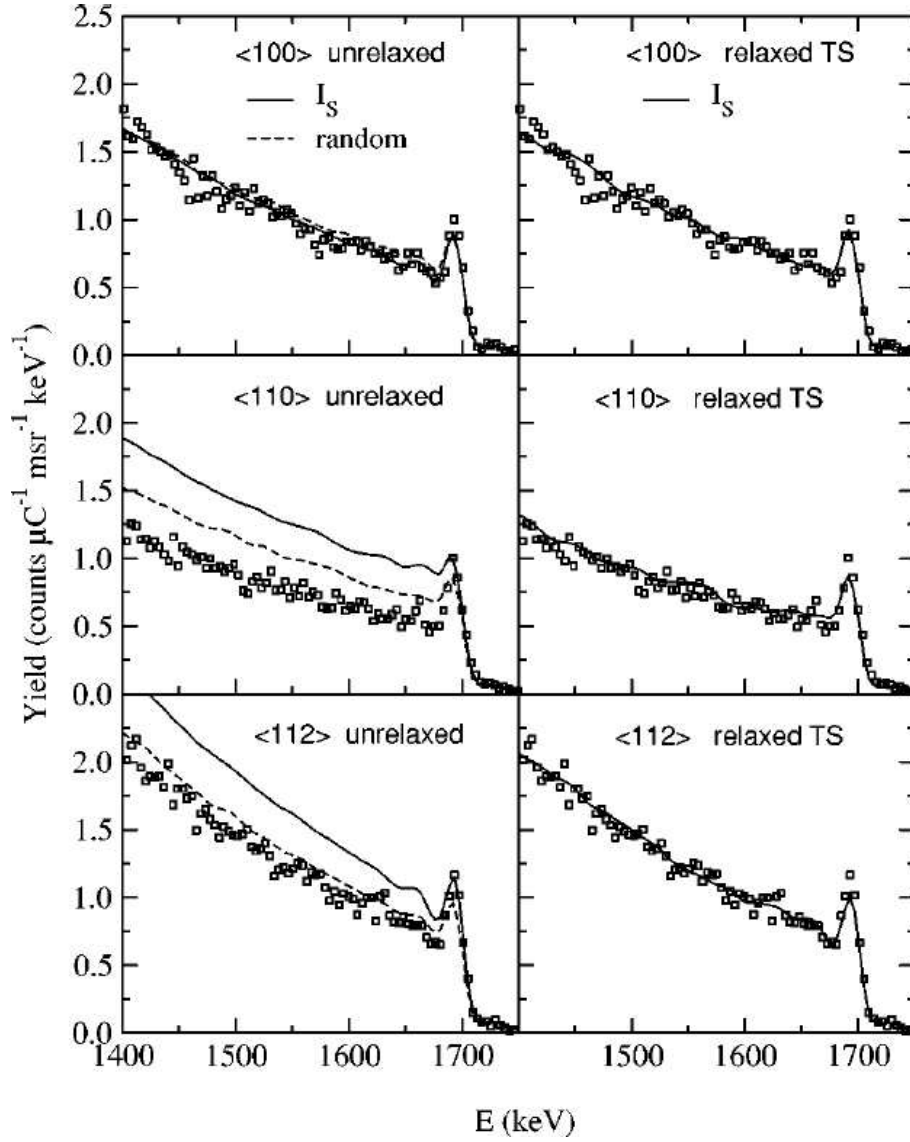


Figure 1.7: Results of the multi-axial fit of the experimental RBS/C spectra performed with different damage models, using the distribution of split- $\langle 110 \rangle$ interstitial (I_S) plus vacancies or of the randomly displaced atoms, which reproduces $\langle 100 \rangle$ spectrum. Symbols refer to the experimental spectra, lines refer to simulations [52].

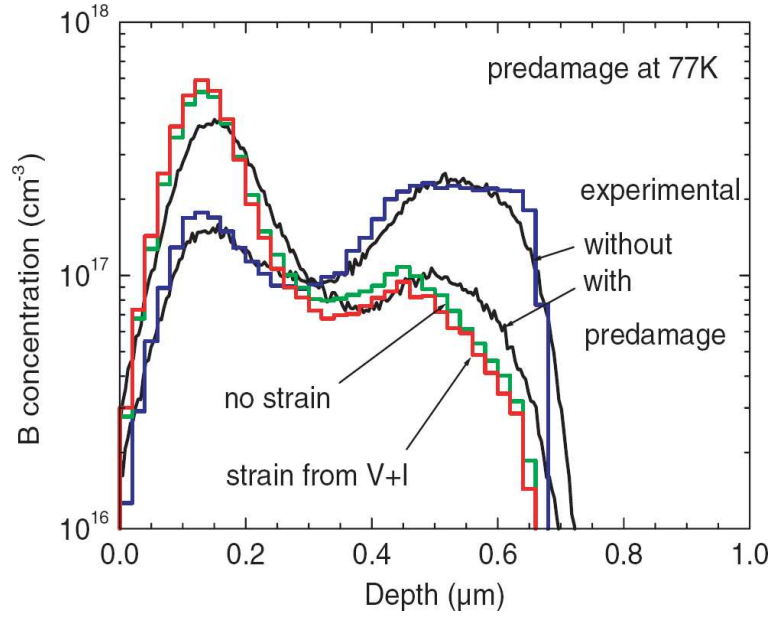


Figure 1.8: *B* profiles after 30keV channeling implantations in undamaged (110)-Si and in (110)-Si predamaged with a N implant at 77K. Continuous lines: as measured by SIMS. Histograms: simulations assuming no strain around defects and considering strain. [47].

Widely used simulation programs based on picture that damage consists of displaced atoms surrounded by the ideal lattice, suffer from a simplified, rather unphysical, description of defects [59]. A deeper physical insight into the actual location, structure and binding properties of defects to the surrounding lattice sites is indeed necessary to improve our current understanding of ion channeling experiments. Investigations in this field can take advantage of the recent great deal of atomic scale modeling of the structure of small defects [60–72]. Classical molecular dynamics (MD) simulation, based on numerical solutions of the Newton’s equations, or more computationally intensive quantum-mechanical methods (ab-initio) have been applied to determine the structure and the coordinates of the small atomic scale defects. Such calculations yield the atomic positions at strictly defined positions, corresponding to energy minima, rather than at random positions. Götz has indicated the existence of split- $\langle 110 \rangle$ interstitial upon B implantations in Si at cryogenic temperatures [73]. Using MD simulations Weber et al. [74] have shown that the lattice distortion due to a divacancy and split- $\langle 110 \rangle$ interstitial is necessary to be taken into account when fitting the multi-axial

damage experiments.

In a recently developed approach for the interpretation of RBS/C measurements [48–54] spectra were simulated by the MC-BCA method and disorder was described by atomic scale models of defects, structurally relaxed by empirical potentials. Fig. 1.7 shows the results of the multi-axial fitting of experimental RBS/C spectra performed with different damage models, the split- $\langle 110 \rangle$ and the random interstitial model [52]. A model system is built by inserting a distribution of one defect type at a time in a supercell. The results labeled by “relaxed TS” are obtained by relaxing the simulation cell with the Tersoff empirical potentials, while the results labeled by “unrelaxed” represent the case when the cell is populated with only defective atoms, neglecting the strain, without further relaxation. The experimental RBS/C spectra is fitted in $\langle 100 \rangle$ direction and then using the fitted distribution analyzed in $\langle 110 \rangle$ and $\langle 112 \rangle$ direction. A good multi-axial fitting is obtained using the relaxed split- $\langle 110 \rangle$ interstitial, while the unrelaxed split- $\langle 110 \rangle$ or random interstitial failed to reproduce the experimental spectra under the other alignment directions. Despite the success, the presented results are influenced by the empirical nature of the Tersoff potential, as we will investigate and discuss in Section 4.4. Within the model proposed by Hobler et al. the non-negligible influence of the strain induced by the presence of the small interstitial clusters is indicated by BC simulations of 30keV B channeling profile measurements (CPM) in N predamaged silicon sample [47] (See Fig. 1.8).

However, none of the above discussed models can describe all experimental findings. In order to develop more general models of damage accumulation, based not only on a single defect type, more accurate and physically correct descriptions of the as-implanted damage are required. Therefore, the goal of this thesis is to improve existing and propose new simulation methods with the help of experimental data.

Chapter 2

Simulation Methods

2.1 Introduction

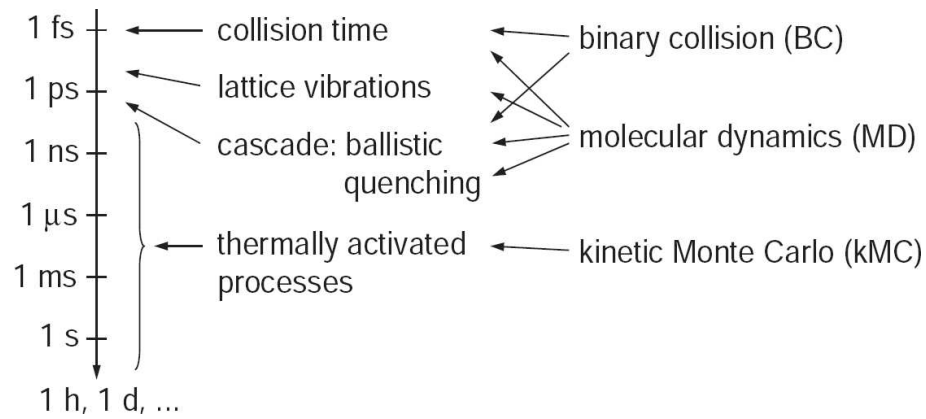


Figure 2.1: Time scales and atomistic simulation methods [7].

The understanding and modeling of ion implantation induced defects in silicon is complicated by the many parameters influencing their generation, and by the existence of many different types such as isolated point defects, point defect clusters, {311} defects, amorphous pockets, and dislocation loops. For the purpose of better understanding and optimizing the fabrication process of Si devices simulation tools can be very helpful, especially because the realization of experimental tests is often very

expensive. While the overall picture of the time evolution of ion implantation induced damage is becoming clear, many important details are not very well understood. Until these details are clarified, the goal of predicting the evolution of damage in the device fabrication will remain only partially realized.

Fig. 2.1 explains the time scales and adequate simulation techniques for the processes relevant to damage formation. In an implantation process binary collision takes on the order of 1 fs, while a full cascade develops in the picosecond time scale. The time necessary for kinetic energy given to the lattice atoms to dissipate into the crystal (quenching) is on the order of picoseconds. After all atoms have dissipated their kinetic energy, they have settled in local potential minima and further changes of the system requires additional thermal activation. The BC approach is adequate to describe spatial properties of the collision cascade, but it is not capable of simulating the quenching of the collision cascade. For that purpose the molecular dynamics method is appropriate, because it takes the many body interaction between the colliding ion and the target atoms into account. Because of the requirement to resolve lattice vibrations (which is in order of 0.1 ps) MD simulations are rather limited to treatment of processes with a duration of up to about 1 ns. For the thermally activated processes, which take place on larger time scales kinetic Monte Carlo methods are used.

In order to give a satisfying description of all physically relevant processes involved in the fabrication of Si devices it is necessary to use a variety of simulation methods from ab-initio calculations up to continuum models. Although continuum models are widely used in process simulation in the semiconductor industry, atomistic models are very useful to extract relevant process parameters like diffusivity, binding energies, etc. With decrease in the size of the semiconductor devices the role of atomistic models increases. A more detailed description of the above mentioned simulation methods is given in the following sections.

2.2 Ab-initio methods

The name *Ab-initio* is given to computations which are derived directly from theoretical principles, with no inclusion of experimental data or any fitting or artificial parameters. In ab-initio methods the Schrödinger equation is solved for the set of

nuclei and electrons of the system under study. The calculation is done using several mathematical approximations [75].

Ab-initio simulations based on the density functional approach (DFT) are the most accurate feasible method to consider small cells. The density functional theory is based on the Hohenberg-Kohn theorems, which demonstrate the existence of a one-to-one mapping between the ground state electron density and the ground state wave function of a many-particle system [76]. In this type of calculation, there is an approximate Hamiltonian and an approximate expression for the total electron density [75]. However, due to very expensive calculation manageable cell sizes have an upper limit of a few hundred or at most about thousand atoms. In addition due to the approximation made in the local density approach some results are not correct, e.g. the bandgap in semiconductors. Nevertheless, these methods give excellent insight into the physics of the system and can calculate some physical quantities which can be later used as input in other simulation methods, like the energies and coordinates of atomic-scale defects in silicon [77, 78] and the energy barriers between different defect configurations. These informations can be further used to define event rates in Kinetic Monte Carlo methods [45], defect types in BC-MC codes [47] or for interpretation of RBS/C results [77].

We have performed our density functional calculation with the VASP code, written by Kresse and Furthmüller. It uses the projector augmented-wave method, which allows reduction of required basis set. A more detailed description of the physical model implemented in VASP can be found in [79, 80].

2.3 Binary Collision Approach

The Monte Carlo binary collision approximation (MC-BCA) has been conventionally used to describe the slowing down and scattering of energetic ions in materials. The BC approach has a number of advantages over analytical formulations based on transport theory. It allows a more rigorous treatment of elastic scattering, explicit considerations of surfaces and interfaces, and easy determination of energy and angular distributions.

In the binary collision approximation the collision is treated as a classical two-body

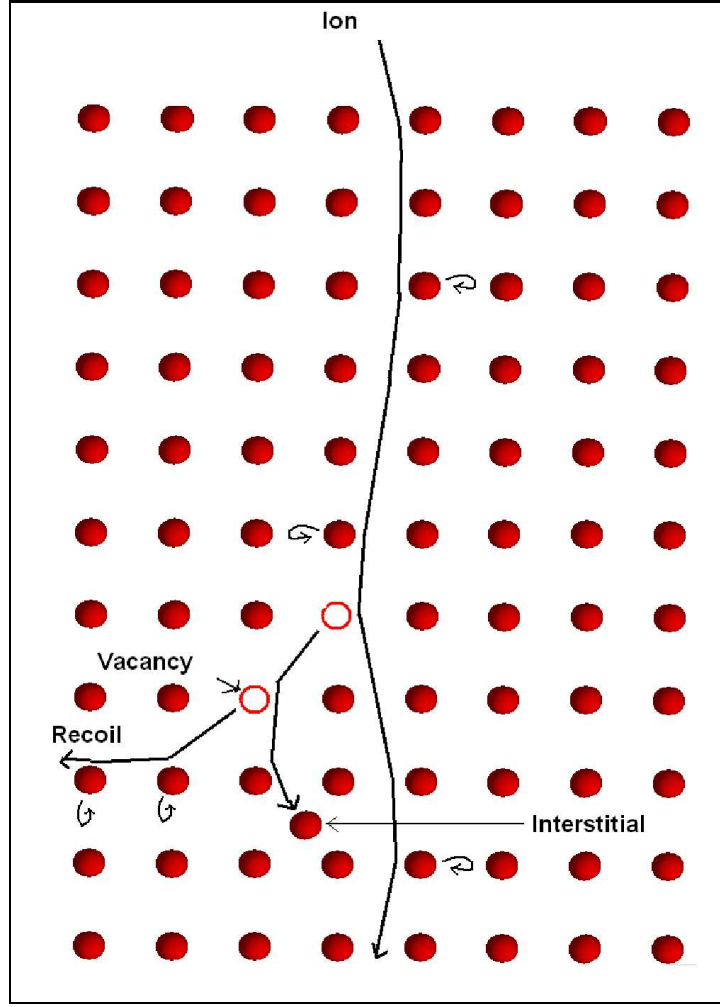


Figure 2.2: *Schematic view of an ion trajectory in the binary collision approach.*

problem with an interatomic potential which includes classical and quantum mechanical terms. The basic assumption of the BCA is that the ion interacts with only one target atom at a time what allows the use of the scattering theory from classical mechanics. Fig. 2.2 shows the ion trajectory and possible interaction of the ion with the crystal atoms. Ions scatter from the target atoms (nuclear energy loss) and are further slowed down by the interactions with the target electrons (electronic energy loss). A target atom is displaced from its lattice position through a ballistic process if the energy transferred to it exceeds the displacement energy (15 eV for silicon), starting a new recoil and leaving behind a vacancy. If the energy transfer is less than the threshold value

the atom remains at its lattice site. The trajectory of ion or recoiled atom is terminated when either the energy drops below a pre-specified value or when the particle leaves the target. The BC method provides the atomic coordinates of the implanted ion and the generated Si interstitials and vacancies during the collision cascade. Thousands of cascades can be simulated to provide satisfactory statistical resolution and to generate reliable dopant and damage profiles. This method has been successful in predicting ion and damage profiles, and has been used much since the 1960's. [8, 81–84]. Owing to the basic approximation that collisions are binary, problems arise when the collision cannot be fully described as two-body collision and multiple interactions between the ion and the target atoms have to be taken into account [84–86]. Furthermore, more complex defect types cannot be obtained by BC simulations.

For the purpose of this thesis we use the IMSIL (IMplant SIMuLator) program, which is a Monte Carlo code based on the binary collision approximation (MC-BCA). Details about the physical model implemented in IMSIL can be found in [8]. For the purpose of this thesis IMSIL-BC has been recently extended by a RBS/C module which allows the calculation of Rutherford backscattering/channeling spectra [77].

2.4 Molecular Dynamics

Molecular dynamics (MD) methods describe the interactions involved in ion implantation more realistically than BC methods, but require much larger amounts of computer capacity than BC methods [84, 87]. In principle they can use interatomic potentials derived from ab-initio or tight binding MD codes, but simulation of large simulation cells with energies commonly used in ion implantation is presently only possible with semi-empirical interatomic potentials [36]. In classical molecular dynamics models the time evolution of a system is determined by the semi-empirical potential and the classical Newton's mechanics. In the Newtonian approach the force \vec{F}_i acting on an atom i is calculated as [87]

$$\vec{F}_i(\vec{r}_i) = \sum_{j \neq i} \vec{F}_{ij}(\vec{r}_{ij}) = - \sum_{j \neq i} \nabla V_{ij}(r_{ij}) \quad (2.1)$$

where \vec{F}_{ij} is the force acting between atoms i and j and V_{ij} is the interatomic potential chosen by fitting experimental data or ab-initio calculations. In order to save calculation time and to reduce the complexity of the algorithm the sum in Eq. 2.1 is usually not calculated over all atoms in the cell but taken over the atoms within the cut-off radius which is determined by the cut-off value of the chosen potential. Since MD simulations solve equation 2.1 for all atoms in the simulation cell they are limited to the cell sizes of the order of ten million of atoms. Due to the requirement to resolve lattice vibrations (≈ 0.1 ps) their maximum feasible simulation times are up to the nanosecond range. Therefore, they are not suited for thermally activated processes at time scales that occur in industrial processing steps. Despite these limitations they can be used to extract a variety of information about formation mechanisms of different defect types and also for the description of amorphous pocket formation [2, 36, 88], although at lower implant energies due to high computational cost.

On the other hand, the accuracy of MD calculations strongly depends on the used interatomic potentials. Simulations have shown that the same system studied with different interatomic potential leads to significantly different results [36, 52, 89]. Another problem of the semi-empirical MD calculations is the transferability. Since the parameters are usually fitted to experimental data, they are excellent at predicting quantities they were parameterized to calculate, but their predictive power in other situations is not guaranteed.

We performed our MD simulations with a code that was written by Gärtner [84]. It uses either the Stillinger-Weber interatomic potential [90] splined with a more accurate interatomic potential for small separations [91] or the Tersoff potential [92]. The time integration is performed with the Verlet algorithm [93] with an adaptive time step. The detailed description of the used MD scheme can be found in [84, 89].

2.5 Kinetic Monte Carlo

The Monte Carlo methods are numerical techniques capable to handle complex mathematical problems through random sampling. In the last decades fast evolution of the computer industry has allowed fast development of Monte Carlo methods as universal numerical simulation technique [94]. In the kMC method reactions are described

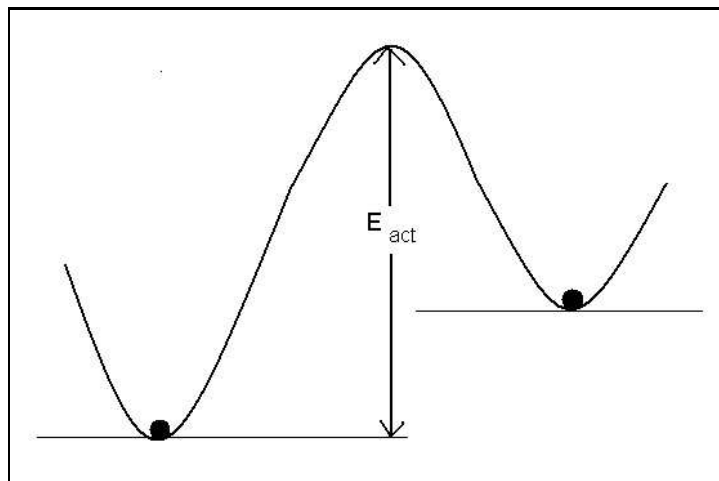


Figure 2.3: *Schematic representation of the energy barrier in kinetic Monte Carlo.*

through their reaction probability instead of rates in complex set of partial differential equations, as it is done in continuum simulators. The kMC method is an event driven technique, i.e. simulates events at random with probabilities according to the corresponding event rates. Fig. 2.3 illustrates the concept behind the kMC approach. A jump between the two states occurs when the internal energy exceeds the activation barrier, which is usually overcome by thermal activation. The probability of exceeding the energy barrier is given by Boltzmann's distribution, leading to an average event rate P_i [12]:

$$P_i = D \times \exp(-E_{i,act}/kT) \quad (2.2)$$

D is the prefactor, $E_{i,act}$ is the activation energy, k is the Boltzmann's constant, and T temperature. The times of the events are selected according to the calculated event rates using generated random numbers. For each event the corresponding event time is calculated according to:

$$t_i = -1/P_i \times \ln R_n \quad (2.3)$$

where R_n is random number between 0 and 1. The event with minimal event time is executed. If the system consists of a set of very high rate events, which after some time have reacted and disappeared from the system leaving behind the slow-rate

ones, the time step will automatically rise. Therefore the kMC method can simulate the timescales involved in typical technological processing steps, including thermally activated processes. kMC simulations have been extensively used in silicon damage studies since 1996 [40, 42, 43, 45, 58, 95–97]. In order to get accurate results kMC models require correct list of defect types and possible events together with their activation energies. These informations are usually obtained from external sources, experiments or *ab initio* calculations. The complexity of the problem increases with the number of different interacting defects and with the size of defect clusters. Unfortunately, the transition energies are often unknown for defect clusters and approximations have to be made. Furthermore, kMC cannot simulate ballistic processes because they cannot be classified into a finite number of events.

In lattice kMC codes all defects and their corresponding lattice sites [12] are considered in the simulation cell. While in non lattice kMC code only the intrinsic (interstitials and vacancies) and extrinsic (dopant) defects are included in the simulation cell [41].

2.6 Continuum models

In continuum simulation the system is formulated as a set of partial differential equations for each particle type considered in the process [98, 99]. The particle gain or loss is formulated in terms of its generation and recombination rates and the diffusion flux. The numerical solution of the set of equations requires spatial and temporal discretization to reduce the derivatives into algebraic differences. The discretization converts the problem to a large set of linear equations which are solved using standard numerical methods. Since continuum models can more easily include other standard wafer processing steps like oxidation, metal deposition etc, they are still widely used in industrial applications. Because their space discretization is not limited by the atoms, the continuum models are capable to simulate large sizes what is their main advantage over the atomistic models.

However, this advantage is reduced as the device size shrinks. Reducing the sizes the complexity of physical reactions on atomistic level shows up, what cannot be taken into account by simple refining the grid used in the numerical solution. Also, the inclusion

of new interactions imply the adding of new coupled differential equations which leads to the growing of the complexity of the system. In addition, the standard continuum approach does not take into account the spatial correlation between defects produced in the same collision cascade [100], in contrast to Monte Carlo simulations [12].

2.7 Multi-scale approach

From the discussion in the previous sections we can conclude that no single simulation technique can simulate the whole process of damage creation and subsequent annealing including all physically relevant phenomena. Either the simulation methods are limited by computer capacity or they are not capable to give satisfying insight into all physical processes. Therefore it is necessary to develop a hierarchical modeling scheme which goes from quantum mechanical ab-initio calculations up to continuum methods in order to create simulators capable to describe the whole ion implantation process. In this thesis we combine the existing and develop new models to achieve the better understanding of the damage physics.

Fig. 2.4 summarizes the models proposed in this thesis. The figure shows the relation between the standard simulation methods (BC, MD, ab-initio) and newly developed simulators (heat flow, RBS/C and atomistic damage model) in this thesis. It emphasizes the importance of the multiscale approach where the calculation on the different time and size scales are used to extract the parameters and initial conditions for the higher level simulators.

An amorphous pocket model based on a single simulation method does not seem to be realistic. BC methods cannot simulate either the heat quenching process or more complex damage types generated during the amorphous pocket creation. kMC methods are not able to simulate the quenching of the cascade since it cannot be classified into the finite number of events. MD and especially ab-initio methods are computationally too expensive for this purpose. In order to overcome these limitations in Chapter 3 we propose an amorphous pocket model that combines the binary collision approach with continuum modeling. Using the existing BC code “IMSIL” we obtain the geometrical distribution and remaining energies of the recoils and use it as input to a heat diffusion simulator which is based on the numerical solution of the heat transport equation. Af-

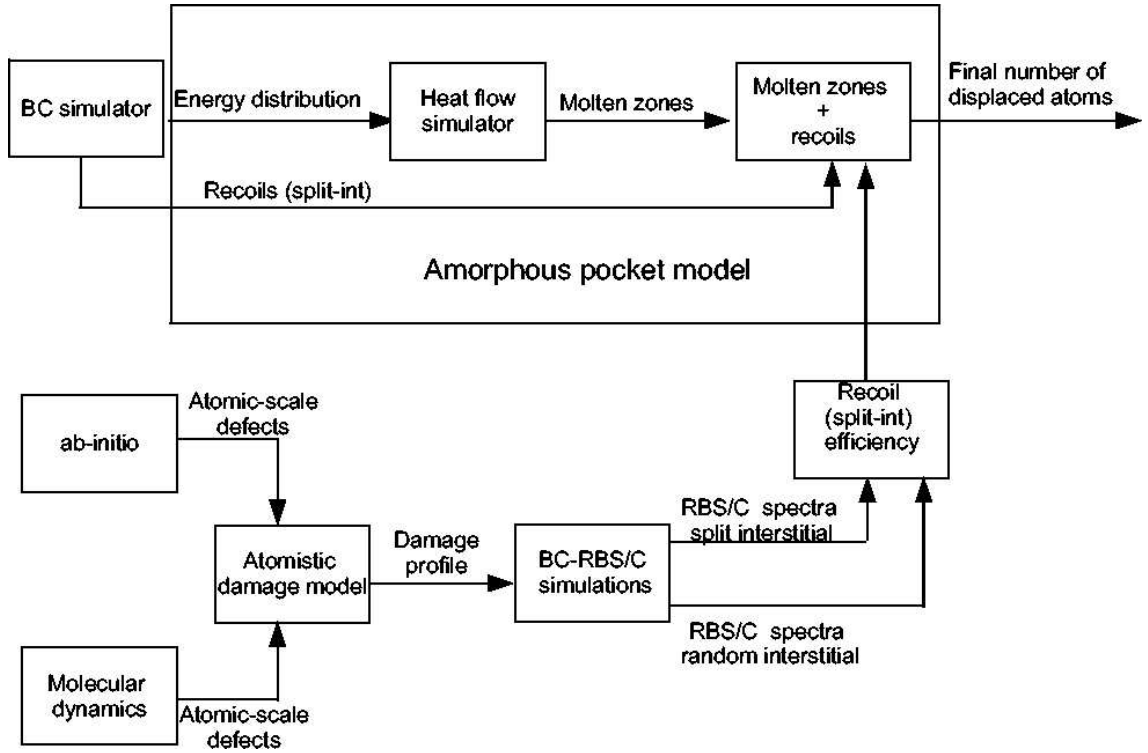


Figure 2.4: Summary of the two multiscale models proposed in this thesis and its interconnection.

ter a critical density of molten atoms is reached the lattice collapse occurs. In addition to molten atoms we consider the recoils which are also obtained by BC simulations. Taking advantage of both approaches, atomistic and continuum, we extend the understanding of the amorphous pockets creation process.

In other approach, explained in Chapter 4, a new atomistic model of damage is introduced (see Fig. 2.4). The model uses ab-initio calculations and molecular dynamics simulations to obtain the structure and defect coordinates of the small interstitial clusters. This atomic-scale modeling of defect structures was used to propose an atomistic model of damage for the purpose of BC-RBS/C simulations. The full quantum-mechanical treatment of the system cannot be achieved due to the limited computational resources. Nevertheless, the quantum-mechanical description of the atomic-scale defects can, in a large amount, be preserved and incorporated into a hierarchical scheme proposed in Chapter 4. Although limited on the analysis of Si containing low levels of

disorder, this model uses the advantages of the small scale modeling of defect structures to extend the damage models in RBS/C simulations. Furthermore, we emphasize the role of the interconnection of the two proposed models where the quantities extracted from RBS/C simulations are used to define parameters (recoil efficiency) for the proposed amorphization model.

2.8 Conclusion

We can conclude that there is no single simulation technique which can take into account the whole ion implantation damage process. The decision for appropriate simulation tool is always the compromise between the desired accuracy and the available computing resources. Since each technique usually gives informations at different size and time scale, they can be combined in a multiscale scheme to achieve better modeling of the desired process. Hierarchical modeling from ab-initio calculations to continuum models needs still to be developed and incorporated into mainstream simulators [4]. Within this thesis we propose two multiscale methods to improve the state of the art of damage modeling.

Chapter 3

Amorphous Pockets

3.1 Introduction

Amorphous pockets are generated by high-density energy deposition, which leads to local melting of the target. They have been observed in silicon by transmission electron microscopy after low-dose heavy [18] and medium-mass [101] ion implantation at cryogenic temperatures. RBS/C measurements [6, 13–15] and molecular dynamics simulations [2, 36, 102] have confirmed the existence of amorphous pockets, especially upon heavy ion implantation.

The process of amorphous pockets creation has been interpreted by the energy spike model [15] which says that a sufficiently high density of energy deposition leads to local melting of the target and thus to more efficient damage production. It is also discovered that the amorphous pockets can be formed through melting and quenching[46, 103, 104]. If the energy transferred to a single atom is lower than the displacement energy for the particular material (15 eV for Si) it is not extracted from its lattice position, but when many neighboring atoms simultaneously receive a small amount of energy the region may melt.

The process of creation and subsequent recrystallization of amorphous pockets are interesting, not only fundamentally, but also because of their influence on the wafer fabrication process. Preamorphization of a wafer prior to dopant implantation can be useful for creation of ultra-shallow junctions, suppressing channeling and leading to a high activation of the dopants at much lower temperature than that required for

annealing of damaged crystalline regions [105]. The disadvantage of this technique is that, after regrowth, end of range defects may remain beyond the initial amorphous to crystalline (a/c) interface. During subsequent annealing these defects contribute to dopant clustering, cause transient enhanced diffusion, and may increase the junction leakage if they are not completely removed [43]. Since a controversy about the mechanisms of amorphization is still present [41, 43, 46, 106], a need for good understanding of amorphization mechanisms and for the development of predictive models exists.

Despite many published amorphization models [41, 46, 58, 106, 107], several effects, i.e. the ion mass and polyatomic effect have not been quantitatively modeled up to date. Within this thesis we suggest an amorphization model which will be able to quantitatively explain the experimental findings on the ion mass and polyatomic effect. Using standard binary collision simulation the spatial distribution of energy deposition is obtained. It is assumed that all deposited energy is instantaneously converted to heat, and the subsequent heat quenching process is modeled with the heat transport equation. The heat transport equation is modified to consider the heat of melting, when the melting temperature is crossed at any point in space, and the energy is stored into the crystal after an ion melts. It is discretized with the finite volume method on grid points that coincide with the crystallographic lattice sites, which allows easy determination of the initial conditions and molten atoms. In order to avoid the unphysical concept of a single molten atom we require that before an atom is considered as molten that its neighbors also meet the melting criterion. After the heat flow simulation and detection of molten atoms the following procedure is applied: For each atom in the cell the local concentration of the molten atoms contained in the sphere defined within the radius, with center in the investigated atom, is examined. If the concentration of molten atoms exceeds the critical defect density the atom is labeled as amorphous, if not it is crystalline. The loop is done over all atoms in the cell, and the new configuration of amorphous atoms is obtained. We find that using a melting radius of 8Å and the critical defect density of 10% we obtain very good agreement with the experimental results. We will show that the simulations without taking into account the local lattice collapse are not able to qualitatively and quantitatively explain the experimental data. Therefore we can conclude that the local collapse of the crystal lattice once the damage exceeds a threshold is an important mechanism for amorphous pocket creation.

In the Section 3.2 we explain in detail the ion mass and polyatomic effect which particularly will be treated with our model. In the next Section 3.3 we discuss the

state of the art of the published amorphization models. In Section 3.4 we present the numerical and computational details of our model, followed with the results and discussion in Section 3.5. Final conclusion is given in Section 3.6.

3.2 Energy spikes in Si due to heavy ion bombardment

In this section we introduce the experimental data on the ion mass and polyatomic effect and their physical interpretation. These two effects are clear evidence of the amorphous pockets existence. The experimental data presented here have been obtained by in-situ RBS/C measurements at cryogenic temperatures where annealing effects are absent, what is important since our model accounts only for the amorphization and not the recrystallization process at the same time.

3.2.1 Ion mass effect

Figure 3.1 shows the number of displaced atoms per incident ion versus energy deposited in nuclear collisions for different ion species, obtained at cryogenic temperatures [6]. The energy deposited in nuclear collisions is a monotonic function of the implant energy. The dotted line represents the prediction of the classical displacement energy criterion calculated according to the modified Kinchin-Pease formula [5] and is presented for comparison purposes.

From Fig. 3.1 the deviations of the measured numbers and those predicted by the classical displacement theory can clearly be seen. The discrepancies are greater by up to a factor of ≈ 8 for the heavier elements. Furthermore, a systematic dependence of the number of displaced atoms on both ion mass and energy is evident in Fig. 3.1 for the experimentally obtained values. For constant nuclear deposited energy the number of displaced atoms consistently increases as the mass of the implanted ions increases. The other systematic dependence is that for constant ion mass, the gradient of the number of displaced atoms decreases with energy finally approaching the value predicted by

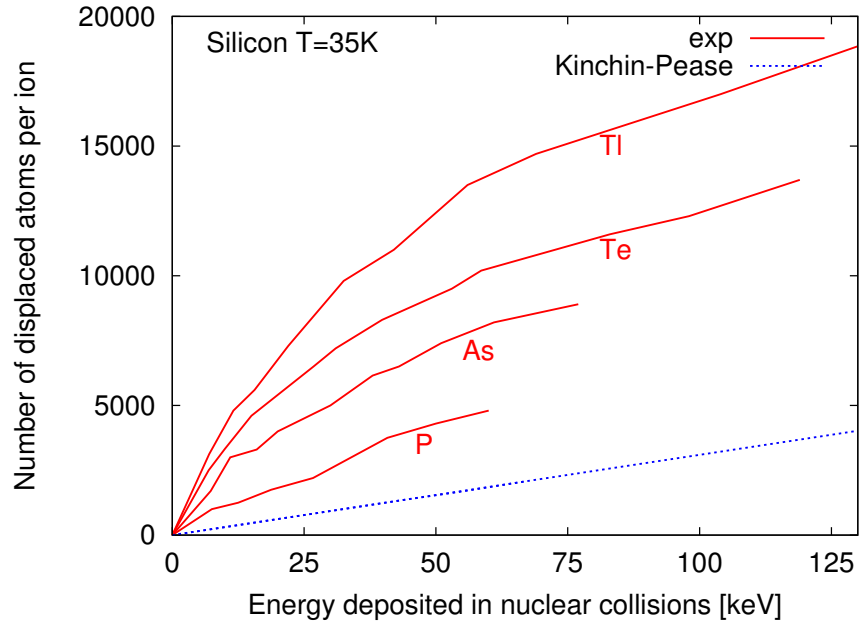


Figure 3.1: Number of displaced atoms per incident ion as a function of energy deposited in nuclear collisions for various implant species (at 35 K). Experimental results - solid lines [6]. The dashed line denotes the prediction of the modified Kinchin-Pease model [5].

the modified Kinchin Pease formula. Both of these dependences can be explained by the energy spike model [6, 13, 15].

As the incident ion mass increases, the cross section for the nuclear (elastic) collision increases what results in a higher density of recoil atom being produced and subsequently higher density of energy deposition. The heavier the ion is the larger the nuclear losses are and the smaller the range of the ions is. Due to the smaller range heavier ions deposit their energy in a smaller volume, what increases the probability of energy overlapping leading to a more efficient damage production. Therefore the damage production increases with ion mass. Reducing the ion mass leads to the development of more discrete and isolated structures within the cascade. This reduces the probability of overlap of the heat zones and leads to a less efficient damage production.

Fig. 3.2 illustrates the distribution of the energetic atoms, obtained by binary collision simulation, for a light (B) and a heavy ion (Tl) implant for the same ion implant

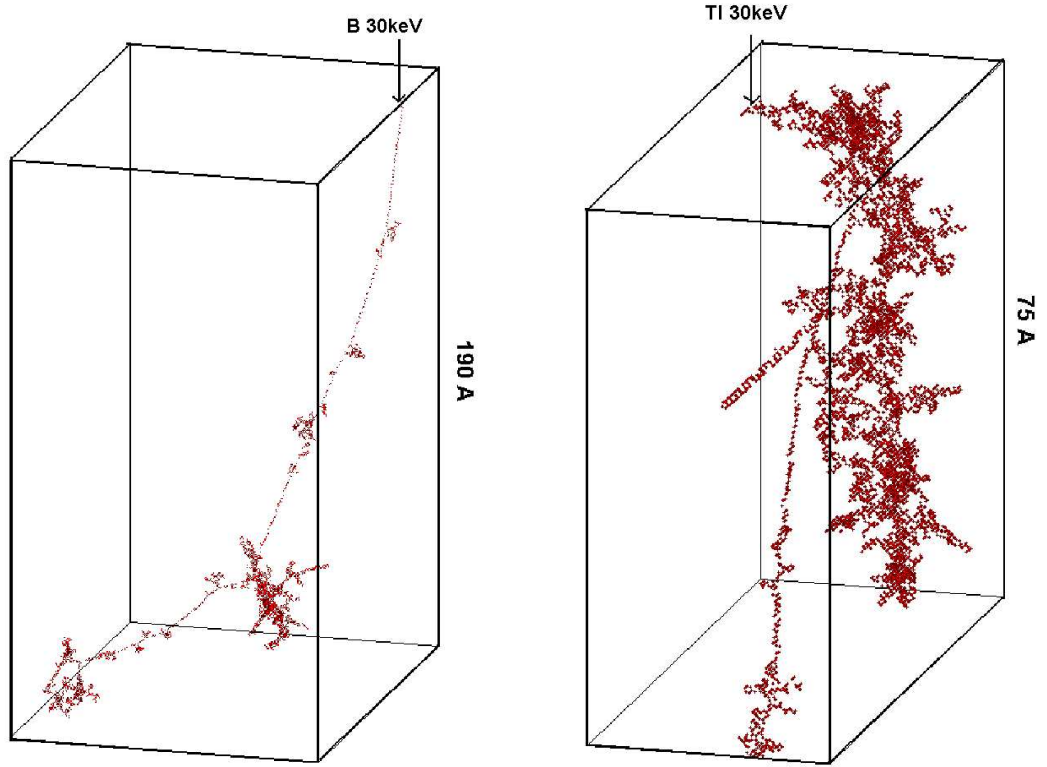


Figure 3.2: *B30 keV implantation cascade (left) and Tl30keV implantation cascade (right) obtained with BC simulations, showing the differences in created damage density upon light ion (B) and heavy ion (Tl) implantation for the same ion implant energy. The arrows indicates the ion's entrance point, while the maximum range of obtained energetic atoms (or the size of simulation cell) is 190 Å and 75 Å, respectively. As it can be seen the density of recoils of Tl cascade is large, which in turns lead to amorphization of local regions, what is not the case for B implants.*

energy (30 keV). The term “energetic atoms” refers to the atoms that have received a minimum energy in the collision event, but not enough to leave their lattice sites, as well as to the slowed-down recoiled atoms which were originally displaced from their lattice sites and finally settle in the crystal lattice. The presented distributions confirm that heavy ions (Tl) have smaller range (75 Å) compared to light (B) ions (190 Å), and thus deposit their energy in a smaller volume. Heavy ion creates large clusters of disordered atoms, while the size and the number of disordered atoms in clusters pro-

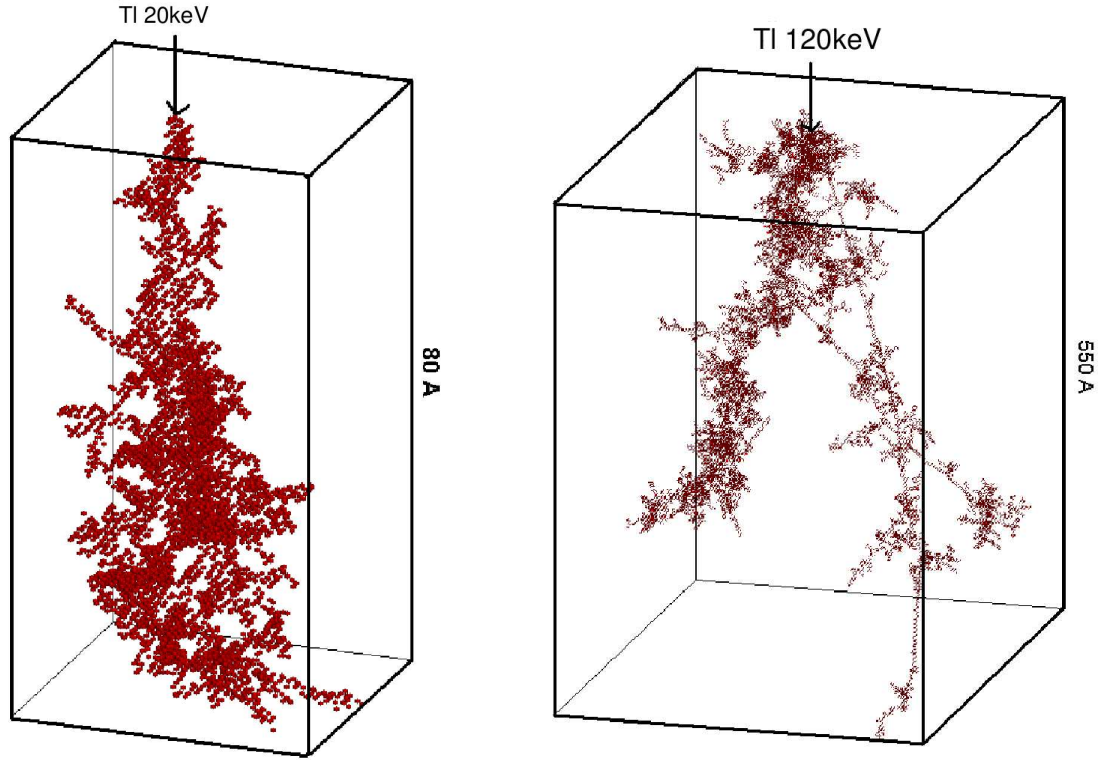


Figure 3.3: *TI 20 keV (left) and TI 120 keV (right) implantation cascade obtained with BC simulations. Low energy range ions (TI 20 keV) create very dense cascade through all part of its trajectory, while the high energy implant (TI 120 keV) creates the subcascades (Si recoils) which carry the energy out of the high energy deposition region thus decreasing the probability of energy overlapping. The arrows indicates the ion's entrance point, while the maximum range of obtained energetic atoms is 80 Å and 550 Å, respectively .*

duced by light ions (B) are much smaller. In addition a more isolated cascade structure is observed upon light (B) than heavy ion (TI) implant, what is consistent with the discussion given in the energy spike model.

The systematic energy dependence of damage for constant ion mass is explained as follows [6]: Also in Fig. 3.1 two energy ranges with different slopes for constant ion mass can be distinguished. This difference in the slope has been taken as evidence

that the damage created through heavy ion impact can be assigned to at least two different types as a function of energy. The relative contribution of each component is determined by the incident ion energy and can be divided in two ranges. For low and medium energies ($E_{nuc} < 60 \text{ keV}$) ions create an amorphous zone over a major part of their trajectory leading to the superlinear damage enhancement. At higher energies ($E_{nuc} > 60 \text{ keV}$) the asymptotic approach of the measured energy dependence to those predicted with the classical displacement model indicate that during the initial part of the ion trajectory, the displacement collisions were enough spatially separated so that the energy deposition is dilute enough, what reduces the influence of energy spike in this energy range. Due to enough separated energy deposition during the initial part of the ion trajectory, high energy ions create mainly isolated defects. Therefore, the conclusion is that in this regime the linear cascade model plays a more important role. In the high energy range the gradient of the number of displaced atoms versus energy approaches, but does not reach, the value calculated according to the modified Kinchin-Pease model. The actual value of the slope extracted from the experimental data presented in Fig. 3.1 for Tl implant in the $E_{nuc} > 60 \text{ keV}$ regime is ≈ 2 times the Kinchin-Pease slope.

In Fig. 3.3 we illustrate the results of the BC simulation for 20 keV and 120 keV Tl implants. Presented distributions of the energetic atoms confirms the qualitative difference in the cascade topology for two different energy regimes. Tl 120keV ions create spatially separated subcascades because high energy Si recoils carry energy out of the high energy deposition region. This in turn dilutes the energy distribution, reducing the probability of energy overlapping. For low energy implant (Tl 20 keV) the density of displaced atoms is high throughout the whole part of the ion trajectory, what increase the probability of energy overlapping and thus the efficiency of damage generation.

3.2.2 Polyatomic effect

According to the standard displacement model the number of displaced atoms per incident ion as a function of energy per atom, for the molecular implantations should be the same as when the atomic ions are implanted separately. But it is discovered that each molecular ion produces more damage per implanted ion than the corresponding

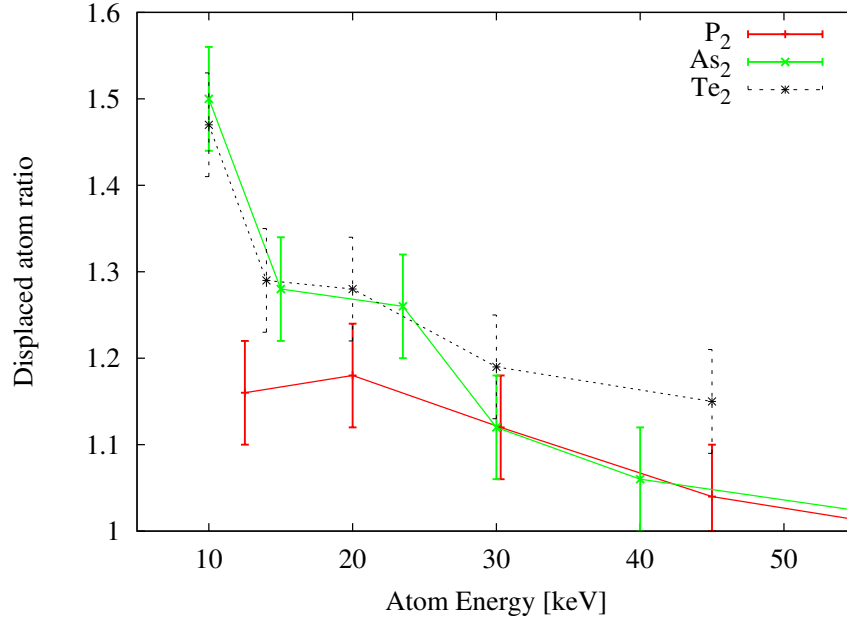


Figure 3.4: Ratio of the number of displaced atoms after P_2 , As_2 and Te_2 molecular implantation and the corresponding number after atomic ion implantations with the same atom dose and atom energy, as a function of atom energy. Lines: Proposed amorphous pocket model. Symbols: in-situ RBS data obtained at cryogenic temperature [6].

monoatomic bombardment [6, 15] for the same values of energy per atom and for the same atomic dose. Fig. 3.4 shows the ratio of the number of displaced atoms after P_2 , As_2 and Te_2 molecular implantations and the corresponding number after atomic ion implantations with the same atom dose and atom energy [6]. From Fig. 3.4 a systematic variation of the ratio of the number of displaced atoms with both ion mass and energy can clearly be seen. As the ion energy increases the energy spike becomes of less importance, since it occurs at the end of the ion trajectory. Therefore less overlap of the spikes created by the individual atoms of the molecule occurs leading to less increase in the local energy density. This in turn decreases the gradient of the displaced atom ratio as the energy increases. The decreasing magnitude of the displaced ratio with ion mass is explained by the expected differences in the cascade structures. The heavy ion cascade would directly form an amorphous zone over a major part of its trajectory as discussed in the previous section. As the ion mass is reduced, a discrete and isolated structure develops within the collision cascade. This reduces the probability of overlap

of the branches of the cascades of the individual atoms of the molecular ion. Therefore, the local energy density is smaller and less damage is produced for lighter ions. We can conclude that the polyatomic effect is less pronounced for light than for the heavy ions.

3.3 Existing amorphization models

In this section we give an overview of some of the existing amorphization models summarizing their field of application and pointing out at their limitations.

The number of displaced atoms predicted by the modified Kinchin-Pease model is given by: $N_D = 0.42E_{nuc}/E_d$, where E_{nuc} is the energy deposited in nuclear collisions and E_d is the threshold displacement energy, i.e. the energy necessary to produce a displaced atom in the target [5]. For silicon, the displacement energy is conventionally taken as 15 eV. In Fig. 3.1 the experimental results [6] and the predictions of the modified Kinchin-Pease model are compared. From the figure we can see that the damage induced by heavy ion mass bombardment far overwhelms the damage predicted by the modified Kinchin-Pease model. In addition since the number of displaced atoms in the modified Kinchin-Pease model depends only on the energy deposited in nuclear collisions and not on the ion mass, this model is able to qualitatively describe neither the ion mass effect nor the polyatomic effect.

One of the often used amorphization models is based on a critical point defect concentration, i.e. a region becomes amorphous if a critical defect density is exceeded [7,107] (see Fig. 1.1). A variation in the critical defect density leads to a different depths of the a/c interface, which strongly affects the amount of damage after recrystallization. The range of the reported critical point defect density is presented in Fig. 3.5 [7]. It can be seen that the CPDD is uncertain within a factor of 10.

Vineyard has proposed a simple heat flow model to estimate the size of amorphous pockets [108]. After the recoils have slowed down below the cutoff energy he has assumed that their remaining energy can be converted to temperature and the subsequent evolution of heat can be treated with Fourier law. In Fig. 3.6 we have compared the

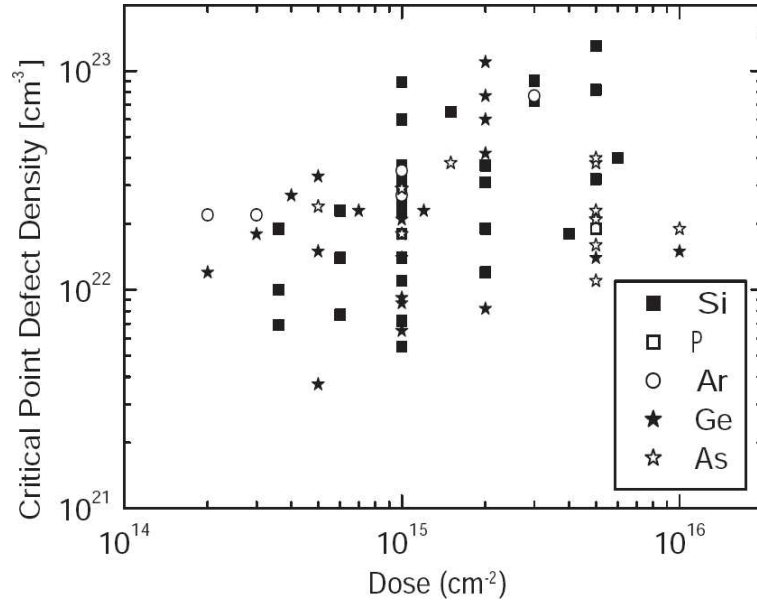


Figure 3.5: Critical point defect density extracted from measured depths of amorphous layers and BC simulations [7].

results of Vineyard's model with the published experimental results. The results of Vineyard's model are obtained using coupled BC/pure heat transport model. The remaining energy of the energetic ions, calculated by BC, is converted to temperature and the quenching is simulated by the Fourier law. An atom is considered as molten when its temperature crosses the melting temperature. We can conclude that using the simple heat equation based on Fourier law with the criterion that the target melts wherever the melting temperature is exceeded, highly overestimates the number of displaced atoms per incident ion. It also does not give any ion mass effect. One of the reasons could be that this model does not take into account the heat of melting.

L. Pelaz et al. have proposed kMC treatment of amorphization and recrystallization based on interstitial-vacancy (I-V) pairs (bond defects) as elementary units [41–44]. The BCA simulations are used to generate the distribution of the interstitials and vacancies. As the vacancy approaches an interstitial they do not recombine immediately but form a metastable defect, known as bond defect. The bond defect, presented in Fig. 3.7, consists of a local rearrangement of bonds in the crystal with no excess or deficit of atoms. The amorphization of material is supposed to occur when the local

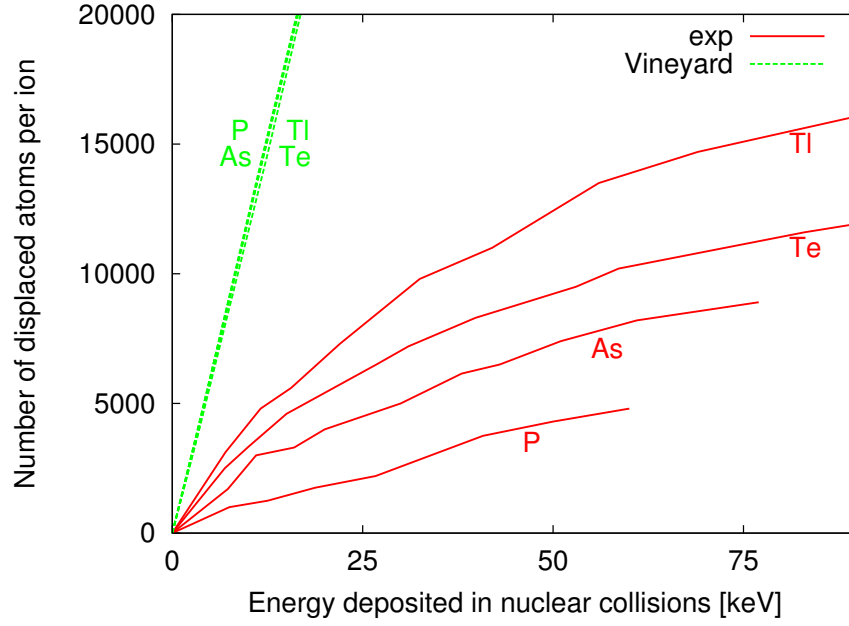


Figure 3.6: Number of displaced atoms per incident ion as a function of energy deposited in nuclear collisions for various implant species P, As, Te, Tl. Experimental results: solid lines [6]. Dashed lines represents Vineyard's model simulations obtained with our simulator.

concentration of bond defects exceeds 25%. Amorphous pockets are treated as conglomerates of bond defects, using Monte Carlo methods and assigning activation energy to each bond defect. The activation energy of the particular I-V pair increases with the number of surrounding I-V pairs, going from 0.43 eV for isolated I-V pair up to 5 eV for I-V pair embedded into an amorphous matrix. This model was able to explain the following experimental observations: the superlinear dependence of damage accumulation with dose (see Fig. 3.9), the critical regime for the crystal-amorphous transition determined by the dose-rate and implantation temperature (see Fig. 3.8), and the recrystallization dependence on amorphous-crystal interface morphology. On the other side, since defect annealing is absent at cryogenic temperatures this model is not able to properly treat the ion mass and polyatomic effect described in Section 3.2. Therefore, a model based only on the kMC approach is not capable of explaining these two effects. In addition, it is questionable whether the whole amorphization and crystallization process can be based on a single defect type, namely bond defect, whose existence has not yet been confirmed experimentally but only by molecular dynamics

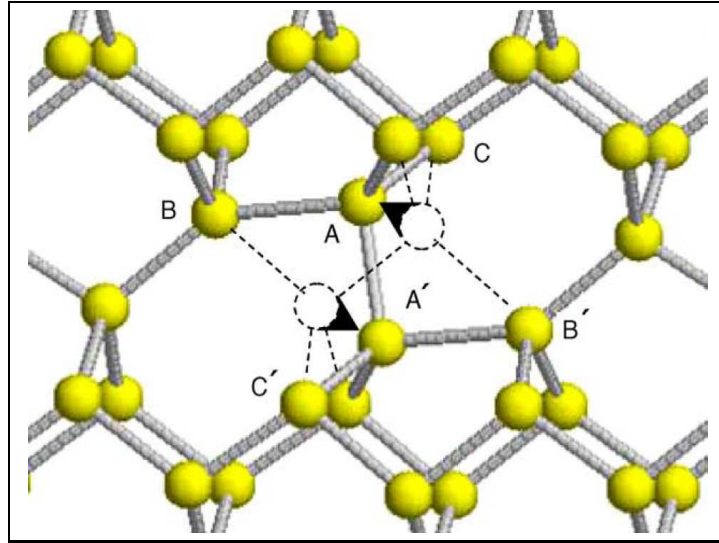


Figure 3.7: Atomic structure of the bond defect. Dashed lines represent atoms and bonds in the perfect lattice. Atoms A and A' move along the direction indicated by the arrows and switch their bonds with atoms B and B', giving rise to the bond defect [44].

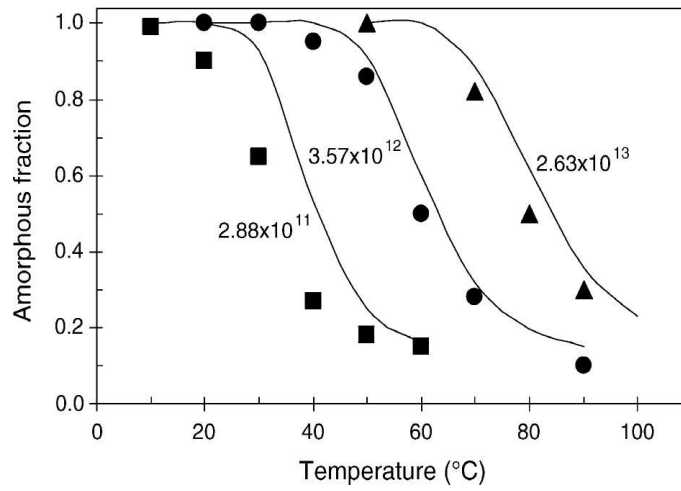


Figure 3.8: Amorphous fraction vs. substrate temperature for 1MeV Si implants to a dose of 10^{15} cm^{-2} with several dose rates in $\text{cm}^{-2} \text{ s}^{-1}$. Solid symbols correspond to the experimental data, obtained with RBS. Solid lines: simulation results with proposed model [41, 44].

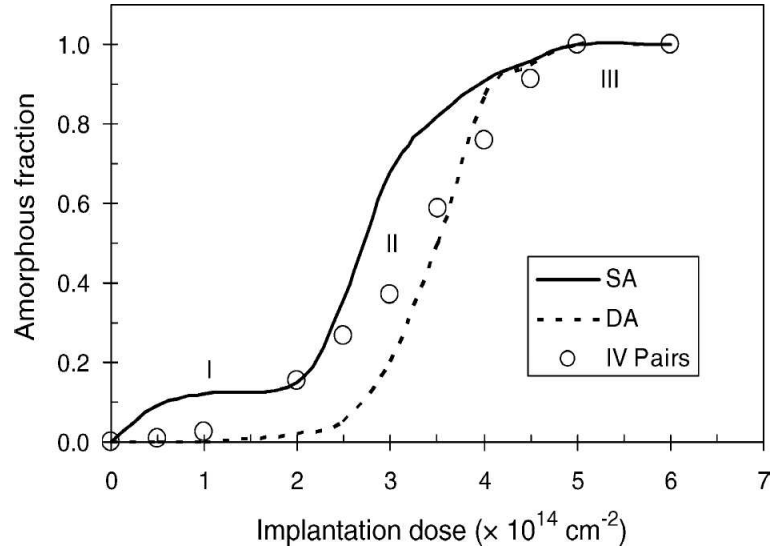


Figure 3.9: Dose dependence of the damage produced by 100 keV Si ions at room temperature. Solid and dashed lines correspond to the single (SA) and double alignment (DA) RBS experiments. Symbols represent I-V pair model [41].

simulations [44].

Another model, recently proposed by Hobler et al. [46], takes into account the heat of melting for each atom. The model is based on melting studies performed by MD simulations. All atoms within a small sphere in the center of the simulation cell are given the same energy and the evolution of the system has been observed. Displaced atoms have been identified with the Lindeman criterion [109]. It was found that a well defined minimum density of deposited nuclear energy must be exceeded in order that an amorphous pocket may be generated, which is shown in Fig. 3.10. Above this threshold the size of the amorphous pocket depends only on the total amount of deposited energy rather than the energy deposition density. For deposited energy densities higher than about 2.5 eV/atom the size of the amorphous pocket is larger than the size of the sphere of initially energetic atoms, which is consistent with the melting process predicted by the spike effect. Based on these MD results the authors have presented another amorphization model: Each energy deposition event calculated with BCA simulations is assigned a sphere the volume of which would be molten according to the heat of melting (0.52 eV/atom in Si). The connected volume of overlapping

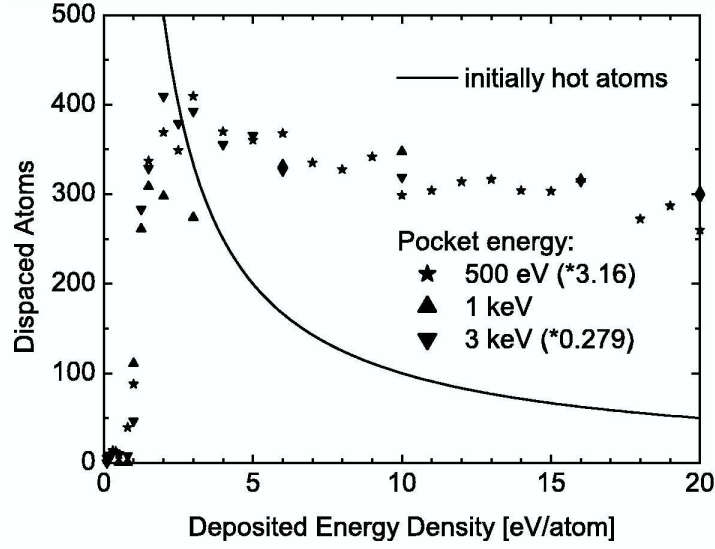


Figure 3.10: Number of displaced atoms 4.5 ps after giving atoms in the center of the simulations cell a total energy of 500 eV, 1 and 3 keV. The energy deposition density is varied. The number of displaced atoms for 500 eV and 3 keV are scaled by factors of 3.16 and 0.279, respectively [46].

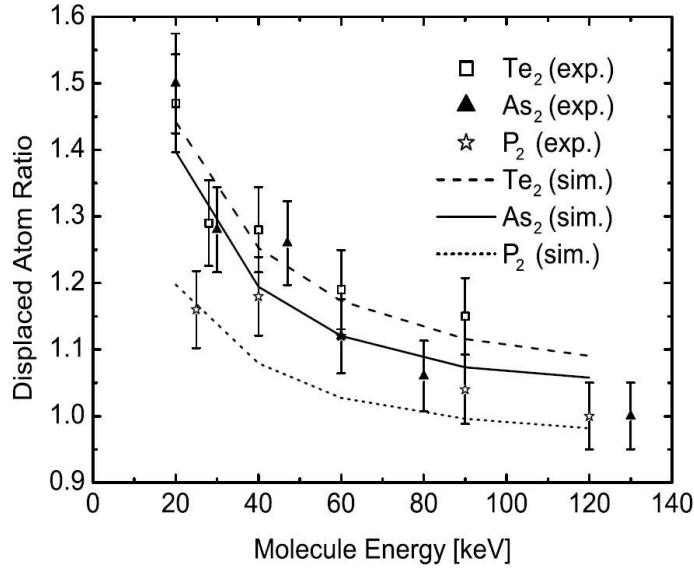


Figure 3.11: Ratio of the number of displaced atoms after P_2 , As_2 and Te_2 molecular implantation and the corresponding number after atomic ion implantations with the same atom dose and atom energy, as a function of atom energy. Lines: Proposed amorphous pocket model [46]. Symbols: in-situ RBS data obtained at cryogenic temperature[6].

spheres defines an amorphous pocket candidate. The number of displaced atoms contained in the volume is the ratio of the sum of energies deposited in it and the heat of melting. Surface effects are taken into account by shrinking the amorphous pocket with constant shrink radius and if the remaining pocket size meets the minimum 10 atoms, an amorphous pocket is generated, otherwise the interstitial is used to calculate the number of displaced atoms. The model yields the correct energy and the ion mass dependence of the poly-atomic effect at cryogenic temperatures as it is presented in Fig. 3.11. But on the other hand it has failed to explain the ion mass effect for mono-atomic implantations. In addition the model assumes spherical geometry of the pocket which, in general, is not the case in silicon.

The recently proposed amorphization model by I. Santos et al. [58, 104, 110] uses classical MD calculation to investigate the damage generation for energy transfers below the displacement energy threshold. Like in Hobler's model [46] atoms located in a sphere in the center of the simulation cell are given a certain energy with velocities in random direction, and the subsequent motion of atoms is simulated with the Tersoff III potential. The energy per atom is varied between 0 and 20 eV. Total deposited energies have been chosen between 50 and 500 eV. Displaced atoms have been extracted using a method based on the time average of atom coordinates. Considering the obtained MD results the authors have defined the efficiency of damage generation as the number of final displaced atoms per initial excited atom. Fig. 3.12 shows the efficiency of damage production as a function of the initial energy of excited atoms for different total deposited energies. From the figure we can see that, according to MD results, there is no stable damage production for initial energy densities below 1 eV/atom independent of the total energy deposited into the cell, while the standard BC approach requires minimum 15 eV/atom to generate a defect. These results are used to incorporate the effect of subthreshold energy interactions in BCA models. First, all energy transfers that take place during the BCA cascades are taken into account. Next, for every atom that receives more than 1 eV (MD threshold) in a collision a local environment is defined by considering all surrounding atoms within a second neighbor distance which also have energies above 1 eV. The atom and its local environment define a group whose efficiency can be extracted from Fig. 3.12. The atom is considered as molten, or displaced, only if the corresponding efficiency is equal or above one. Finally, the atom energy is shared with its neighbors. This procedure is repeated until all deposited energy is dissipated. The results presented in Fig. 3.13 compare the percentage of cascades generating a given number of the displaced atoms obtained by MD

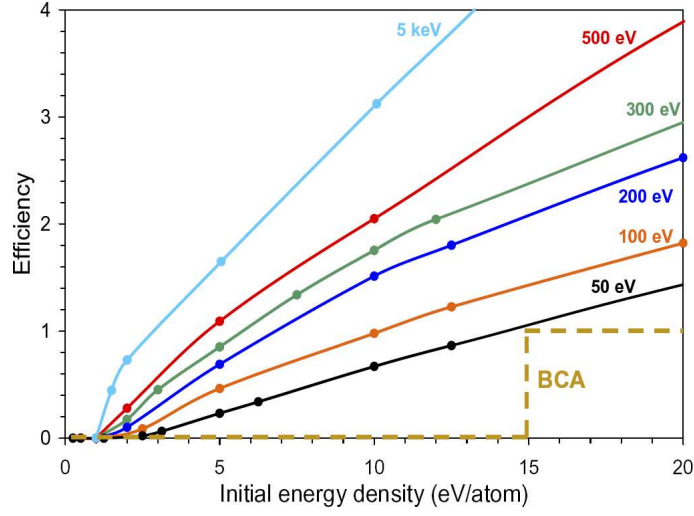


Figure 3.12: Efficiency of damage production as a function of the initial energy of moving atoms for different total deposited energies. Dashed lines represents the efficiency of BCA simulations [58].

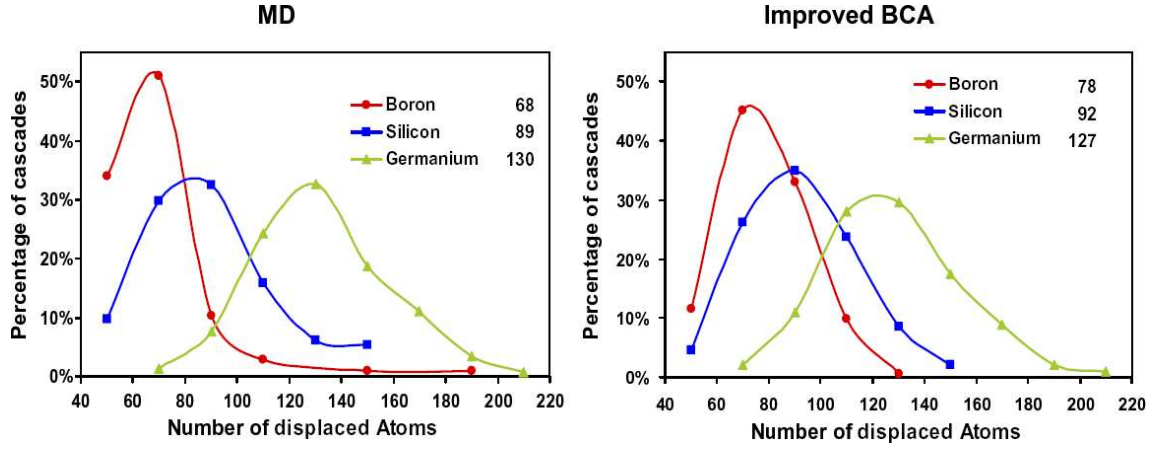


Figure 3.13: Percentage of cascades generating a given number of displaced atoms obtained from simulations of 1 keV implants of B, Si and Ge ions into Si using MD (left bottom) and improved BCA model (right bottom). Average numbers of displaced atoms are also shown [58, 104].

simulations and using the proposed BCA model. We see that the proposed modified BCA model obtains very similar results to those produced by MD simulations, but at a much lower computational cost. However, the comparison of experimental data within the results of this model is not attempted. On the other hand, the proposed model, like Hobler's model [46], assumes spherical melting geometry which is not always the case in silicon. In addition, the energy sharing between the neighboring atoms should be done correctly. Although the energy transfers below 1 eV cannot melt an atom, they can contribute to the overlapping of heat zones of neighboring hot atoms what can additionally increase the amount of damage.

We can conclude that no single up-to-date published model appears to be able to properly account for and predict all experimental observations related to amorphous pockets creation, but usually captures only certain part of the physics and therefore its application is rather limited.

3.4 Amorphous pocket model based on the numerical solution of the heat conduction equation and lattice collapse

Although MD simulations can simulate the damage accumulation upon heavy ion implantation and the amorphous pockets creation process, they are often not well suited for practical application due to their high computational cost. When designing a simulation concept for a heavy ion implantation one faces a much more complicated physics and variety of interactions and transition states between ion and material than for light ions, because heavy ions create amorphous pockets and not only point defects. This sets the requirement of making a compromise between the desired accuracy of the model, from one side, and the available computer resources from the other side. Trying to keep the physical background of the process and to avoid the computational limits imposed by MD simulations, we present a model of amorphous pocket creation based on binary collision simulations to generate the distribution of deposited energy, and on the numerical solution of the heat transport equation to describe the quenching process. The model uses Vineyard's assumption that the remaining recoil energy

can be converted into heat and subsequently treated with the simple heat diffusion equation [108]. Space is discretized with the finite volume method on grid points that correspond to the crystallographic lattice sites. The heat equation is modified to consider the heat of melting when the melting temperature is crossed at any point in space and to consider the energy stored into the crystal after an atom melts. Local collapse of the crystal lattice once the damage exceeds a threshold is also taken into account.

The results obtained with this model are in very good agreement with published experimental data on P, As, Te and Tl implantations in Si and with P, As, Te data on the polyatomic effect at cryogenic temperature.

Nevertheless, it should be pointed out that the heat conduction model is not strictly correct at such small space scales, but it is taken as a basis for practical modeling in many fields of science. Furthermore, the aim of our work is not to describe quantitatively every detail of the temperature evolution of the sample, but only to obtain the overall number of molten atoms upon heavy ion bombardement. Therefore, we assume that the heat conduction law gives a satisfying physical description of our problem.

3.4.1 Numerical model of the heat transport equation

Here we present the physical background of the heat transport equation and its numerical solution implemented in our simulations. Eventual limitations of the model are discussed.

When temperature is transferred through a system, the transport can be described, to a first order, by a phenomenological relation of the form [111–113]

$$\vec{q} = -\lambda(T)\nabla T(\vec{r}, t) \quad (3.1)$$

where T [K] denotes temperature, \vec{q} [W/m²] the heat flux and λ [$\frac{W}{m \cdot K}$] the thermal conductivity of material. Eq. 3.1 is known as Fourier's law, which reads: the heat flux is proportional to the negative of the local temperature gradient, heat flows from a hot reservoir to a cold reservoir. The heat flux measures the heat transfer per unit area in unit time, the temperature gradient provides the driving force for the flux and the

inverse of the thermal conductivity characterizes the resistance of the system to heat flow. Equation 3.1 is supplemented with the law of heat conservation [113–115]

$$\rho c_p(T) \frac{\partial T(\vec{r}, t)}{\partial t} = -\nabla \vec{q} \quad (3.2)$$

where ρ [$\frac{kg}{m^3}$] is the mass density and c_p [$\frac{J}{kg \cdot K}$] is the specific heat of the material, which is in general a function of temperature.

Since the initial conditions for the heat transport are obtained by BCA simulations which give the energy of recoils as output the left side of Equation 3.1 will be expressed as a function of energy. Using the energy equation applied to a solid undergoing conduction heat transfer we have [114]

$$E(\vec{r}, t) = \rho \cdot V \int_0^T c_p(\xi) d\xi \quad (3.3)$$

where V [m^3] denotes the volume of the system. Taking the derivative of Eq. 3.3 with respect to T we have

$$\frac{\partial E(\vec{r}, t)}{\partial T} = \rho \cdot V \cdot c_p(T) \quad (3.4)$$

Using the chain rule we can write

$$\left(\frac{\partial E(\vec{r}, t)}{\partial t} \right) / \left(\frac{\partial T(\vec{r}, t)}{\partial t} \right) = \rho \cdot V c_p(T) \quad (3.5)$$

combining Eq. 3.5 with Eq. 3.2 we obtain

$$\frac{\partial E(\vec{r}, t)}{\partial t} = -V \nabla \vec{q} \quad (3.6)$$

Introducing Eq. 3.1 in Eq. 3.6 we write the energy balance equation that describes conductive heat flow [116]

$$\frac{\partial E(\vec{r}, t)}{\partial t} = V \nabla(\lambda(T) \nabla T(\vec{r}, t)) \quad (3.7)$$

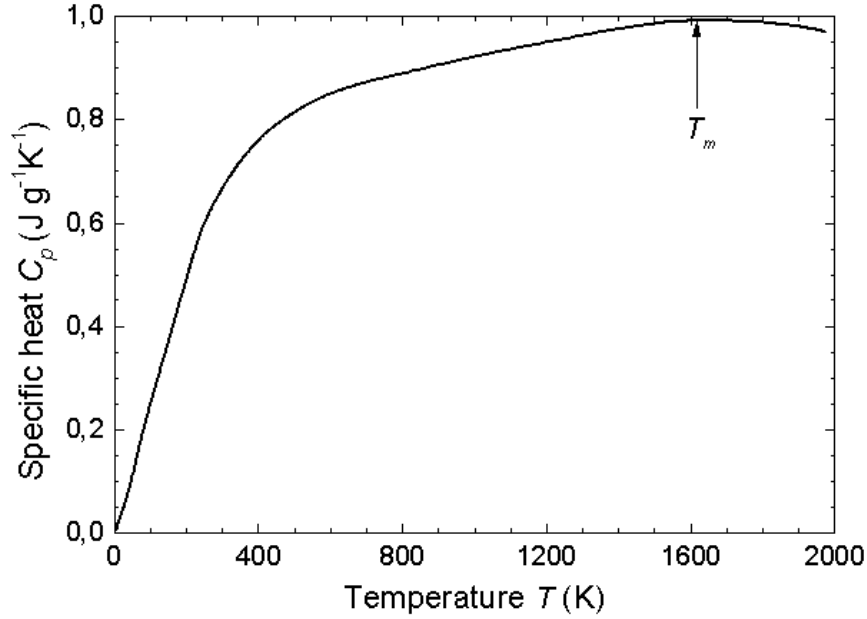


Figure 3.14: *Temperature dependence of specific heat for silicon [117].*

Due to the importance and wide range of potential applications, many analytical and numerical methods for the solution of the diffusion equation have been proposed [113, 115, 118–120]. But the analytical solutions are possible only for a few special cases of the initial and boundary conditions. In most cases Eq. 3.7 does not have an analytical solution, or the analytical solution is even more difficult to implement than a suitable numerical solution. Keeping in mind that one of the main ideas in the proposed amorphization model is the introduction of the heat of melting for each particular atom and atomistic resolution of the system for easy detection of molten zones, analytical solution would be rather time consuming and inappropriate to our problem. Therefore we solve Eq. 3.7 using numerical solution based on the finite volume method with atomistic space discretization.

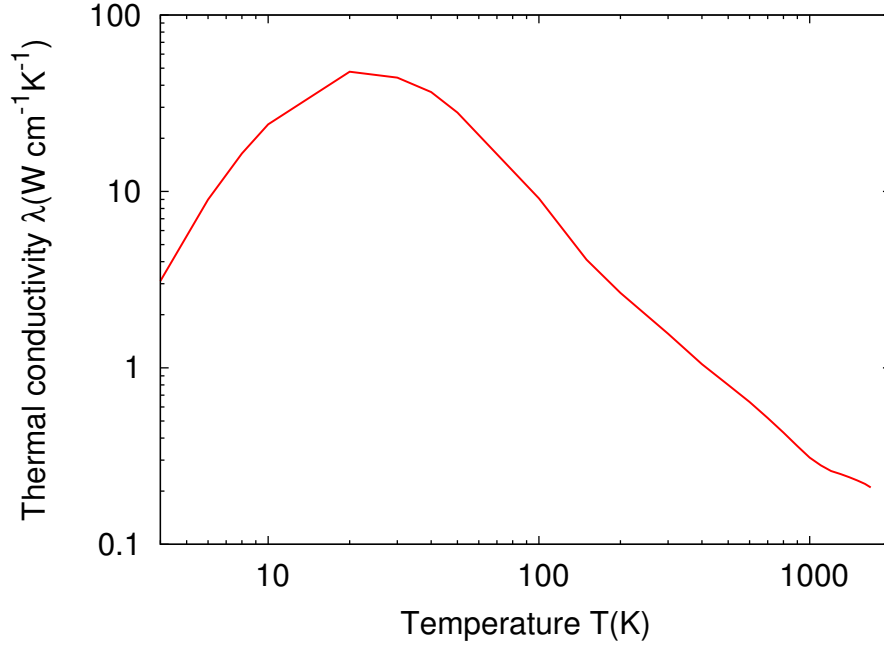


Figure 3.15: *Temperature dependence of thermal conductivity* [117].

Applying Eq. 3.7 to such small (atomistic) length scale may appear questionable, but many authors assume that the standard heat conduction theory can be applied to describe the energy dissipation of the thermal spike [15, 108, 121–123]. As a consequence of Eq. 3.1 any temperature disturbance will propagate at an infinite velocity through the media [124, 125]. Indeed, the simulated heat transport is too fast at short times. Assuming a finite heat velocity in the heat transport equation Cattaneo and Vernotte have obtained the hyperbolic heat conduction equation [111, 114, 124–127], which assumes the finite heat flow determined by the phonon relaxation time. This equation is not only numerically complicated to solve, but can also lead to the unphysical results, like negative temperatures [126] or singularities associated with the interaction of a wave front and a boundary [128]. In order to avoid these inconsistencies the numerical solution of the hyperbolic heat equation would be rather time consuming [128], where the main advantage over MD simulations could be lost. In addition the main deviation of the Fourier compared to the non-Fourier law are reported to be at a very short time scales [126]. Since we are only interested in the overall number of molten atoms and not in every detail of the time evolution of the temperature field we

assume that this model is applicable to our problems. We also assume that taking into account the geometrical distribution of initial energy deposition and to obey energy conservation, as is done in our approach, are the most important features of amorphous pocket simulations.

The temperature dependence of various physical parameters, such as the specific heat and the thermal conductivity can be included in the simulations, if necessary. The experimentally measured thermal dependence of the specific heat and the thermal conductivity of crystalline silicon are presented in Figs. 3.14 and 3.15, respectively [117]. For the thermal conductivity in the temperature range above the melting temperature the dependence described by the Wiedmann-Franz law [129–132] can be used. The variation of the specific heat in the temperature range above the melting temperature is not significant, therefore the value at the melting temperature can be used.

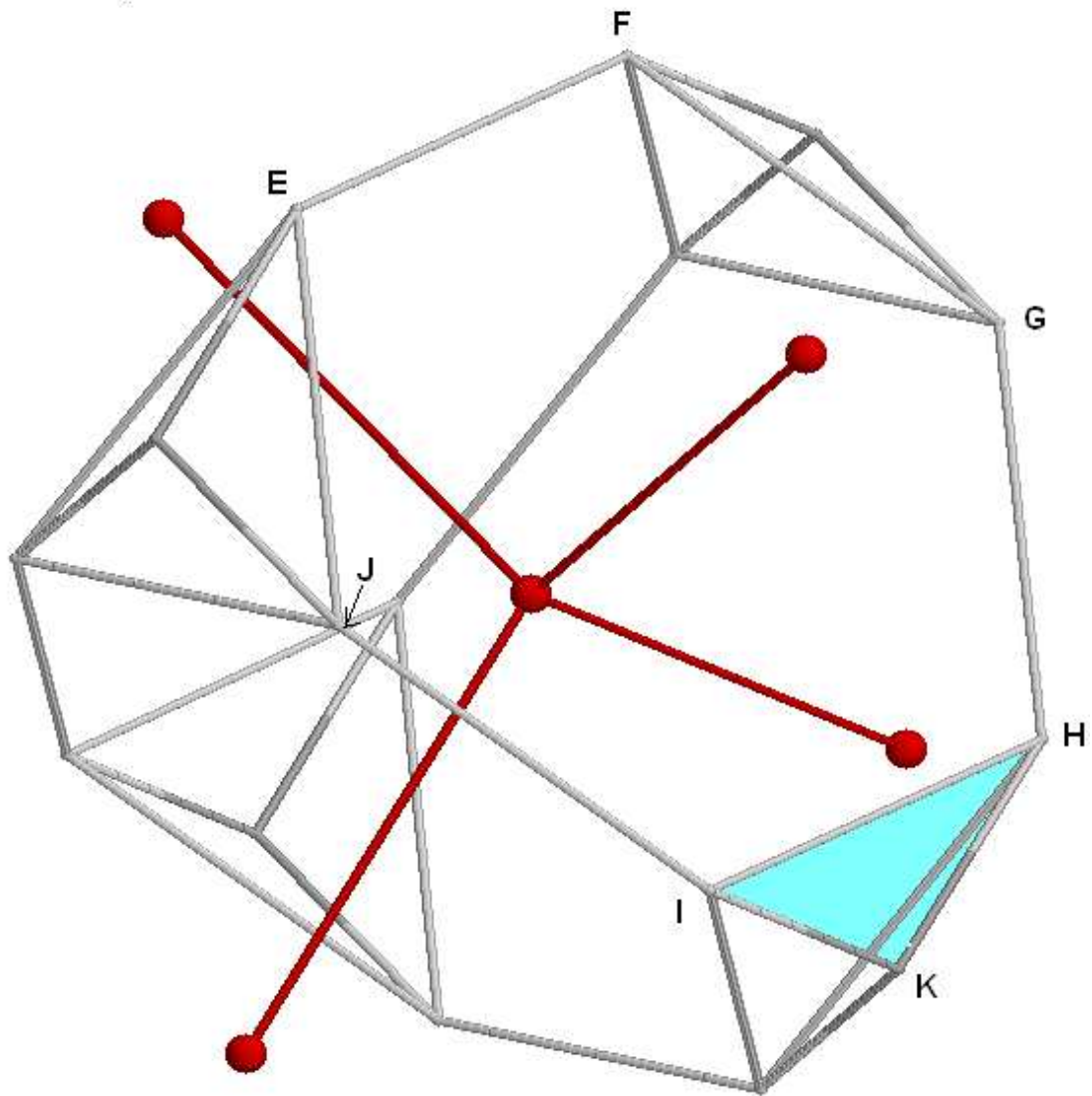


Figure 3.16: Applied geometrical discretization. Finite volume that encloses silicon atom (in the center) and the four nearest neighboring atoms, presented with dark ball and stick models. The volume is defined by 4 symmetry planes of the distance between the atom and its 4 nearest neighbors (i.e: regular hexagon \overline{EFGHIJ}), and by 12 triangles in the planes perpendicular to the direction of atom's second nearest neighbors (Shaded triangle \overline{IKH} represents one of the 12 triangles).

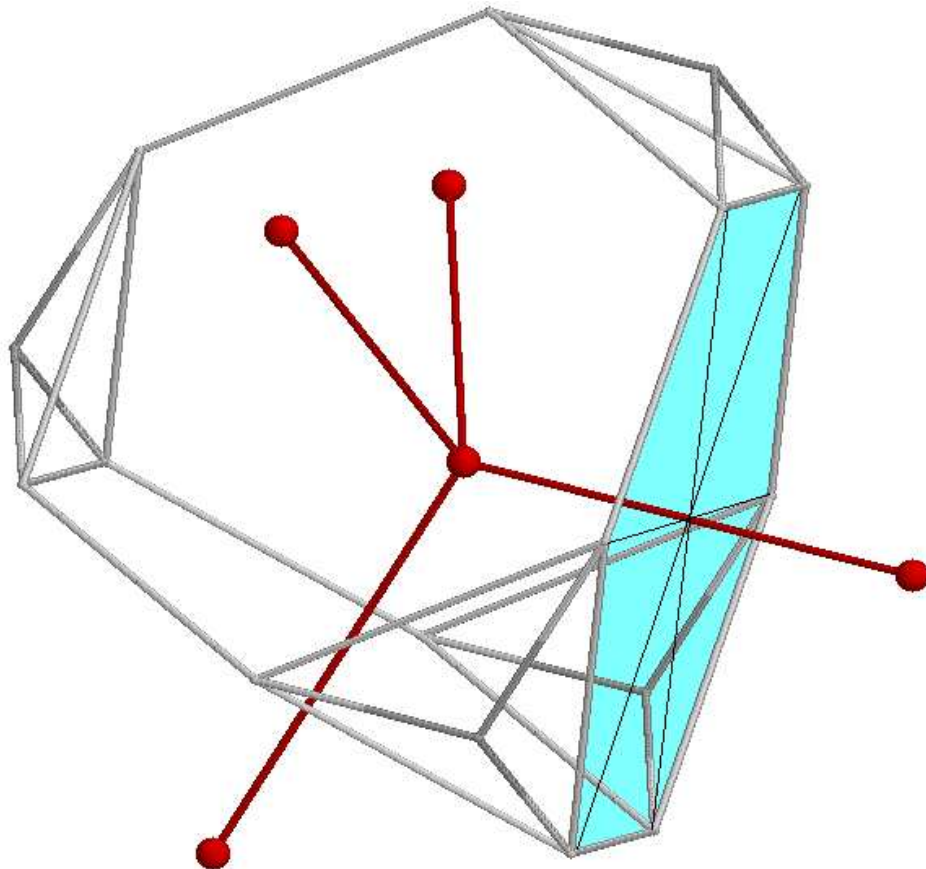


Figure 3.17: *Illustration of the geometrical relation of two neighboring volumes and the surface through which heat flux flows. Only one surface area is indicated, while the relation with the other three neighbors is completely symmetric. The shadowed hexagon represents the area through which the heat flows occurs. Note that the hexagon is placed in the midplane perpendicular to the distance between two atoms and intersects the bond exactly at its center.*

The space is discretized with finite volumes on grid points that coincide with the crystallographic lattice sites. The applied geometrical discretization with the corresponding body defining the volume of the grid point, and the relevant areas used for the heat flow are presented in Fig. 3.16. The silicon atom is presented by the black sphere in the center together with its 4 nearest neighbors (4 other black spheres) and the corresponding atomic bonds (sticks between the atom and its neighbors). The volume is defined by the symmetry planes at the distance between the atom and its 4 nearest and 12 second nearest neighbors. From Fig. 3.17 we can clearly see that the intersection area between two neighboring volumes is the regular hexagon \overline{EFGHIJ} (for each neighbor one), placed in the midplane perpendicular to the distance between two atoms. The hexagon intersects the bond between two atoms exactly in its center and in the middle of the bond. 12 further triangles define the surface area in the planes between the atom and its second nearest neighbors. One of the triangles \overline{IKH} is shadowed in Fig. 3.16.

From Fig. 3.17 we see that the spacing between the neighboring grid points coincides with the nearest neighbor distance between the silicon atoms and is given by

$$\Delta x = a_{latt} \frac{\sqrt{3}}{4} \quad (3.8)$$

where $a_{latt} = 5.43 \text{ \AA}$ is the lattice constant of silicon.

The volume of the grid element, defined by the body enclosing the silicon atom (See Fig. 3.16) is the silicon atom volume:

$$V = V_{atom} = \frac{a_{latt}^3}{8} \approx 2.0 \times 10^{-29} \text{ m}^3 \quad (3.9)$$

Using the geometry illustrated in Figs. 3.16 and 3.17 we can write down the equation for the heat flux conservation (Eq. 3.6) in integral form:

$$\int_V \frac{\partial E(\vec{r}, t)}{\partial t} dV = - \int_V V \nabla \vec{q} dV \quad (3.10)$$

Applying the Gauss-Ostrogradsky theorem [133], which says that the surface integral of a vector over a closed surface equals the volume integral of the divergence of

that vector integrated over the volume enclosed by the surface, we write

$$\int_V \frac{\partial E(\vec{r}, t)}{\partial t} dV = -V \int_S \vec{q} d\vec{S} \quad (3.11)$$

where S is the surface enclosing the body in Fig. 3.16. The surface vector is oriented so that it points out of the node volume. Since the node volume V is a constant it is placed in front of the integral. To simplify our calculations we assume that the heat flow between the atom and its second nearest neighbors can be neglected. From this assumption it follows that the heat flows only between the atom and its first neighbors through the regular hexagons, as it is shadowed in Fig. 3.17. The surface of the hexagon is

$$S_{hex} = 6 \cdot a^2 \frac{\sqrt{3}}{4} = a_{latt}^2 \frac{3\sqrt{3}}{16} \quad (3.12)$$

Where the relation between the edge of the regular hexagon a and the silicon lattice constant has been used

$$a = \frac{\sqrt{2}a_{latt}}{4} \quad (3.13)$$

Using the geometrical relation and introduced assumption the surface integral in Eq. 3.11 becomes

$$\int_S \vec{q} d\vec{S} = \sum_{j=1}^{j=4} q_{i,j} \vec{S}_{hex} = \sum_{j=1}^{j=4} q_{i,j} S_{hex} = S_{hex} \sum_{j=1}^{j=4} q_{i,j} \quad (3.14)$$

S consists of 4 equal hexagons (for each neighbor one), thus S_{hex} can be placed in front of the sum. Also, considering geometrical relation in Fig. 3.17 the scalar product in Eq. 3.14 is replaced by the plain product, since the surface is placed perpendicular to the heat flux (the surface vector is parallel to the heat flux vector). Index i represents the particular atom and index i, j denotes its j^{th} neighbor. Introducing Eqs. 3.9, 3.12 and 3.14 into Eq. 3.11 we obtain

$$\int_V \frac{\partial E(\vec{r}, t)}{\partial t} dV = -V \frac{3\sqrt{3}}{16} a_{latt}^2 \sum_{j=1}^{j=4} q_{i,j} \quad (3.15)$$

Assuming that the energy is constant over the atom volume, the integral in 3.15 can be replaced by product

$$V \frac{\partial E(\vec{r}, t)}{\partial t} = -V \frac{3\sqrt{3}a_{latt}^2}{16} \sum_{j=1}^{j=4} q_{i,j} \quad (3.16)$$

Thus

$$\frac{\partial E(\vec{r}, t)}{\partial t} = -\frac{3\sqrt{3}a_{latt}^2}{16} \sum_{j=1}^{j=4} q_{i,j} \quad (3.17)$$

For the space derivatives in Eq. 3.1 we have the following difference equation:

$$\nabla T(\vec{r}, t) = \frac{T_{i,j}^n - T_i^n}{\Delta x} \quad (3.18)$$

Where $T_i^n, T_{i,j}^n$ denote the temperature of the atom and its j^{th} neighbor, respectively. Therefore the difference equation describing the heat flow between the atom i and its j^{th} neighbor reads

$$q_{i,j} = -\lambda(T) \frac{T_{i,j}^n - T_i^n}{\Delta x} \quad (3.19)$$

Using the Euler forward finite difference scheme, the time derivative in Eq. 3.17 can be replaced by the following difference equation:

$$\frac{\partial E(\vec{r}, t)}{\partial t} = \frac{E_i^{n+1} - E_i^n}{\Delta t_n} \quad (3.20)$$

E_i^{n+1} represents the node energy for the next time step while E_i^n is the node energy in the current time step. The spacing of the timestep t_n is

$$\Delta t_n = t_{n+1} - t_n \quad (3.21)$$

The index n of the timespacing indicates that the spacing in time need not to be constant.

Introducing Eqs. 3.19 and 3.20 into Eq. 3.17 we obtain:

$$\frac{E_i^{n+1} - E_i^n}{\Delta t_n} = \frac{3\sqrt{3}a_{latt}^2}{16} \sum_{j=1}^{j=4} \lambda(T) \frac{T_{i,j}^n - T_i^n}{\Delta x} \quad (3.22)$$

From Eq. 3.8

$$\frac{E_i^{n+1} - E_i^n}{\Delta t_n} = \frac{3a_{latt}}{4} \sum_{j=1}^{j=4} \lambda(T) (T_{i,j}^n - T_i^n) \quad (3.23)$$

The temperature dependence of the thermal conductivity can be approximated as the average of the atom's thermal conductivity and the thermal conductivity of its neighbor

$$\frac{E_i^{n+1} - E_i^n}{\Delta t_n} = \frac{3a_{latt}}{4} \sum_{j=1}^{j=4} (T_{i,j}^n - T_i^n) \frac{(\lambda_{i,j}^n + \lambda_i^n)}{2} \quad (3.24)$$

Solving the previous equation for the grid energy at the new timestep E_i^{n+1} we finally obtain the numerical form of the energy balance equation (Eq. 3.7):

$$E_i^{n+1} = E_i^n + \Delta t_n \cdot \frac{3a_{latt}}{8} \cdot \sum_{j=1}^{j=4} (\lambda_{i,j}^n + \lambda_i^n) (T_{i,j}^n - T_i^n) \quad (3.25)$$

The applied forward Euler algorithm, called explicit timestepping, uses the grid values of only the previous timestep (index n , $t = t_n$) to calculate those of the next (t_{n+1}). In this case, the spatial derivatives will be evaluated at timestep n and the time derivatives at $n + 1$ timestep. In other words each new energy at timestep $n + 1$ is calculated independently, so it does not require simultaneous solution of system of equations, which can be memory and time consuming. But on the other hand the disadvantage of explicit timestepping algorithms is conditional stability, which means they are limited to smaller timesteps than the implicit ones. Applying von Neumann stability analysis [134] we obtain maximum time step for the stable numerical solution:

$$\Delta t_n \leq \frac{a_{latt}^2}{24 \cdot D} \quad (3.26)$$

where D denotes the thermal diffusivity of silicon and can be calculated from the

corresponding values of the specific heat and thermal conductivity

$$D(T) = \frac{\lambda(T)}{\rho \cdot c_p(T)} \quad (3.27)$$

Taking into account the temperature dependence of the thermal diffusion $D(T)$ in Eq. 3.26 the requirement for the maximum timestep becomes

$$\Delta t_n \leq \min_j \left[\frac{\Delta x}{4 \cdot D_{i,j}} \right] \quad (3.28)$$

where the minimum is over the four nearest neighbors. In Eq. 3.28 $D_{i,j}$ reads

$$D_{i,j} = \frac{D(T_{i,j}^n) + D(T_i^n)}{2} \quad (3.29)$$

Applying Eq. 3.28 for each atom and before each time step we secure that our system is stable. As a consequence the calculated timestep varies through successive time steps being adapted to the maximal possible value. This technique is called adaptive time stepping.

3.4.2 Program details

The principles of the program are outlined in the following sections and summarized in Fig. 3.18.

The first step consists of calculating the collision cascade by binary collision simulation code “IMSIL”. The geometrical distribution and remaining energy of the energetic atoms and stopped recoils is obtained. Next, the initial conditions for the heat transport simulations are calculated, where the remaining energy of the energetic atoms is assigned to their nearest lattice sites, as it is explained in Section 3.4.2.2. Since in Eq. 3.25 we need both energy and temperature, the energy of atoms is converted to the temperature according to the procedure explained in Section 3.4.2.3. In the next step the size of the simulation cell and the boundary conditions for the heat flow are determined. Afterwards, heat transport is simulated according to the numerical solution described in Section 3.4.1. During the heat quenching the distribution of atoms

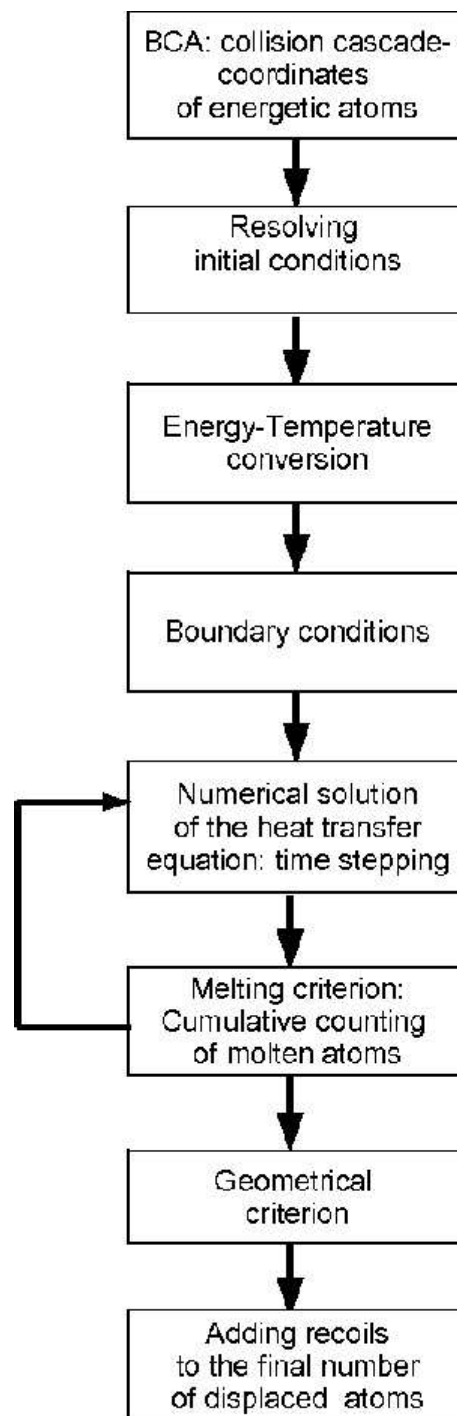


Figure 3.18: *Flowchart of amorphous pocket simulation program.*

labeled as “molten” is built up cumulatively, i.e. an atom is considered molten if it ever has met the melting criterion, explained in Section 3.4.2.5. The simulation is performed until the energy deposited through the ion implantation is dissipated in the surrounding crystal. In the next step a second (labeled as “geometrical” in Fig. 3.18) criterion is applied to the molten zones, obtained by the heat transport simulation. Applied criterion is explained and described in Section 3.4.2.6. Finally, the distribution of recoiled atoms is added to the final number of displaced atoms according to the procedure outlined in Section 3.4.2.7. The detailed description of each step of the program is given in the following sections.

3.4.2.1 Binary Collision simulation of collision cascade

Using the binary collision code “*IMSIL*” [8] the geometrical distribution of energy deposited in nuclear collisions is obtained. The coordinates and energies of the energetic atoms are calculated simulating full collision cascades of the ion and all subsequent secondary and higher order recoils down to the cut-off energy where they are not able to produce further displacements. Value of 5 eV is used as the displacement and cut-off energy. Since the used value is smaller than the standard silicon displacement energy of 15 eV it yields a larger number of the recoils produced in the collision cascade. It is important to remark that this distribution of recoils is used only to determine the initial energy deposition profile, and not to gain the final number of recoiled atoms. In order to obtain a correct number of recoiled atoms, an additional simulation of the collision cascade, with the standard value for the displacement energy (15 eV), will be performed as it is explained in Section 3.4.2.7.

The decision for using 5 eV for the cut off and displacement energy is motivated by the following: The energy profile obtained using 15 eV for the displacement and cut-off energy gives the initial energy sources up to the displacement energy value. This energy, when converted into temperature (see Section 3.4.2.3), would give extremely large temperature sources of about tens thousands of Kelvin. Since the surrounding crystal atoms have substrate temperature up to few hundreds of Kelvin, it would introduce strong local temperature disturbances in the material. On the other side, Eq. 3.1, has limited validity in systems with a strong temperature disturbances, and its applicability is mainly localized to the thermodynamic limit, i.e. at time scales typically greater than several phonon relaxation times and to the space scales of weak local temperature

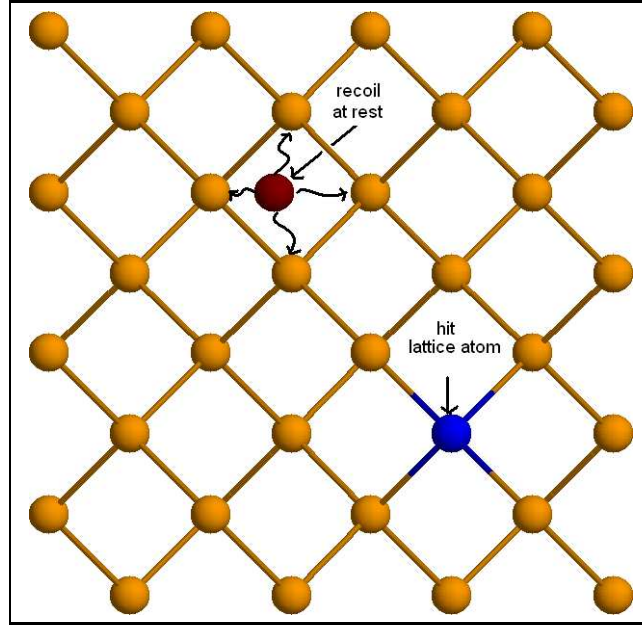


Figure 3.19: *Illustration of resolving of the initial conditions. Recoiled atoms at rest share its energy to the neighboring lattice sites. Hit lattice atoms denotes the atoms which experienced collision with moving ion, but the received energy was below displacement threshold and the atom remains at its lattice site with received amount of energy.*

disturbances [126]. Therefore, in order to overcome this limitations and avoid large temperature discontinuities we have used 5 eV for the cut-off and displacement energy for the collision cascade simulations. Decrease of these values from 15 to 5 eV effectively means that the certain level of the heat dissipation is already performed in the binary collision part of the simulation, which smooths the initial temperature profile for the following heat flow process. Another reason for choosing $E_d = 5\text{eV}$ is given in Section 3.4.2.5

3.4.2.2 Resolving initial conditions

The process of determining the initial conditions is illustrated in Fig. 3.19. As a result of the BC simulation the distribution of the energetic atoms is obtained. From the modeling point of view two types of initial energy sources are distinguished. First

type are the atoms which have experienced a subthreshold collision during collisional phase of the ion impact, i.e. they were not able to start movement. These hit atoms remain at their lattice sites in an excited vibration state, releasing the received energy through phonons. Their deposited energy is assumed to be converted into the heat of the corresponding lattice site. Second type of the energy sources represent the recoiled lattice atoms which have been displaced from their lattice sites and set into motion. After they have lost their energy due to electronic and nuclear stopping they come to the point where they are no more able to produce further displacements, i.e. they come to rest in the host lattice. These atoms represent interstitial atoms embedded in the Si lattice, and their remaining energy is shared equally between the neighboring lattice atoms. The neighboring lattice sites are defined within the radius of 2.35\AA , what corresponds to the nearest neighbor distance in silicon. Additional treatment of recoils is explained in Section 3.4.2.7.

3.4.2.3 Material parameters and Energy-Temperature dependence

Considering that all energy deposited in initial sources is instantaneously converted into heat, a temperature can be assigned to each atom giving rise to temperature gradients for the heat diffusion. The energy-temperature dependence is illustrated in Fig. 3.20 for the case of constant value of the specific heat.

Eq. 3.3 is modified to consider the heat of melting when the melting temperature is crossed at any point in space. With this consideration we take into account the potential energy and phase change when an atom melts. Furthermore, we assume that the energy once spent for melting an atom, will be stored into the lattice crystal. This prevents that this energy, once spent for melting an atom, eventually again contributes to melting of neighboring atoms. The energy stored into crystal is taken to be equal to the heat of melting. In other words, once an atom crosses the melting temperature his cooling branch has different behavior from the atoms whose temperature has never reached the melting temperature. Using these two assumptions we obtain the following equations for the conversion of the deposited energy per atom to the equivalent temperature.

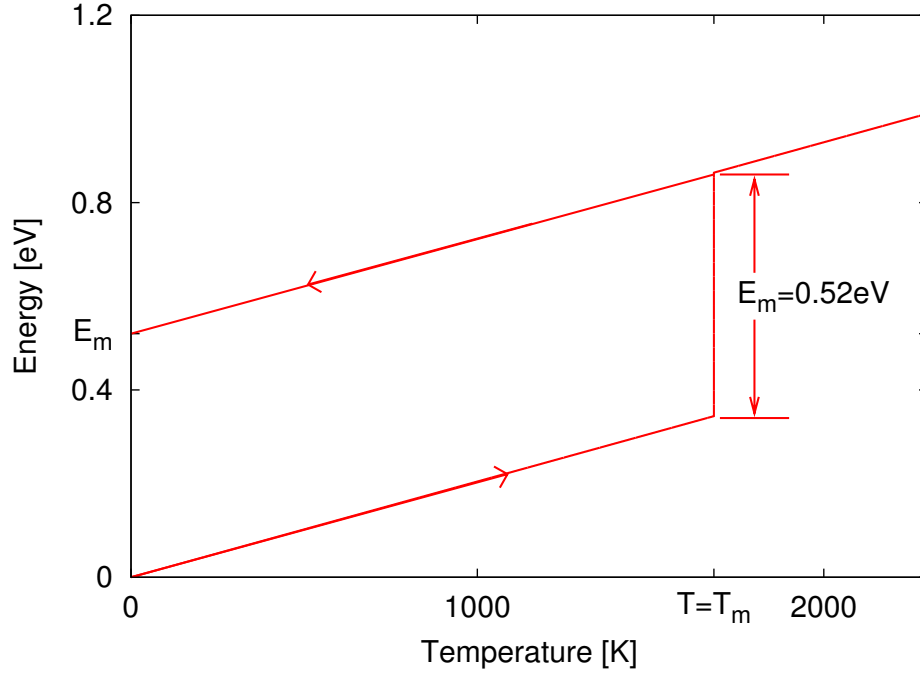


Figure 3.20: Dependence of energy per atom on temperature, presented, for simplicity, for the constant value of the specific heat. It shows energy temperature dependence according to Equations 3.30, 3.31 and 3.32. It includes the heat of fusion when an atom crosses the melting temperature and the energy stored into the crystal after an atom melts. T_m denotes the silicon melting temperature and has value of 1683K.

Not molten atoms:

$$E(T) = \rho \cdot V \int_0^T c_p(u) du \quad \text{for } T \leq T_m \quad (3.30)$$

$$T = T_m \quad \text{for } E(T_m^-) < E < E(T_m^-) + E_m \quad (3.31)$$

Molten atoms:

$$E(T) = \rho \cdot V \int_0^T c_p(u) du + E_m \quad (3.32)$$

V represents the atom volume given by Eq. 3.9 and $E_m = 0.52 \text{ eV}$ is the heat of melting per atom for silicon. The integral in equations 3.30 and 3.32 is calculated by numerical integration and trapezoidal rule:

$$E(T) = \sum_{i=1}^n \rho \cdot c_p(i\Delta T) V \Delta T \quad (3.33)$$

where the temperature resolution step of $\Delta T = 1K$ is found to be small enough to provide negligible numerical error. In order to keep simulation times reasonable the energy temperature dependence given with Equations 3.30, 3.31 and 3.32 is calculated once at the initialization part of the program, and during the heat simulation the required values of energy (temperature) are obtained by linear interpolation performed by the binary search procedure.

We have run several simulations taking into account the temperature dependence of the specific heat and the thermal conductivity in Eqs. 3.30 and 3.32. The results were rather similar to those obtained when neglecting these dependencies, but computational times were up to two orders of magnitude longer. In order to avoid too large computational times, to obtain the results which will be presented in the following, we will use the constant parameter values. In this case the integrals in Eqs. 3.30 and 3.32 are replaced by simple products. Since the focus of our investigation is the melting process of atoms, the appropriate values for the specific heat and the thermal conductivity would be those at the melting temperature. The following values are used: $c_p(T_m) = 1017 \text{ J/kgK}$ for the specific heat, $\lambda(T_m) = 21[W/(mK)]$ for the thermal conductivity [135]. Silicon melting temperature is $T_m = 1683K$ and the Si mass density ($\rho = 2330 \text{ kg/m}^3$) [135].

However, the aim of the presented heat flow model is not to describe quantitatively every detail of the temperature evolution in the sample, than to obtain a physically based reasonable estimation of the number of molten atoms upon ion implantation, with the available computational cost. Therefore the limitation imposed by neglecting the full temperature dependencies of the material parameters should not be critical.

3.4.2.4 Boundary conditions

After introducing the initial conditions into the system, the size of the simulation cell is determined so that it covers the distribution of the energetic atoms. In order to allow uninterrupted heat flow outside the cell from the bordering atoms, the cell is extended in all three direction for several unit cells. It has been found that extending the simulation cell for more then 3 unit cell does not change the number of molten atoms. Therefore, the value of 3 is chosen. The boundary layers of the simulation cell are connected to a thermal reservoir of constant temperature, namely substrate temperature, to simulate the heat transport outside the cell.

3.4.2.5 Melting criterion during heat quenching

During the heat quenching phase the melting criterion has to take into account the basic assumption confirmed by molecular dynamics simulation [2], which says that a single energetic atom in an otherwise perfect crystal does not produce damage if its energy is less than the displacement energy for silicon ($E_d = 15\text{eV}$). Therefore, we have to include in our model that the creation of amorphous zones should be the result of overlapping of nearby energetic atoms and not the result of isolated recoiled atoms. In other words, the isolated initial sources with energy up to the threshold displacement energy must not produce damage. In order to choose appropriate melting criterion, which is able to take into account mentioned assumption, the following simulations are performed. One atom in the center of the large simulation cell is given energy going from 1eV to 15 eV, and the heat transport is simulated. The number of molten atom is detected. Intuitively, an atom may be labeled “molten” when its temperature exceeds the melting temperature T_m , as we have used it in Section 3.4.2.3. From Fig. 3.21 we see than one single isolated energy source can lead to melting up to 5 atoms according to this simple criterion, what is in contrary to the starting assumption. Therefore, the melting criterion that labels an atom as “molten” whenever its energy crosses the melting temperature is not appropriate for describing the melting process. Furthermore, the concept of a single molten atom is problematic, and melting makes sense only for larger volumes.

In order to avoid problematic concept of a single molten atom, before labeling an atom as molten we require that not only this atom but in addition at least some of its

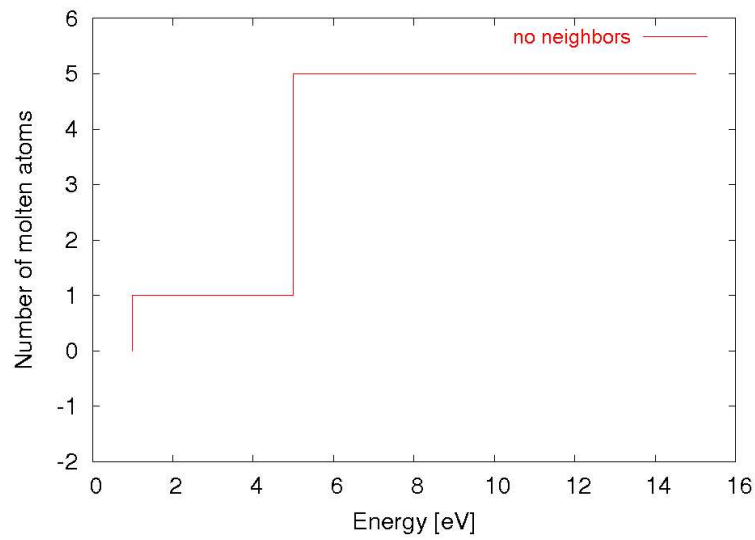


Figure 3.21: Number of molten atoms as a function of energy stored into atom using criterion that an atom is molten whenever its temperature crosses the melting temperature.

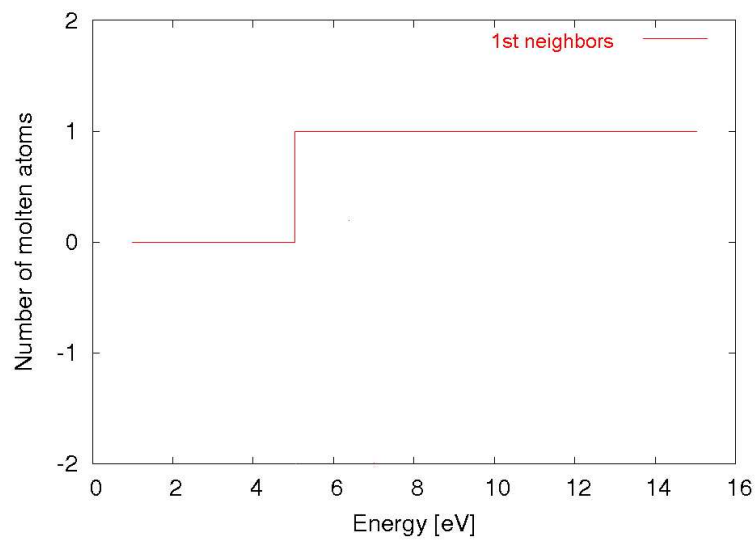


Figure 3.22: Number of molten atoms as a function of energy stored into atom using melting criterion which requires that not only atom but also its neighboring atoms cross the melting temperature.

neighbors cross the melting temperature. In Fig. 3.22 we present the number of molten atoms versus energy when the melting criterion is met by the nearest neighbors. From the figure we see that requiring that the criterion is met by the first neighbors does not melt any additional atom in the energy range up to 5 eV and induce melting of one additional atom in the energy range between 5 and 15 eV. Since the cut-off energy in our simulations is 5 eV, we assure that the atom energy will not exceed this value. Keeping in mind that the test problem has radial symmetry the results presented in the Fig. 3.21 are the same when the number of molten neighbors is required to be either 1 up to maximum 4 nearest atoms. The particular value will be fitted when compared to experimental values.

3.4.2.6 Geometrical criterion based on critical point defect density

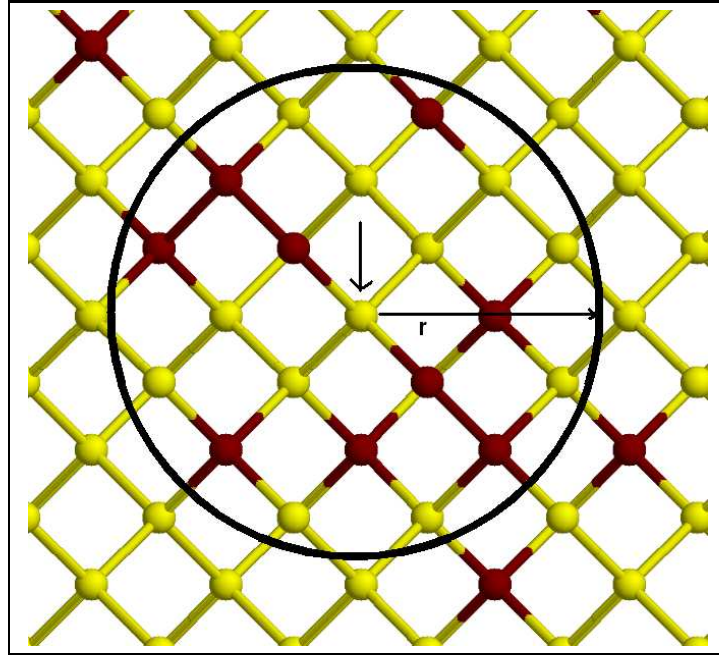


Figure 3.23: *Illustration of geometrical criterion. Within the given radius a minimum density of molten atoms has to be exceeded in order to label an atom as molten (with arrow). Dark atoms represent “molten” atoms according to previous heat transport simulations and light colored crystalline atoms.*

As we will show in Section 3.5, the heat conduction law alone is not capable to either quantitatively or qualitatively predict the experimental data on the ion mass and polyatomic effect, even if the melting criterion described in Section 3.4.2.5 is taken into account. Therefore, an additional criterion is applied to the distribution of molten atoms obtained with the heat conduction simulation and the melting criterion from the previous section.

As it is known from experimental results [7] and ab-initio and molecular dynamics simulations [136] when the local defect density in the lattice exceeds the critical value the lattice collapses in these regions occurs. Considering the configuration of molten atoms obtained by the heat transport simulator and the melting criterion during the heat quenching the procedure illustrated in Fig. 3.23 is applied. For each atom in the cell the local concentration of the molten atoms contained in the sphere defined within the given radius, with center in the investigated atom, is examined. If the concentration of molten atoms exceeds a threshold the atom is labeled as “amorphous”, if not it is crystalline. The loop is done for all atoms in the cell, and new final configuration of amorphous atoms is obtained. The term “amorphous” is used in order to avoid eventual confusion with the term “molten” used for the atoms which are considered as molten during the heat quenching phase. Applying this criterion the amorphization of small clusters, eventually single isolated atoms, is further penalized while the continuous larger pockets are favored what is in agreement with the MD results [2]. Also compactness of the amorphous zones is obtained, i.e. if the molten zone contains some crystalline atoms the local collapse of the lattice occurs leading to the amorphization of these atoms. This criterion allows better taking into account the spatial correlation between the different molten atoms than it is possible in the heat flow simulations even when the melting criterion that meets first neighbors is used. Applying the criterion of the minimum density of molten atoms after the heat transport simulation we have assumed that the melting process occurs on the smaller time scale than the lattice collapse. It is shown that for high energy deposition the zones can melt on the subpicosecond time scales [58, 123] while the lattice collapse occurs later.

3.4.2.7 Counting recoils in the final number of displaced atoms

The second type of the energy sources discussed in Section 3.4.2.2 represents the recoiled atoms that are already slowed down and came to rest in the host lattice. As we

have explained in Section 3.4.2.2 the energy of these recoils is already shared with the neighboring atoms and subsequently used for the heat flow simulations. In addition these atoms represent the interstitials placed into the host lattice and their presence has to be taken into account in the final number of displaced atoms. After the heat is dissipated and the final number of amorphous atoms according to criterion explained in Section 3.4.2.6 is obtained, the distribution of recoiled atoms is obtained by BC simulation and added to the final number of displaced atoms according to the following procedure.

The contribution of each interstitial to the final distribution of displaced atoms depends on the experimental method used for the damage measurement. The experimental data used for the comparison, presented in Figs. 3.1 and 3.4, are obtained by RBS/C in situ measurements. The reported number of displaced atoms per incident ion is extracted from experimental RBS/C spectra assuming that the damage is in the form of randomly displaced atoms surrounded with the perfect lattice. The simple procedure of damage quantification from the experimental RBS/C spectra is introduced in Section 4.1.

The model of random interstitial surrounded by the perfect lattice neglects the strain in neighboring lattice sites and leads to overestimation of the damage in the sample [48, 52, 77] as we will show in Section 4.4. Instead, each interstitial is assumed to be equivalent to two displaced atoms, since the majority of interstitials are in the split- $\langle 110 \rangle$ interstitial configurations according to the MD simulations [95]. The efficiency of the split- $\langle 110 \rangle$ interstitial on the RBS/C spectra is investigated with the procedure described in detail in Section 4.4. According to the results from Section 4.4 each split- $\langle 110 \rangle$ interstitial has about 2 times larger efficiency, compared to the random interstitial. Therefore, each recoil, obtained by BC simulations, will be multiplied by 2 and added to the previously obtained number of amorphous atoms. This yields the final number of displaced atoms.

In Section 3.4.2.2 for the purpose of determination of the initial temperature profile we have used 5 eV as the displacement energy, which gives a larger number of recoiled atoms than obtained with the standard value of 15 eV. In order to obtain the correct number and distribution of recoils parallel simulation of the collision cascade, with the value of 15 eV as the displacement energy, is performed and the equivalent number of recoils is obtained. The distribution of recoils is compared with the distribution of the

obtained amorphous zones. Only the recoils which are not contained in the already amorphous zones are added to the final number of displaced atoms, according to the above described procedure.

3.5 Results and discussion

For the purpose of testing our model we have compared our simulation results with the experimental data published on the ion mass and polyatomic effect [6].

3.5.1 Ion Mass Effect

We have simulated collision cascades of P, As, Te, Tl in Si for different ion implant energies, and compared our results with the experimental results [6] obtained at cryogenic temperatures (35 K).

In Fig. 3.24 we present the number of displaced atoms per incident ion as a function of energy deposited in nuclear collisions, what is a monotonic function of implant energy. Solid lines represent the experimental results, while dashed lines represent the results of the proposed amorphization model. About 100 simulations is performed in order to obtain statistical quality of the data. The reported values of the energy deposited in nuclear collisions are calculated as the statistical average of the values obtained by simulating many cascades with one particular ion implant energy. Similarly, the corresponding number of displaced atoms per incident ion is obtained as the average of the values obtained by simulating the heat flow/lattice collapse using many BC cascades with the same ion implant energy, previously used to calculate the corresponding value of energy deposited in nuclear collisions. The final number of amorphous atoms is calculated by applying both criteria described in the previous sections. During the heat quenching it was required that all four nearest neighbors meet the melting criterion before labeling one particular atom as molten. The amorphization threshold values fitted to the experimental results are 8Å for the melting radius and 10% for the minimum concentration of molten atoms. The number of recoils is multiplied with 2 and included in the final number of displaced atoms.

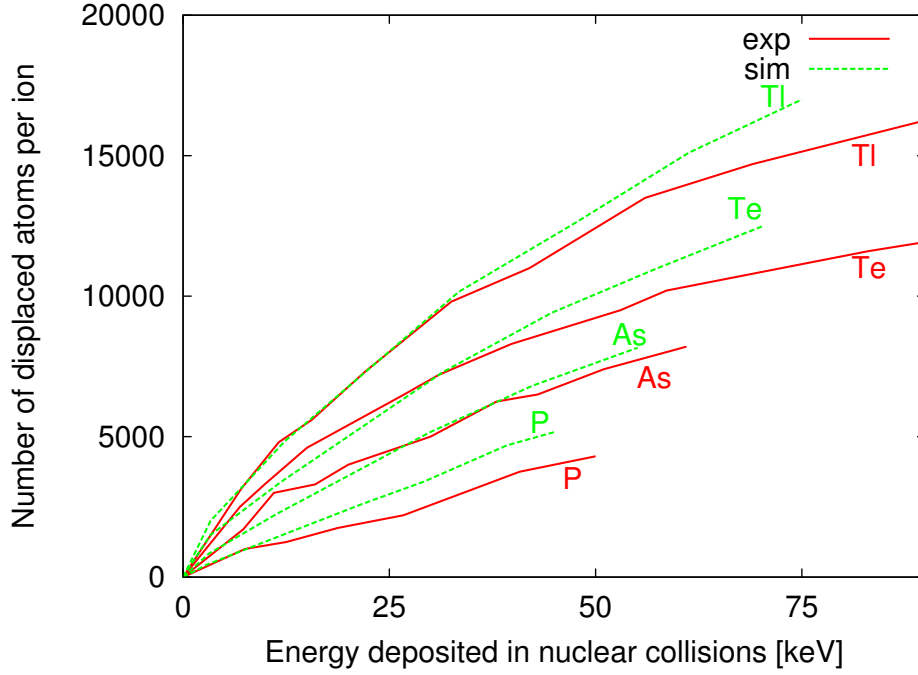


Figure 3.24: Number of displaced atoms per incident ion versus energy deposited in nuclear collisions. Experimental results - solid lines [6]. Simulation results: dashed lines - criterion requires that at least 4 neighbors meets the melting criterion before one atom is considered molten and in addition requires that minimum 10% of molten atoms exists within the volume of the sphere with radius of 8\AA .

From the results presented in Fig. 3.24 we can see that the model correctly describes the ion mass effect for all implanted ion species. It also produces correct energy dependence of the number of displaced atoms per incident ion. We can conclude that the presented model gives qualitative and in a large amount quantitative description of both the ion mass and the energy dependence of the ion mass effect at cryogenic temperatures.

However, the presented results show that the model slightly overestimates the number of displaced atoms for all ion species in the high energy range. In this range the influence of the amorphous pockets should be weaker compared to point defects, as discussed in Section 3.2.1. The discrepancy between the experimental and simulated values is most pronounced for phosphorus, which is the lightest ion used, where the

influence of the amorphous pockets is also expected to be of a minor role. Therefore, one of the reasons for the deviation of the model can be assigned to the uncertainty of the actual defect types present in the sample and their contributions to the RBS/C signal. The value of 2 used for counting the recoiled atoms favors split- $\langle 110 \rangle$ interstitials. Although MD simulations have shown that most of the damage is the form of split- $\langle 110 \rangle$ interstitial, in reality the damage usually consists of a mixture of different defect types, with unknown abundance, what contributes to the discrepancies. Furthermore, amorphous atoms obtained by the heat transport simulation/lattice collapse are according to the experiments in the random interstitial form and their contribution to the RBS yield is taken into account as +1 defect. Since the efficiency of the atoms contained in the amorphous pockets to the RBS/C yield is not precisely known this can be also the source of the deviation of the simulated results.

In order to demonstrate the importance of each part of the proposed model, we now show results at intermediate steps of model development. First we show that the heat conduction law modified to include the heat of melting is not capable to describe the process of amorphous pockets creation.

In Fig. 3.25 simulations with different applied criteria are compared with the experimental results (solids). The line labeled by “without Em” represent the results of Vineyard’s model which does not take into account the heat of melting. These results are obtained with the proposed heat flow model without considering the heat of melting or the lattice collapse. An atom is labeled as molten if its temperature crosses the melting temperature. Obviously the heat flow model based on Vineyard’s assumption highly overestimates the experimental results. Although taking into account the heat of melting (dashed lines labeled with “with Em” in Fig. 3.25) in the heat transport simulations has quantitatively improved the overall description of the experimental results the deviations are still significant. The model still does not give any ion mass dependence and highly overestimates the number of defects at higher energies. Requiring, in addition, that the average energy of the atom and its neighbors meets the melting criterion [36] further decreases the number of displaced atoms and yields slight ion mass dependence. The results of averaging over atoms up to second nearest neighbors are shown in Fig. 3.25 by dotted lines. However, despite small ion mass effect, this assumption still does not qualitatively improve the result and introduces also coupling within the second neighbors, during the heat quenching, what is physically questionable.

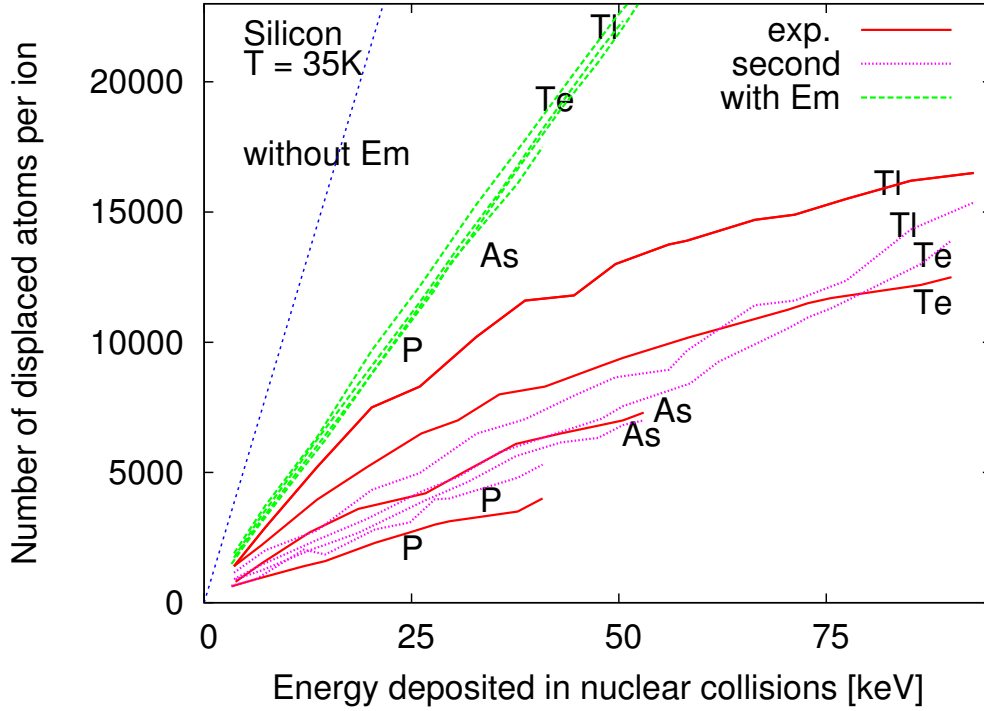


Figure 3.25: Number of displaced atoms per incident ion as a function of energy deposited in nuclear collisions for various implanted species, and various criterion applied in the simulations. Experimental results - solid lines [6]. Dotted lines - criterion with heat of melting and second nearest neighbors. Dashed lines - criterion with only heat of melting. The line labeled with “without Em” represents the results with no heat of melting included [106].

Taking into account the “heat of crystal” and using the number of molten neighbors that cross the melting temperature from the melting criterion described in Section 3.4.2.5 as a fitting parameter leads to the results presented in Fig 3.26. The results presented in Fig 3.26 represent the best fitting obtained requiring that minimum three neighbors meet the melting temperature. From the figure we can conclude that the model does not also gain the satisfying ion mass and energy dependence.

From the results presented above we can conclude that the amorphous pocket creation process cannot be qualitatively modeled by the heat transport equation and melting criterion that includes local melting of atoms. It requires the inclusion of some

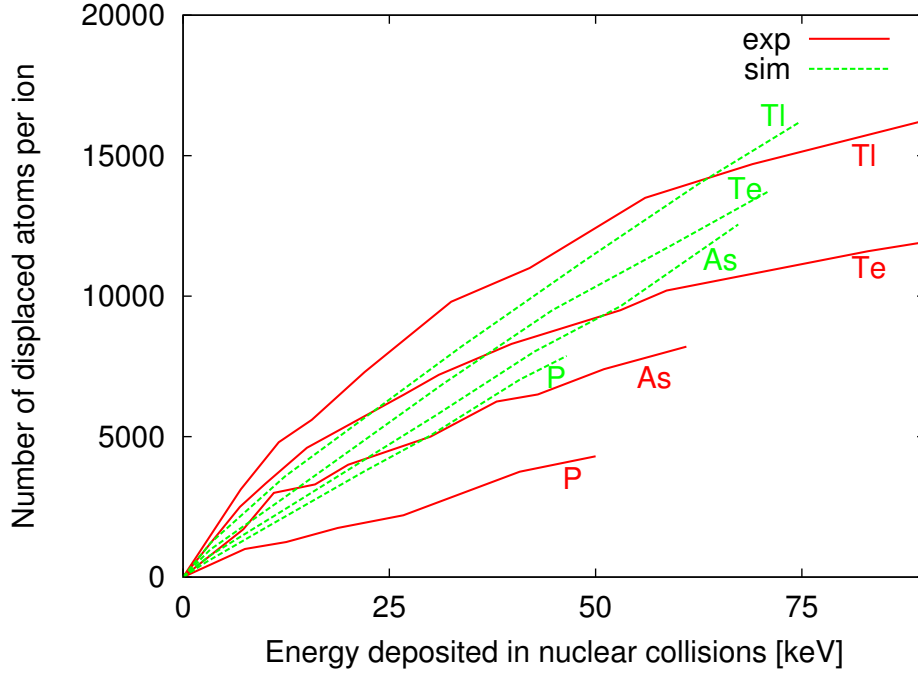


Figure 3.26: Number of displaced atoms per incident ion versus energy. Experimental results - solid lines [6]. Simulation results: dashed lines - criterion requires that at least 3 neighbors meets the melting criterion before one atom is considered molten.

larger zones when considering the melting process, and that was modeled by the geometrical criterion described in Section 3.4.2.6.

In Figs. 3.27 and 3.28 the qualitative influence of the heat transport simulation and the applied geometrical criterion is illustrated. In Figs. 3.27 the initial distribution of energetic ions for P and Tl 90keV implantations is presented. This distribution is used as input for the following heat transport simulations. After the heat quenching simulations using melting criterion which includes all 4 neighbors the distribution of molten atoms presented in upper part of Fig. 3.28 is obtained. Although the initial concentration of energetic atoms is relatively high for the whole implantation trajectory, especially for Tl implant (See Fig. 3.27), heat simulations with the applied melting criterion allow creation of molten zones mainly at the end part of the ion trajectory. But noncompact and rather isolated small regions of molten atoms can still be seen. Applying the criterion of minimum 10% of molten atoms we obtain the distribution

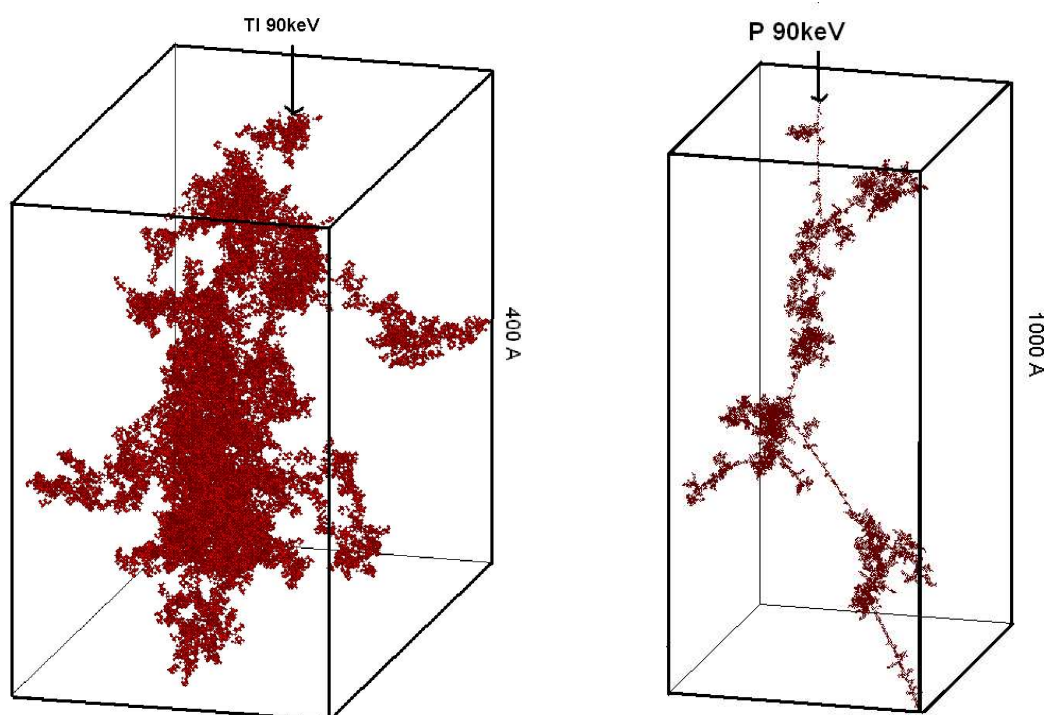


Figure 3.27: Energy distribution of P and Tl 90 keV implants obtained from BC simulations and used as input for heat transport simulations. The arrows indicates the ion's entrance point, while the maximum range of obtained energetic atoms is 400 Å and 1000 Å, respectively.

of the amorphous atoms presented at the bottom of Fig. 3.28. Vanishing of smaller and noncompact zones is evident, while the larger zones become more compact and connected.

3.5.2 Polyatomic effect

In order to test whether the amorphous pockets are really responsible for the additional damage we have compared the results of our model with the experimental data

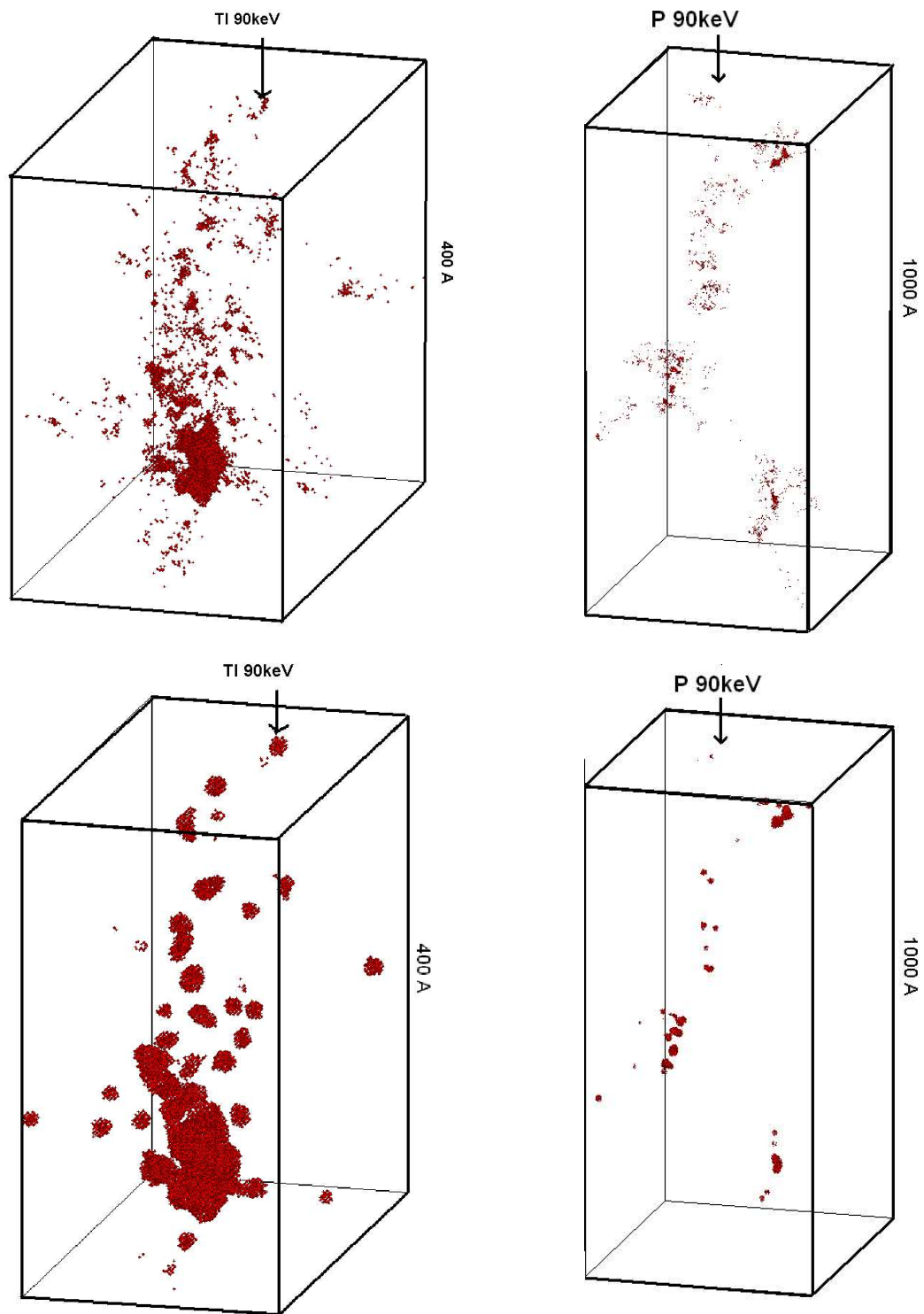


Figure 3.28: Influence of the applied criterion which requires 10% of molten atoms within the sphere of 8\AA radius for P and Tl 90 keV implants. Upper figures: The results of the heat transport simulations. Bottom: After applied geometrical criterion the vanishing of the smaller noncompact defects and on the other side growing and compactness of larger zones can be seen. The arrow points to the place of the ion impact.

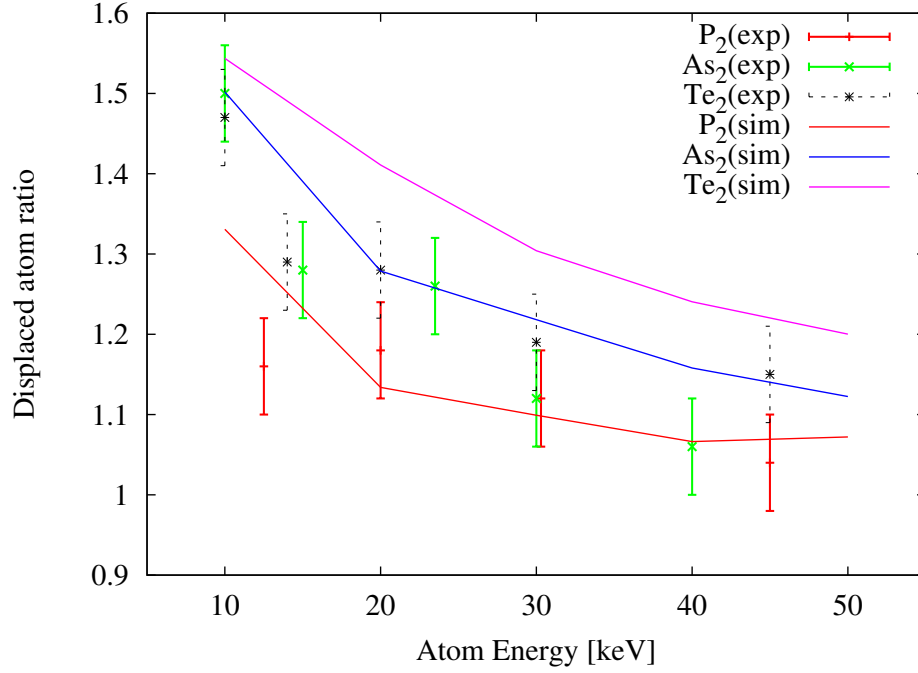


Figure 3.29: Ratio of the number of displaced atoms after P_2 , As_2 and Te_2 molecular implantation and the corresponding number after atomic ion implantations with the same atom dose and atom energy, as a function of atom energy. Lines: Proposed amorphous pocket model. Symbols: in-situ RBS data obtained at cryogenic temperature [6]. The error bars represent standard deviation of the data obtained by large number of simulations.

published on the polyatomic effect [6] and presented in Fig. 3.4 for three different ion species. Fig. 3.29 shows the ratio of the number of displaced atoms after P_2 , As_2 and Te_2 implantations and the corresponding number after implantation of atomic ions with the same atom energy and atom dose. The same applied criteria are used as in the previous section.

It can be seen that both the ion mass and the energy dependence of the polyatomic effect are qualitatively described by the model. However the magnitude of the ratio is within the experimental results for P and As implants, but the overestimation of the ratio is obvious for the Te implants. The reason for this can be uncertainty of the actual contribution to the RBS/C spectra of the recoils and amorphous pockets as

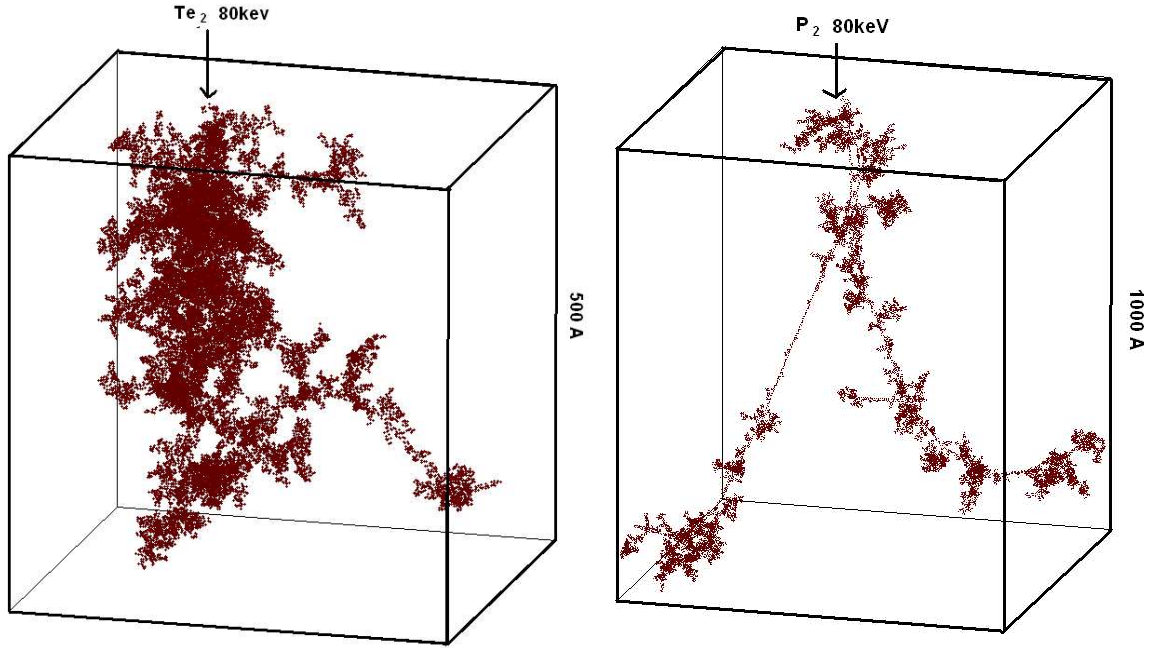


Figure 3.30: Energy distribution upon P and Tl 80 keV diatomic implants obtained by BC simulations and used as input for the heat transport simulations. The arrows indicates the ion's entrance point, while the maximum range of obtained energetic atoms is 500 Å and 1000 Å, respectively.

discussed in the previous section.

Qualitative influence of the particular melting criteria in different evolution stages of molten atom simulations is presented in Figs. 3.30 and 3.31. In Figs. 3.30 the initial distribution of energetic ions after P_2 and Tl_2 80keV implantations is presented. It confirms the assumption of overlapping of the collision cascade of atomic ions for heavy ions (Tl implant) which leads to the creation of amorphous zones in the initial as well as in the end part of the collision cascade. P atomic implants create dilute subcascades where little overlap occurs leading to the creation of very small isolated pockets. Introduction of geometrical criterion, as in the case of atomic implants, removes small isolated molten zones, favoring larger compact pockets.

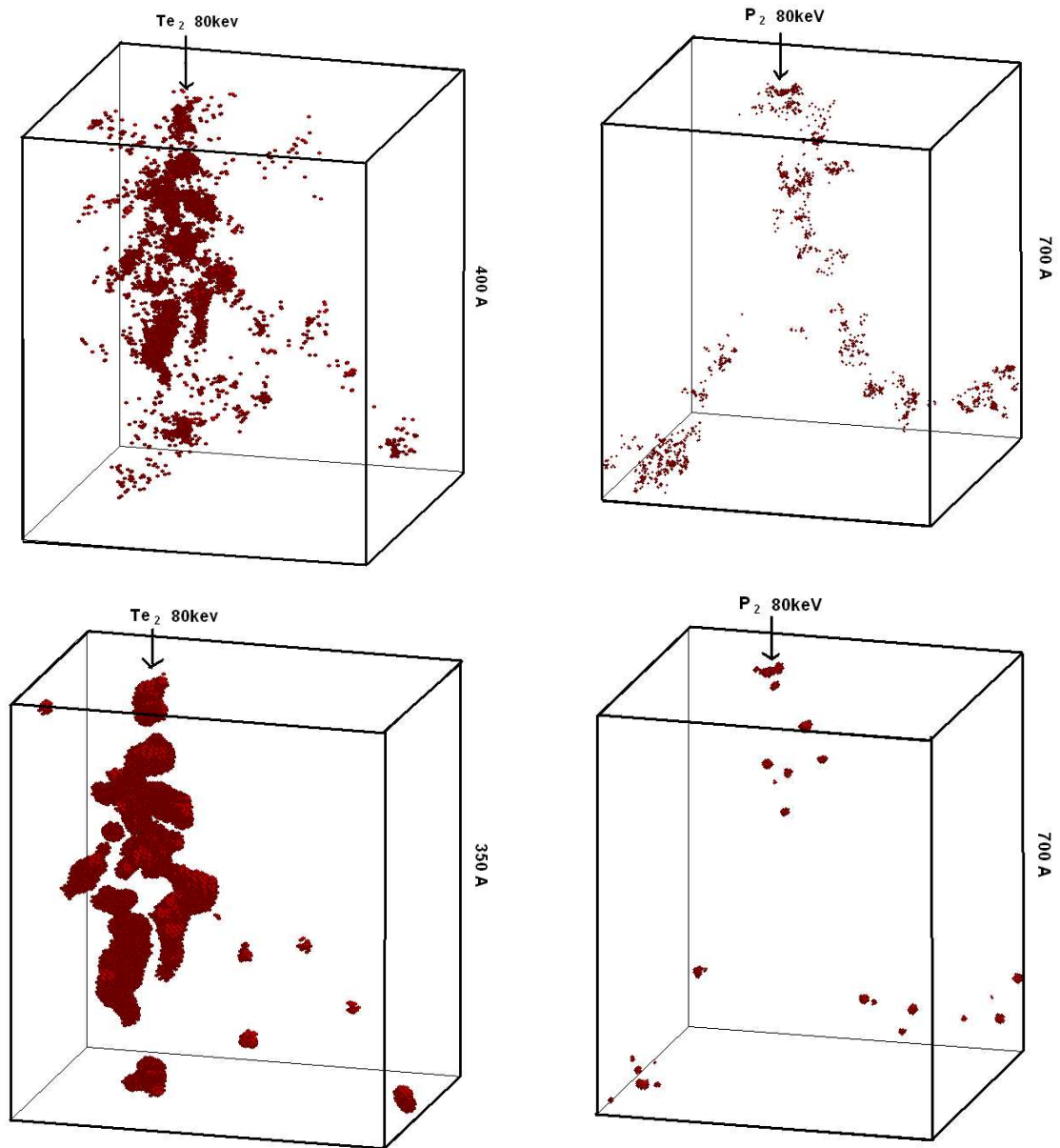


Figure 3.31: Influence of the applied criterion which requires 10% of molten atoms within the sphere of 8\AA radius for P2 and Te2 80 keV diatomic implants. Upper figures: The results of the heat flow simulations. Bottom: After applied geometrical criterion the vanishing of the smaller noncompact defects and on the other side growing and compactness of larger zones can clearly be seen. The arrow points to the place of ion impact.

3.6 Conclusions

The presented model takes into account the following physical concepts of the amorphous pockets creation process:

- Heat transport simulation of deposited energy.
- Heat of melting when an atom melts
- Energy stored in the lattice after an atom melts
- Melting criterion that takes into account that the melting should be the result of the overlap of neighboring heat sources and not due to a single energy event
- Local lattice collapse once the defect density exceeds a threshold

Although the inclusion of the heat of melting and the heat stored into crystal quantitatively improved the ability of the heat flow model to predict the number of displaced atoms upon heavy ion implants it is clear that this was not sufficient to explain the ion mass effect. Introducing a critical defect density above which a local region collapse to the amorphous state significantly improved the results. Thus, taking into account neighboring environment of an atom allows better accounting of the damage morphology, qualitatively gaining the correct ion mass and energy dependence. We can conclude that considering the lattice collapse when the density of molten atoms exceeds a critical value is essential for the qualitative modeling of the amorphous pockets process. The used value of 10% is in the range of the reported values for the CPDD in silicon [7].

With the proposed model very good agreement for the number of displaced atoms after implantation of various ion species (P, As, Te, Tl) including molecular ions (P_2 , As_2 , Te_2) and for a wide range of energies is obtained. The presented data are obtained using the same set of the fitting parameters for both the ion mass and polyatomic effect which extends the transferability of the model. Nevertheless, the deviation of the simulation from the experimental data still exists, especially in the high energy range for the monoatomic implantations, and for Tl in the case of molecular implants. The

eventual uncertainty of the type of the defects present in the sample and uncertainty of the influence of particular defects to the final number of displaced atoms could be reasons for the discrepancies between the experimental and simulated data. Further modeling of the influence of the amorphous pockets and eventual strain around them should be performed in order to justify or disconfirm the factor of “+1” used to model the amorphous atoms contained in the pockets. Although the influence of recrystallization process at cryogenic temperatures is negligible some recrystallization due to local heating from neighboring cascades may occur [2] what can influence the obtained data.

Chapter 4

Rutherford Backscattering Spectroscopy

4.1 Introduction

The Rutherford Backscattering Spectroscopy technique with channeled ions (RBS/C) has been used extensively over the last few decades for the purpose of quantitative analysis and accurate determination of stoichiometry, thickness and depth profiles of impurity and damage distributions in thin surface layers [33, 137–142]. The basic principle of the RBS/C technique is illustrated in Fig. 4.1. Aligning the ion beam along a major crystallographic axis allows to obtain information about the crystalline quality of the sample. Due to inelastic collisions channeled ions lose their energy. Atoms displaced from crystallographic positions, like impurities or defect atoms, further affect channeling by direct backscattering of channeled atoms resulting in a higher backscattering yield. Measuring the number and energy spectra of backscattered ions in the near-surface region allows identification of the atomic masses and quantification of target elements as a function of depth [137, 139, 143, 144].

Application of the RBS/C method to damage quantification is illustrated in Fig. 4.2. Comparing the RBS spectra of samples implanted with different fluence (samples A and B in Fig. 4.2), with spectra obtained from the perfect crystal ('virgin') and amorphous material a qualitative estimation about the amount of damage can be obtained. The simple inspection of the measured energy spectra in Fig. 4.2 gives us the information about the amount of disorder in different samples and the answer whether the irradi-

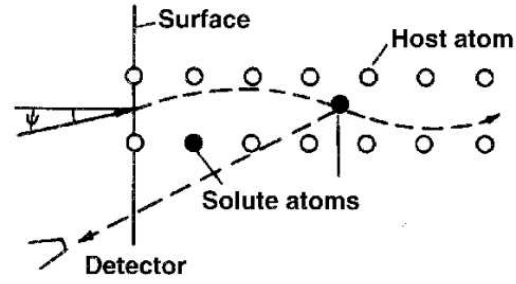


Figure 4.1: Schematic view of the channeling of ions directed at an angle ψ to a close-packed row of atoms in a crystal. Channeled ions are backscattered from solute atoms.

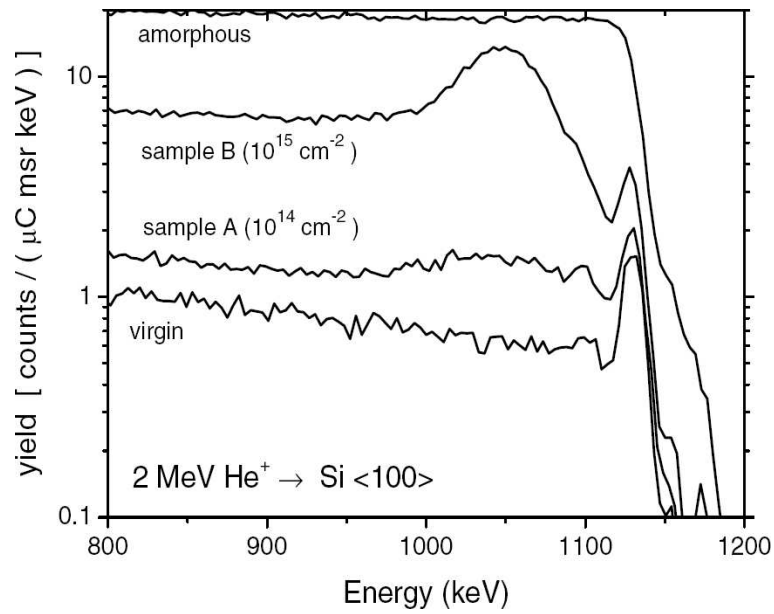


Figure 4.2: Example of the damage measurement with RBS technique: 2 MeV He $\langle 100 \rangle$ RBS/C experimental energy spectra for the samples implanted with 180 keV Si^+ ions at a fluence of 10^{14} cm^{-2} (sample A) and 10^{15} cm^{-2} (sample B). The spectra of a virgin and an amorphous Si sample are shown for comparison[54].

ated sample has been amorphized or a thermal process has restored the perfection of virgin Si.

A better insight into the amount of damage in the implanted sample can be obtained in the defect analysis based on the so-called two-beam approximation (TBA) introduced by Bogh [59]. It is important to remark that experimental RBS spectra are usually obtained as a function of energy and before the quantification procedure they must be converted to the corresponding depth spectra, which is given as a function of the collision depth. The data are usually analyzed according to the so called Aarhus convention, in which it is assumed that the random stopping power applies to both the ingoing and outgoing trajectories. With this assumption, the depth of scattering is uniquely determined and the conversion of the energy to the depth RBS/C spectra can be obtained [137]. In the framework of the two-beam approximation, for the case of low damage samples we can estimate the defect concentration in a sample from the measured spectrum as [139, 145]

$$n_d(z) = N \cdot \frac{\chi_D(z) - \chi_V(z)}{1 - \chi_V(z)} \frac{1}{f} \quad (4.1)$$

where $n_d(z)$ is the concentration of the displaced atoms at depth z , N is the atomic density of the crystal, f is the defect scattering factor (f goes from $f = 1$ for randomly displaced atoms down to $f \approx 0$ for dislocations [141]). The normalized RBS/C yield $\chi_D(z)$ at the depth z represents the measured value of the RBS signal at this depth divided with the corresponding value of RBS/C signal of the amorphous sample. χ_V is the normalized virgin yield defined similarly. The two beam approximation with a sufficient accuracy can only be applied in the cases when only one well-defined defect type is present in the analyzed crystal, so that the scattering factor is known [141]. In most cases real crystals contain unknown mixtures of a variety of different defect types for which the scattering factor f is unknown.

For a more detailed analysis, such as the evaluation of the number of defects introduced by ion irradiation, RBS/C is most accurately used in combination with Monte Carlo binary collision simulations. Since the RBS/C signal is sensitive to the exact positions of the impurity atoms in the crystal lattice [48, 50, 52, 77], it is important to make reasonable assumptions about the kind of defects and also to know the atomic positions of each defect type. Standard models based on the picture that damage

consists of displaced atoms surrounded by the ideal lattice neglect the relaxation of the lattice around the defects and lead to the overestimation of the damage produced by ion implantation [48, 121]. In addition, because of the assumption that the atoms are randomly displaced within the lattice these models often failed to describe multi-axial RBS/C measurements of implanted Si [48, 49]. A deeper physical insight on the actual location, structure and binding properties of defects to the host lattice is indeed necessary to improve our current understanding of ion channeling experiments. Atomic-scale models [60–72] have significantly improved the understanding of structure and properties of small native defects in silicon. Such calculations yield the atomic positions at strictly defined positions, corresponding to energy minima, rather than at random positions. In addition, these defects cause lattice relaxation, which interacts with the analyzing beam, increasing dechanneling and the RBS/C signal. Recent interpretation [48, 50–54] of RBS/C measurements with atomic defect models, structurally relaxed with empirical potentials, gave an improved interpretation of multi-axial RBS/C analysis of Si containing low levels of disorder. The influence of the correct atom positions on the interpretation of channeling implantations is also shown by Hobler et al. [47].

Using the Tersoff potential as the empirical potential and the VASP code for ab-initio calculations we have determined the coordinates of the split- $\langle 110 \rangle$ interstitial, of the di-, tri-, and four-interstitial cluster, and of the tetrahedral interstitial as well as the strain on neighboring atoms induced by the presence of these defects. We have proposed an atomistic model of damage where the location of the defect atoms in the host lattice are determined by these atomic-scale models calculated previously. Using these coordinates in binary collision RBS/C simulations we find differences in the RBS/C yields of up to 30%. The dependence of the backscattering yield on the assumed defect type is larger with the defect coordinates obtained by the empirical potential than by the ab-initio calculations. The influence of the strain is investigated as well as the anisotropic behavior of the small defects in multi-axial beam alignments. In order to investigate the mutual interaction of the defects and limitation of this model, the cell populated with various damage concentrations is relaxed with the Tersoff III empirical potential. After the relaxation the cell is inspected with RBS/C simulations and the differences between the relaxed and nonrelaxed system are investigated. The conclusion is that the nonrelaxed model can be used up to concentration of 6-7% of the atomic density depending on the assumed defect type. By increasing the damage concentration mutual defect interactions lead to the amorphization of the sample.

Within the framework of this thesis a Rutherford Backscattering Spectroscopy quantification code has been written as a module of the Monte Carlo binary collision simulation code ‘IMSIL’ [77]. The code uses the principles of the close encounter probability [146] and the Rutherford scattering cross section. Computational details of binary collision simulation of RBS are outlined in Section 4.2. In the next section we propose an atomistic model of damage used in RBS/C simulations. Within the proposed model the influence on interpretation of RBS/C spectra of a various atomic-scale models as well as the calculation method are investigated and the results are presented in Section 4.4. In Section 4.5 we show the RBS/C simulation results performed on the relaxed supercell populated with different damage concentration. Finally in the last section we give conclusions of our work.

4.2 Binary collision simulation of RBS

In this section we outline the principles of the implemented RBS/C simulation code. The code is written as a module of the Monte Carlo binary collision code IMSIL [8, 77]. The code uses the principle of the close encounter probability defined by Barret [146] and the Rutherford backscattering cross section [139]. The program gives as the output the RBS signal as a function of backscattering energy.

Fig. 4.3 presents a schematic view of a backscattering event that leads to the scattering of the incoming particle to the detector. The analyzing ions are directed into the surface of the wafer. The z -axis defines the wafer surface normal vector. Let us assume that a particle with mass m_1 and initial energy E experiences a collision at depth z^* with a target particle of mass m_2 which is initially at rest. After the collision the backscattered ion (particle 1) leaves the target towards the detector placed at angle θ_{OUT} with respect to the negative z -axis. The scattering angle that leads to the detection of the scattered particle into the detector is ψ . The angle between the incoming ion and the z -axis is α .

The sequence of a Rutherford backscattering event of the type modeled in this work can be divided into the following steps:

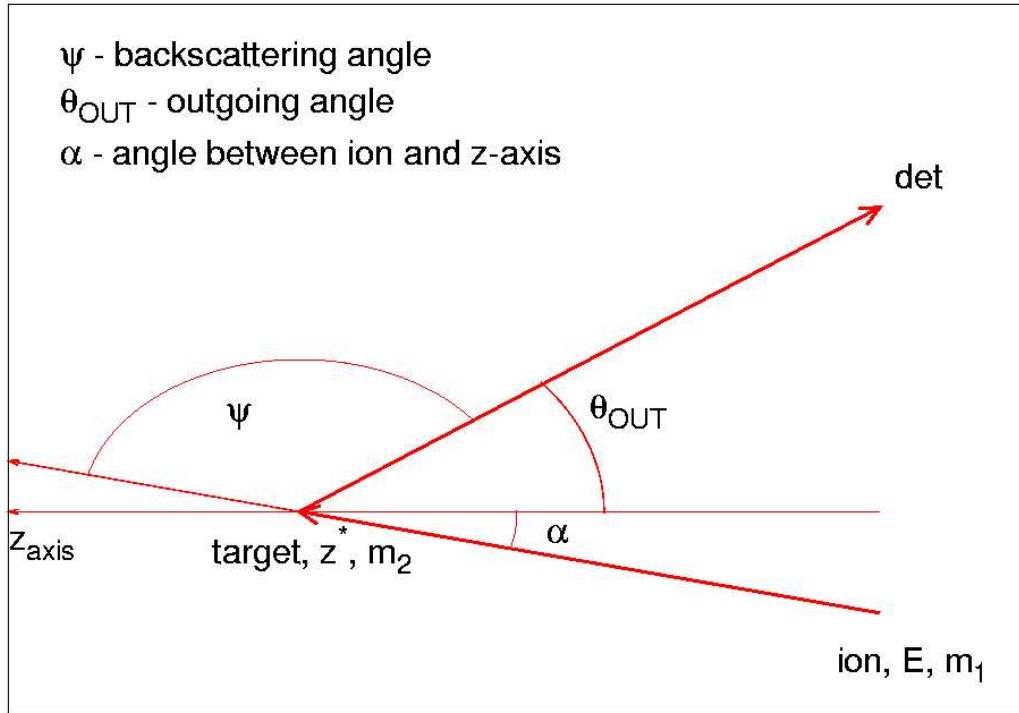


Figure 4.3: Illustration of a Rutherford backscattering event defining the important quantities. z^* is the depth where the scattering event takes place. m_1, m_2 denote the ion and the target mass, respectively. θ_{OUT} is the angle between the z-axis and the detector. ψ is the backscattering angle that leads to scattering into the detector and α is the angle between the ion direction and the z-axis.

1. The trajectory and energy loss of the incoming ion before the scattering event.
2. The probability of a large angle backscattering event that leads to the scattering of the particle towards the detector (Rutherford scattering event).
3. Energy loss due to the Rutherford scattering event.
4. The trajectory of the scattered ion in the outgoing path towards the detector is approximated by a straight line in a random medium, and the energy loss is taken into account.

5. A count, representing a quantitative measurement of the RBS event, is added to the appropriate energy bin.

The detailed description of the modeling of these events is given in the following sections.

It is important to emphasize the difference between the “probabilistic” treatment of a Rutherford scattering event, based on the concept that will be described here, from the treatment done in the BC approach. When an ion enters into the crystal it undergoes a collision. The actual scattering angle and the energy loss as well as the direction of the ion after the mentioned scattering will be calculated in the BC part of the program. However, this scattering event does not in general lead to the scattering of the particle into the detector (Rutherford scattering), and, actually, the probability that an ion is scattered into the detector by any scattering event, is rather low. Therefore, in a pure BC simulation a huge number of ions would have to be simulated to obtain reasonable statistics for the RBS signal. To resolve this problem, we calculate in parallel at each collision the probability that the ion would be scattered, with appropriate (usually large) angle, to the detector. After this scattering event the ion can eventually continue its movement experiencing many further collisions as calculated in the BC treatment. In other words in the BC approach single ion trajectory is followed and calculated while in the RBS approach for each collision we have a possible trajectory that can lead to the detection of the ion in the detector. Summing up over all these probabilities for many ions throughout their whole trajectories we obtain the quantitative estimation of the number of ions “virtually” scattered into the detector.

4.2.1 Trajectory of incoming particle

The ion entering into the crystal loses its energy due to a series of successive collisions with the target atoms. The corresponding trajectory and the energy of the particle before the scattering event E will be calculated in the binary collision program “IMSIL” [8] and will not be described here. When a collision occurs the position and the energy of the incoming particle as well as the position of the target atom will be transferred to the RBS module.

4.2.2 Rutherford scattering event

The incoming ion (particle 1) experiences collision at depth z^* with the target atom (particle 2) and leaves the target towards the detector placed at angle θ_{OUT} defined with respect to the negative z-axis (see Fig. 4.3).

The probability that the ion will undergo the collision with the target atom and be detected in the detector is given by the RBS reaction probability P_{RBS} which is given as a product of the Rutherford backscattering differential cross section, the close nuclear encounter probability and the detector solid angle [147–149]:

$$P_{RBS} = P_{vib} \cdot \frac{\partial\sigma}{\partial\Omega} \cdot d\Omega \quad (4.2)$$

$\partial\sigma/\partial\Omega$ is the Rutherford scattering cross section given with equation 4.3 and P_{vib} is close nuclear encounter probability defined as the probability density that the target atom is at the point of passage when the thermal vibrations are taken into account. $d\Omega$ [sr] is the detector solid angle.

First we outline and explain briefly the Rutherford backscattering cross section followed with the definition of the calculation of the probability density due to thermal vibrations.

4.2.2.1 Rutherford backscattering cross section

Fig. 4.4 [138, 144] illustrates the concept of a cross section. We prepare an incident flux of beam particles of known energy, and measure the number of particles scattered out of the beam at particular scattering angle ψ . At an angle ψ from the direction of incidence, let an ideal detector count each particle scattered in the differential solid angle $d\Omega$. We assume that the flux will always be uniform over the thickness of the target material. The azimuthal symmetry is also assumed, and the detector will capture only the portion of the scattered particles defined by the detector solid angle. The differential scattering cross section is defined as the number of interactions per target particle that lead to scattering into an element of the solid angle ($d\Omega$) at a given angle

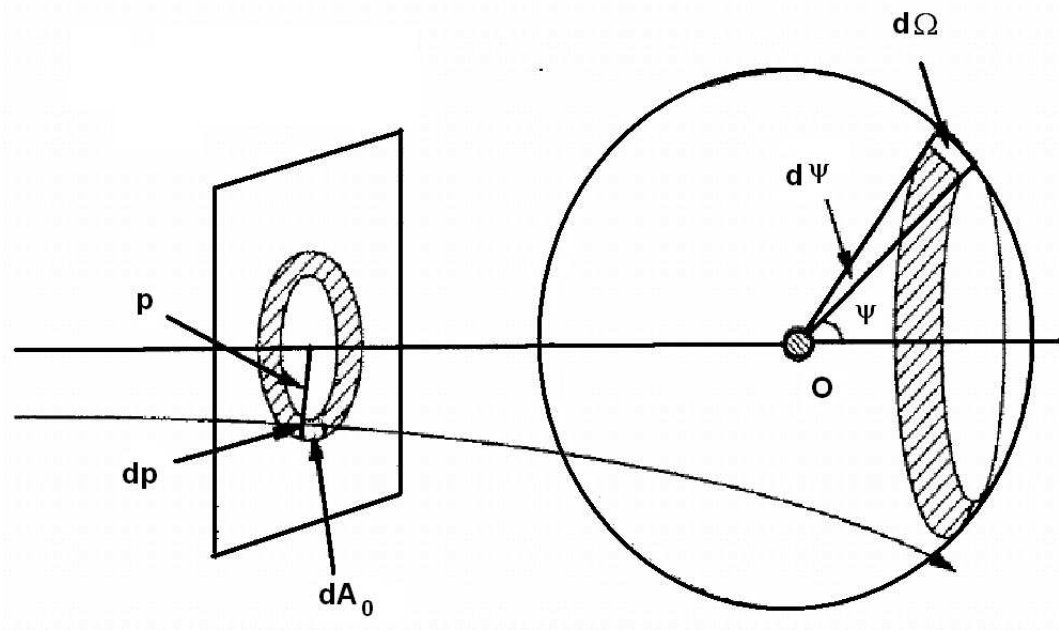


Figure 4.4: Illustration of the quantities related to the definition of the scattering cross section. Incident particles within the area dA_0 are emitted into the area $d\Omega$. p is the impact parameter and ψ is the scattering angle. O is the scattering center.

(ψ) divided by the number of incident particles per unit area [144, 150]. Applying the definition of the cross section to a particular event, instead to a beam of particles, we assume that the probability of a collision between the incoming ion and the target atom is proportional to the differential cross section [138, 144, 150] which reads[138, 139]:

$$\frac{\partial \sigma}{\partial \Omega} = \left[\frac{z_1 \cdot z_2 \cdot q^2}{8\pi\epsilon_0 \cdot E} \right]^2 \cdot \frac{1}{\sin^4 \psi} \cdot \frac{\left[\sqrt{1 - \left(\frac{m_1 \cdot \sin \psi}{m_2} \right)^2} + \cos \psi \right]^2}{\sqrt{1 - \left(\frac{m_1 \cdot \sin \psi}{m_2} \right)^2}} \quad (4.3)$$

Where m_1, z_1 are the mass and the atomic number of the incoming ion, respectively. m_2, z_2 are the mass and atomic number of the target particle, respectively. $q = 1.609 \times 10^{-19}C$ is the elementary charge and $\epsilon_0 = 8.85434 \times 10^{-12}F/m$ is the vacuum permittivity. ψ is the scattering angle through which the incident ion is scattered

and E is the energy of the incident particle immediately before the scattering event.

Eq. 4.3 is valid as long as the distance of the closest approach between the incoming ion and the target atom is large compared with nuclear dimensions, but small compared with the Bohr radius $a_0 = 4\pi\epsilon_0\hbar^2/(m_e q^2) = 0.53\text{\AA}$, where q is the elementary charge, $m_e = 9.109 \times 10^{-31} \text{ kg}$ is the mass of the electron, and $\hbar = 1.054 \times 10^{-34} \text{ Js}$ is the reduced Planck's constant [138]. In this case the interaction between the incoming and target atom is very well described by the Coulomb repulsion of two nuclei. For $\psi \Rightarrow 0$ Eq. 4.3 says that the cross section tends to infinity, which violates the initial assumption that the cross section of the target nuclei should be small. Small scattering angles correspond to large impact parameters between the projectile and the target nuclei, which are greater than the radius of the innermost electron shell of the target atom.

The backscattering angle is calculated as (See Fig. 4.3):

$$\psi = \arccos(\vec{e}_{ion} \cdot \vec{e}_{det}) \quad (4.4)$$

where \vec{e}_{ion} is the unit vector in the direction of the ion before the collision, and \vec{e}_{det} is the unit vector in the direction of the detector.

Experimental measurements have shown that actual cross sections deviate from Rutherford at both high and low energies for all projectile-target pairs [139, 152–154]. The low energy departures are caused by partial screening of the nuclear charges by the electron shells surrounding both nuclei. The low energy correction to Rutherford cross section given by L'Ecuyer [152] is:

$$\sigma_{corr}/\sigma = 1 - \frac{0.049z_1z_2^{4/3}}{E_{CM}} \quad (4.5)$$

Where E_{CM} is the CM energy of the system related to the ion energy (measured in lab frame) as

$$E_{CM} = \frac{E}{(1 + \frac{m_1}{m_2})} \quad (4.6)$$

This correction by L'Ecuyer 4.5 is a first order correction and does not take into account the influence of the scattering angle. Its applicability is mainly limited for

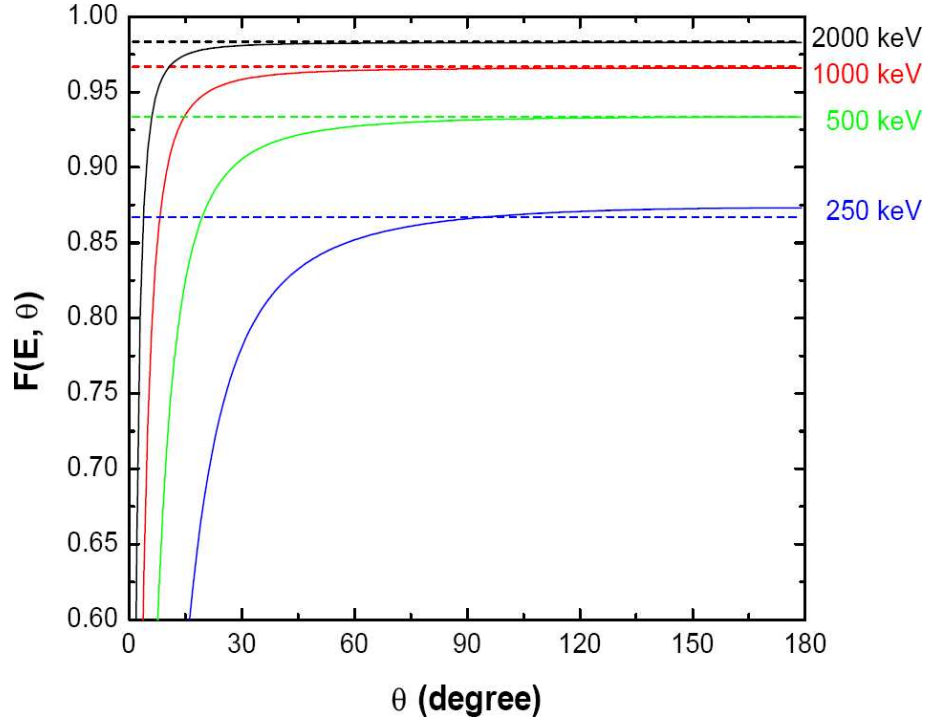


Figure 4.5: Angular dependence of the correction factors for the Rutherford cross-section by L'Ecuyer (dashed lines) and Andersen (solid lines) for He backscattered from gold at different energies [151].

backscattering angles $\psi > 90^\circ$. A more accurate correction is given by the angular and energy dependent factor by Andersen [153]

$$\sigma_{corr}/\sigma = \frac{(1 + \frac{V_1}{2E_{CM}})^2}{\left\{ 1 + \frac{V_1}{2E_{CM}} + \left[\frac{V_1}{2E_{CM} \sin(\theta_{CM}/2)} \right]^2 \right\}^2} \quad (4.7)$$

where θ_{CM} is the CM scattering angle and V_1 is given by:

$$V_1[kV] = 0.04873 z_1 z_2 \left(z_1^{2/3} + z_2^{2/3} \right)^{1/2} \quad (4.8)$$

The dependence of the correction factors as a function of scattering angle is presented in Fig. 4.5 [151] for He scattered from gold. For large scattering angles both

correction factors are near to one and similar, while for small scattering angles only the Anderson's factor gives adequate correction to the Rutherford cross section.

For sufficiently high energies the distance of the closest approach between the projectile and the target nuclei reduces to the dimension of the nuclear sizes. The short range nuclear forces then begin to influence the scattering process, and the deviations of the cross section from Rutherford appear [139,144]. When the scattering process is inelastic, the energy of the scattered particle cannot be expressed by the kinematic factor [144]. A formula for the energy E_{NR} above which the deviations of cross section are larger than $> 4\%$ is given by Bozoian [155]

$$E_{NR}[MeV] = \frac{m_1 + m_2}{m_2} \frac{z_2}{10} \quad \text{for } z_1 = 1 \quad (4.9)$$

$$E_{NR}[MeV] = \frac{m_1 + m_2}{m_2} \frac{z_1 z_2}{8} \quad \text{for } z_1 > 1 \quad (4.10)$$

From Eq. 4.10, it can be concluded that special care must be taken when using protons because nuclear reactions become significant for proton interactions with light elements at energies greater than 1 MeV. For the case of He in Si the cross section can be considered purely Rutherford with negligible deviations for ion energies up to 4 MeV. Low energy corrections become of practical importance only for low and middle energy scattering analysis $E < 100 \text{ keV}$. For many channeling studies, the accurate knowledge of the scattering cross sections is not necessary, since only normalized yields rather than absolute yields are used.

4.2.2.2 Thermal vibrations

The close nuclear encounter probability is defined as the probability of finding a particle at the point of ion passage due to thermal vibrations. Atoms are assumed to vibrate independently where the probability density of a displacement has the Gaussian distribution [137]:

$$P_{vib}(r) = \frac{1}{2 \cdot \pi \cdot x_{rms}^2} \cdot \exp\left(-\frac{r^2}{2 \cdot x_{rms}^2}\right) \quad (4.11)$$

r is the distance between the collision point and the target atom. x_{rms} denotes the root-mean-square vibration amplitude of the target atom in one direction and can be calculated using the Debye theory of thermal vibrations [137]:

$$x_{\text{rms}} = 12.1 \left(\left[\frac{f(x)}{x} + \frac{1}{4} \right] / (m_2 T_D) \right)^{1/2} \quad (4.12)$$

Where T_D is the Debye temperature, m_2 is the atomic weight of the vibrating atoms and $f(x)$ is the Debye function

$$f(x) = \frac{1}{x} \int_0^x \left[\frac{\epsilon d\epsilon}{\exp(\epsilon) - 1} \right] \quad (4.13)$$

x is given by

$$x = T_D/T \quad (4.14)$$

$T[K]$ is the crystal temperature. At room temperature with the Debye temperature of 490 K for silicon Eq. 4.12 gives a vibration amplitude of 0.0083 Å [137, 156].

4.2.3 Energy loss due to Rutherford scattering

As a result of the backscattering event the particle will lose energy. The ratio of the projectile energy immediately after the collision to the incident energy immediately before the collision is defined as the kinematic factor K [137, 139, 144]

$$K = \frac{\left[\frac{m_1}{m_2} \cos \psi + \sqrt{1 - \left(\frac{m_1}{m_2} \right)^2 \sin^2 \psi} \right]^2}{\left(1 + \frac{m_1}{m_2} \right)^2} \quad (4.15)$$

Thus, the energy of the particle before and after the collision are therefore calculated as

$$E_{after} = E \cdot K \quad (4.16)$$

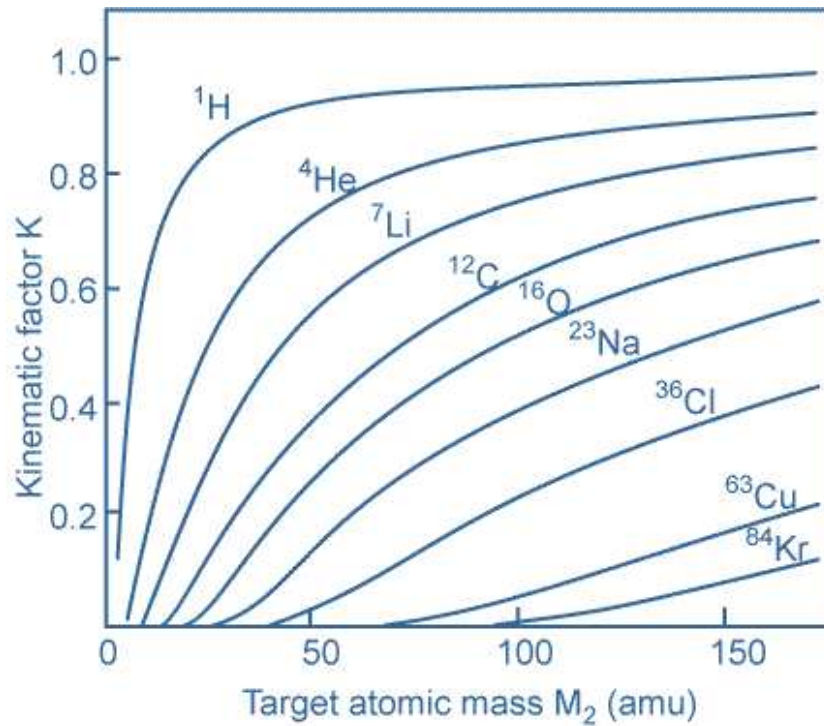


Figure 4.6: Kinematic factor at $\psi = 170^\circ$ as a function of a target mass for a number of projectile types [139].

Fig. 4.6 shows the kinematic factor at $\psi = 170^\circ$ as a function of the target atom mass for a number of projectile types [139].

4.2.4 Outgoing particle path

After the collision we assume that on its path to the detector the particle travels in a straight line through a random medium.

The energy of the particle detected at the detector can be calculated by the following equations:

$$E_{out} = E_{after} + \int_{z^*}^0 \left(\frac{\partial E}{\partial z'} \right) dz' \quad (4.17)$$

$$\frac{\partial E}{\partial z'} = \left(\frac{\partial r}{\partial z} \right) \left(\frac{\partial E}{\partial r} \right) = - \frac{1}{\cos(\theta_{out})} \left(\frac{\partial E}{\partial r} \right) \quad (4.18)$$

$(\partial E / \partial r)$ is the rate of the energy loss of the outgoing particle with respect to the distance r traveled through the substrate. $\frac{\partial r}{\partial z} = -\frac{1}{\cos(\theta_{out})}$ according to Fig. 4.3. Energy loss divided with material density is defined as a stopping power what is a function of particle energy.

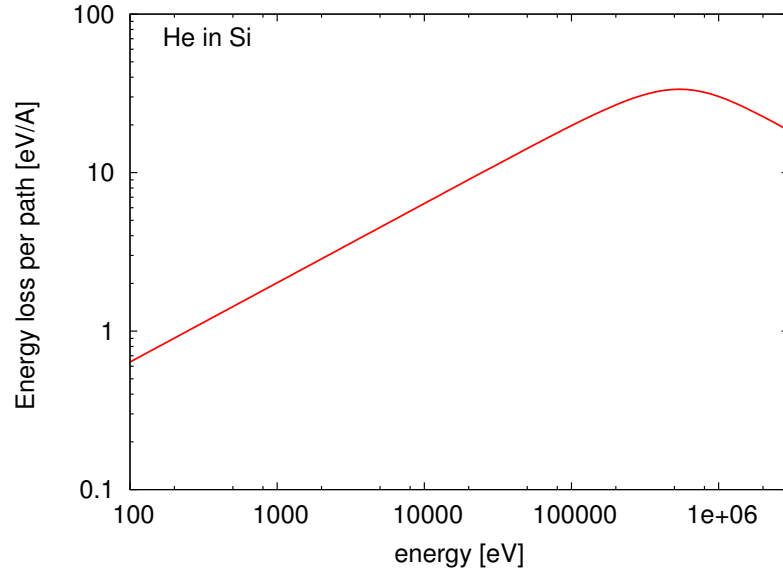


Figure 4.7: The energy loss per particle path for He implantations in Si as a function of energy.

As an example, the energy loss per particle path of He ions traveling through the Si target is illustrated in Fig. 4.7.

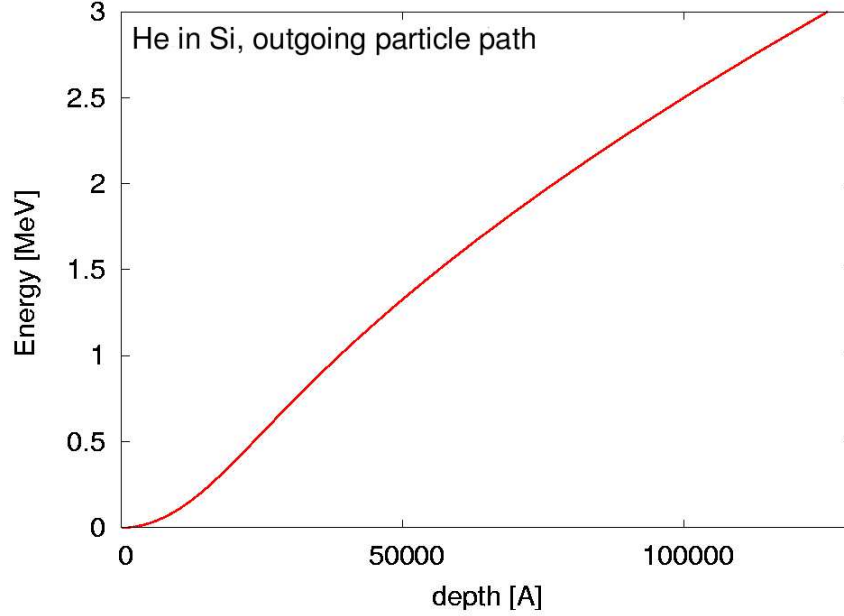


Figure 4.8: *Slowing down of 3 MeV He ions in Si calculated integrating random stopping power values presented in Fig. 4.7. Energy which backscattered particle has to have in order to get out of target after scattering event as a function of a scattering depth. It is assumed that the backscattered particle moves through random medium with straight lines. He 3MeV is used for this example, and scattering angle of 170° .*

After the collision the path of the backscattered particle is approximated by a straight trajectory in a random medium. Random stopping as a function of energy is calculated at the start of the program, using energy equally spaced on a logarithmic scale between the cut off and the ion energy. It is then numerically integrated (Eq. 4.17) using the trapezoidal rule. The result of the integration of the stopping power is shown in Fig. 4.8, for the case of He in Si, with 170° scattering angle. The energy reported at the y-axis is interpreted as the minimal energy that an particle should possess in order to reach given depth in random medium. The remaining energy of the particle leaving the target material is obtained according to Eq. 4.17.

It is important to remark that the approximation of straight random backscattering paths prevents the correct description of plural scattering effects which may occur during this outgoing part of the particle trajectory, and which are expected to be non-negligible at lower ion energies [157, 158]. Plural scattering mainly contributes to the “high” and “low” energy background of the RBS/C signal, measured relative to the surface peak and low energy shoulder [157].

4.2.5 A count in energy spectrum

After leaving the sample the ion travels through the vacuum maintaining its energy and the direction. The backscattering count P_{RBS} is scored in energy spectrum at the outgoing energy E_{out} . If according to Eq. 4.17 particle loses its energy before leaving the target $P_{RBS} = 0$. In addition if the backscattering count P_{RBS} is scored in depth spectrum at the collision depth z^* we can obtain the corresponding RBS/C spectrum as a function of collision depth.

4.3 Atomistic model of damage in RBS/C simulations

The traditional ‘random’ defect model is widely used in RBS/C simulations of the implanted samples. The model is based on the defect positions which are created statistically according to the local damage concentration and the atom positions which are supposed to be randomly distributed interstitials in the perfect lattice. The random model has failed to obtain multiaxial fitting of the RBS/C measurements in implanted silicon [48–52] which raises the requirement for a new improved model of damage in RBS/C simulations. Taking results from the recent investigations in the field of atomic scale modeling of the structure of defects a new improved atomistic model of damage is proposed. In the proposed model the defect positions are also generated statistically according to local damage concentration but the actual atom positions correspond to the already precalculated coordinates of atomic-scale defect models and their strained fields.

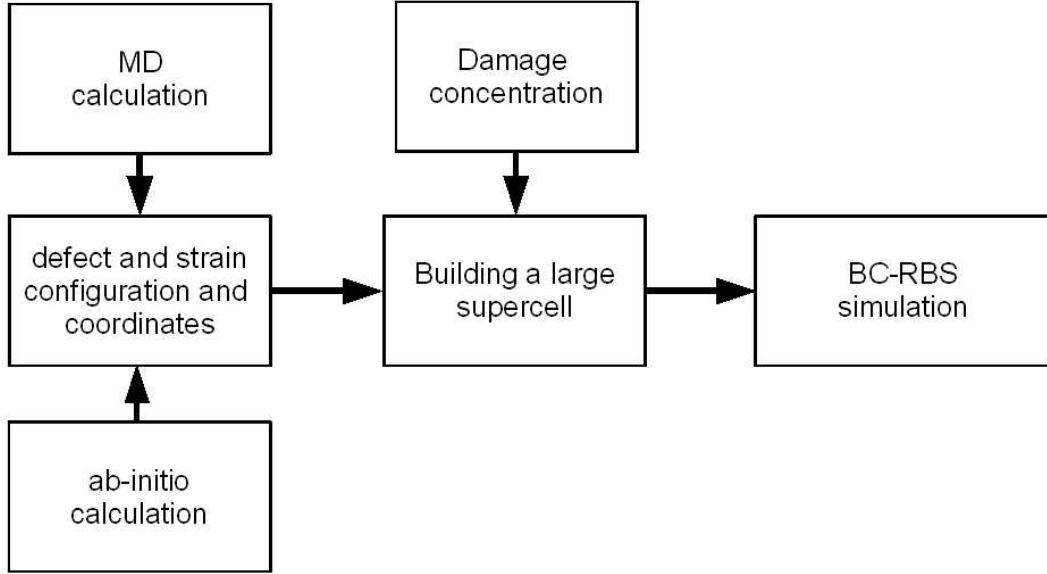


Figure 4.9: *Chart diagram of procedure used to implement atomistic model of damage in Monte Carlo RBS/C RBS/C simulation.*

In order to implement atomistic model of damage in Monte Carlo simulations of RBS/C spectra we have used the procedure presented in Fig. 4.9. In the first step coordinates of various defect types and associated strained fields are calculated using either classical molecular dynamics simulations or ab-initio calculations. These coordinates are used to subsequently populate a large supercell, with one defect type at a time, according to the local damage concentration given by 1D damage histograms. Afterwards RBS/C simulation is performed on the prepared supercell. The details of the particular steps are outlined in the following sections.

4.3.1 Atomic-scale defect models

Using a Si cell with a size of 10x10x10 unit cells relaxed by the Tersoff III [159] empirical potential we have calculated the coordinates of minimum energy configuration of small interstitial clusters I_n , where n denotes the number of excessive atoms

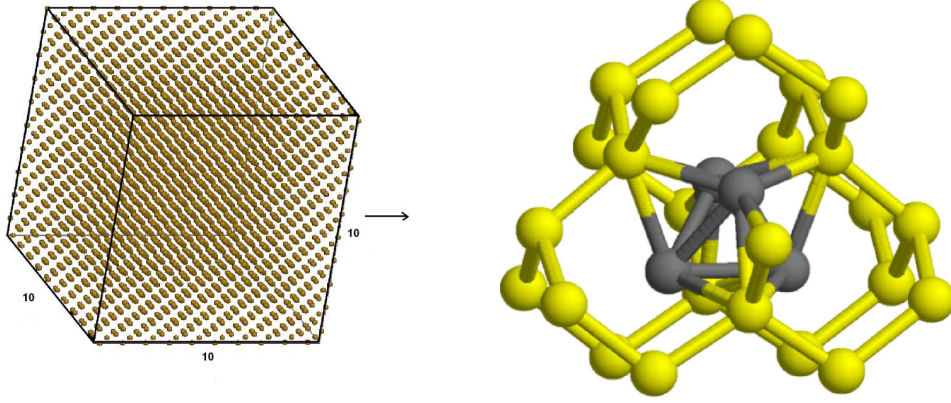


Figure 4.10: *Simulation cell 10x10x10 unit cell used to calculate minimum energy configuration of the defects by Tersoff III empirical potentials. Ball and stick illustration of atomic-scale defect (dark grey) surrounded with cluster of strained atoms.*

in the range $n = 1, \dots, 4$. The relaxation is done by a molecular dynamics simulation of quenching from 300K to 0 K in 5 ps. In order to save the CPU time these defect configurations obtained by MD calculations are used as the initial configurations in ab-initio calculation. A schematic illustration of the MD cell used for the defect calculation and the obtained structure together with the strained region is shown in Fig. 4.10. The coordinates of the defects are introduced into a 216 atoms Si cell and relaxed with the ab-initio code VASP [79]. The calculations were performed using the generalized gradient approximation (GGA) and projector augmented wave potentials. The complete description of the computational details used in ab-initio calculations can be found in Reference [78].

In both cases we have identified the positions of the defect atoms as well as the strain associated with the defects. The following five different configurations of atomic scale models have been considered (see Fig. 4.11): I_1 is the well known split- $\langle 110 \rangle$ interstitial, composed of two defective atoms in the $\langle 110 \rangle$ plane [61, 63, 68–70]. I_2 is the di-interstitial composed of three defective atoms which is obtained adding one single interstitial to an existing I_1 defect [60, 68, 70]. I_3 is the tri-interstitial composed of four defective atoms obtained by adding of one single interstitial to the I_2 structure, which represents tetrahedral case symmetrically embedded into the crystalline envi-

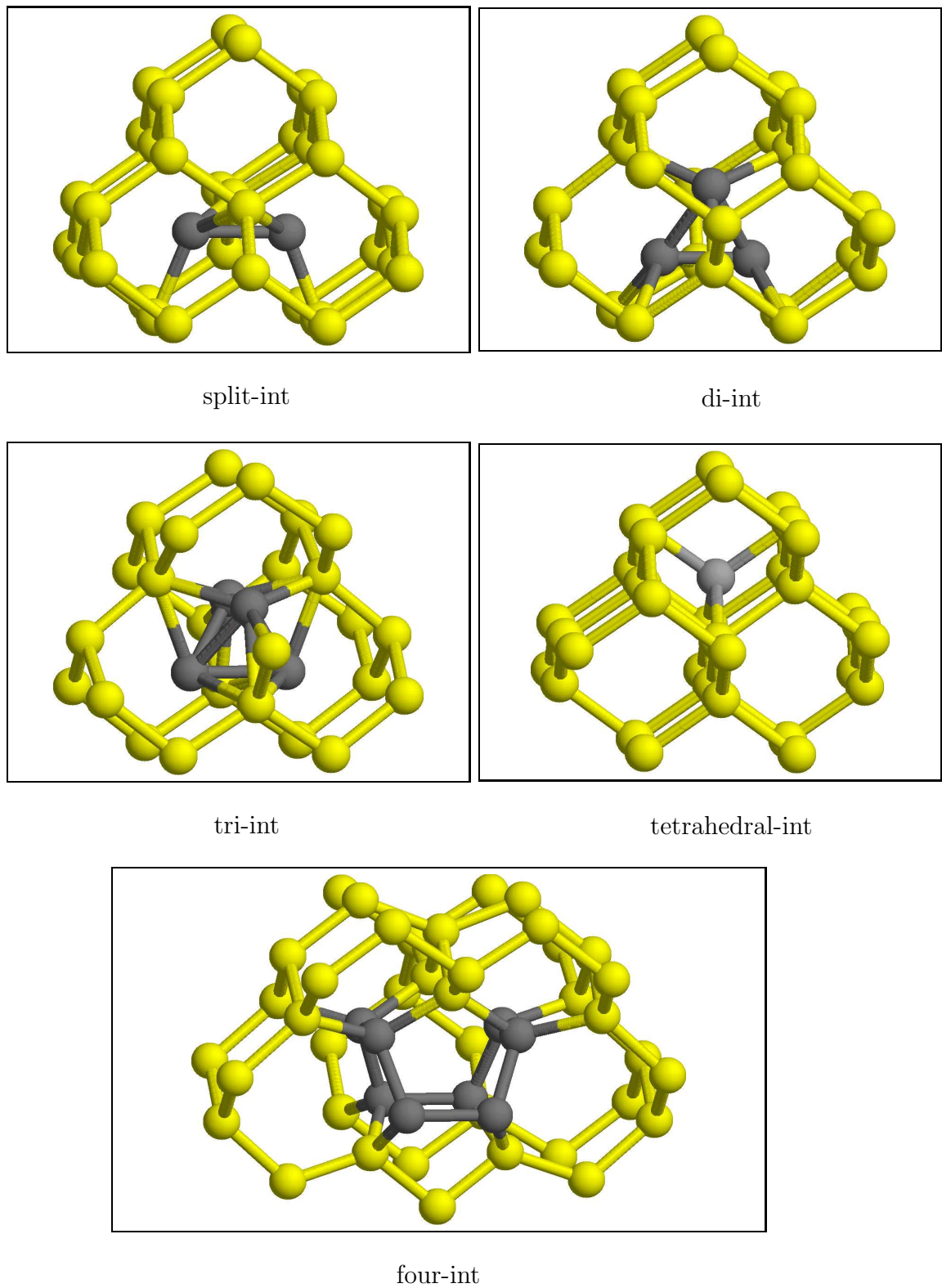


Figure 4.11: *Ball and stick representation of self-interstitial defects calculated with *ab-initio* methods. Si defective atoms are dark grey, where other atoms are light gray.*

ronment [60, 68, 70, 71]. All these configurations are obtained with the $\langle 110 \rangle$ dumbbell defect being fundamental unit. I_4 represents the four-interstitial which is composed of eight fourfold coordinated defective atoms, being formed by the agglomeration of four split- $\langle 100 \rangle$ interstitials on the $\{110\}$ plane [62, 64, 71]. The Si atoms in the I_4 configuration preserve their four-fold coordination. In addition we have considered the tetrahedral interstitial (I_T) [61, 66, 69], which is composed of one fourfold coordinated defective atom while the neighboring crystalline atoms are fivefold coordinated.

4.3.2 Building a large supercell

In the next step a big silicon cell containing 1.6 million atoms ($10 \times 10 \times 2000$ unit cells) is populated with clusters which contain not only the defects but also the strained regions around the defects. The concentration of the defects inserted at particular depth is determined by the damage concentration usually defined in the histogram file. The defects have been inserted as to guarantee a minimum distance between them but otherwise at random positions, taking into account all possible symmetry-equivalent orientations. An equivalent number of vacancies with their strained fields is also inserted into the cell in order to balance the interstitial profile and to keep the number of atoms constant. The strain of nearby defects is superposed linearly.

The term “symmetry-equivalent orientation” is explained in the following. Silicon has a diamond lattice which like other crystals has an ordered internal arrangement of atoms showing symmetry. A crystal’s symmetries can be described in terms of the geometric operations (rotation, reflection, rotoinversion) which applied on the crystal produce identical configurations. The silicon lattice has a set of 24 symmetry operations, which is also reflected on the corresponding defect configurations. Therefore we can apply these symmetry operations on the relative positions (measured from the lattice site) of the defect configuration. The new obtained configurations define a set of symmetry equivalences. Since some defects already possess additional symmetry the effective number of symmetry equivalent orientations will be smaller. In case of the split- $\langle 110 \rangle$ interstitial we have six different symmetry-equivalent orientations, which are presented in Fig. 4.13.

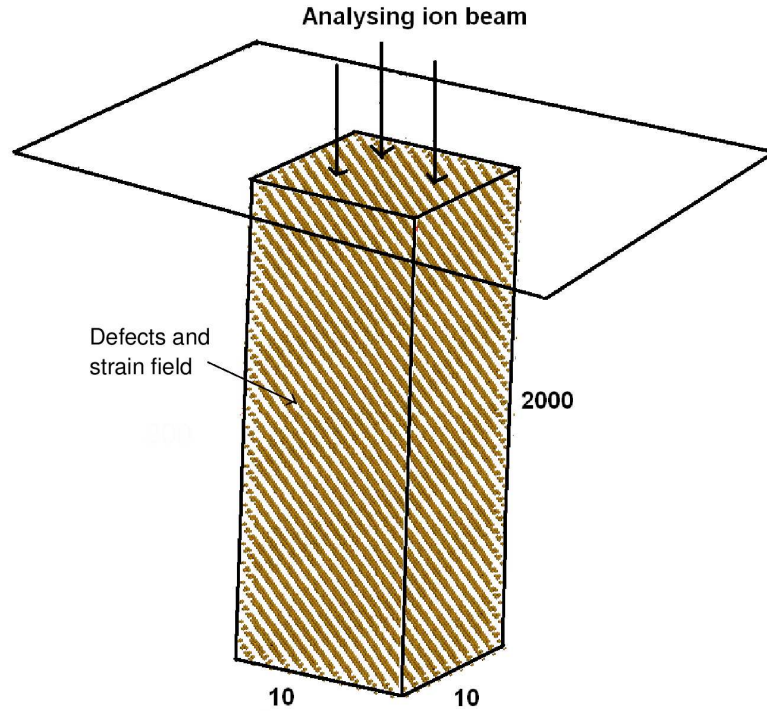


Figure 4.12: Large supercell size $10 \times 10 \times 2000$ unit cells populated with defects and subsequently analyzed with RBS/C He beam to investigate the influence of defect models.

4.4 Investigation of the impact of defect model on Monte Carlo simulation of RBS/C spectra

In order to compare the influence of the particular defect model in silicon on the interpretation of RBS/C spectra we have prepared supercells using the procedure explained in Section 4.3. We also compare the impact on the RBS/C spectra of the particular technique to calculate the defect configurations in silicon, the Tersoff empirical potential and VASP for ab-initio calculations.

In addition to the above mentioned deterministic defect models, simulations were

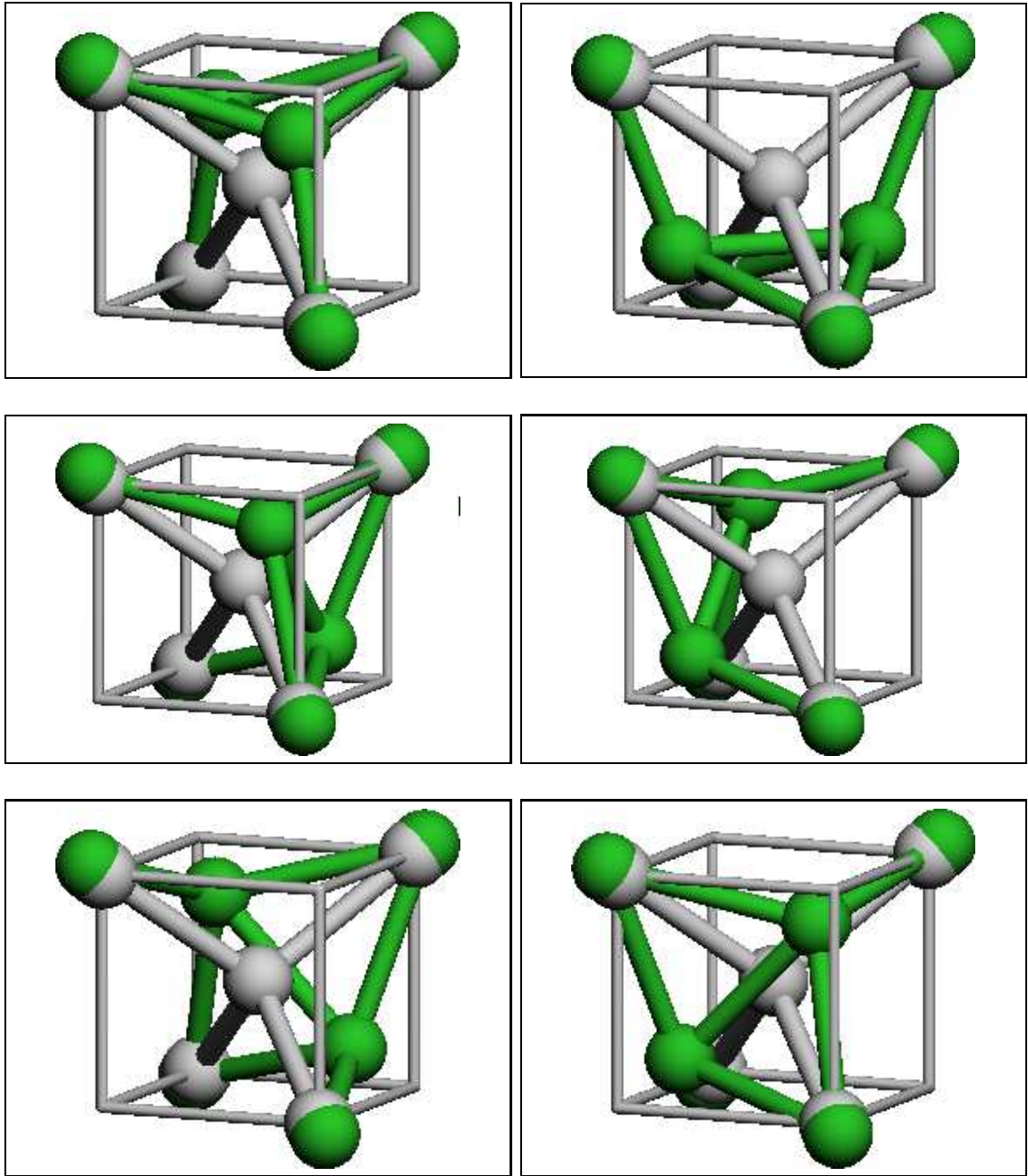
split- $\langle 110 \rangle$ interstitial

Figure 4.13: Ball and stick representation of 6 symmetry equivalent orientations for split- $\langle 110 \rangle$ interstitial. Light colored atoms represent the ideal lattice positions, while dark colored represent the actual atom position, including defective atoms [78].

also performed in the framework of the random model, where defects consist of atoms randomly displaced from original sites with no deformation induced in the surrounding lattice. Despite that this picture of randomly displaced damage in perfect lattice is not quite physical, it is still widely used as the standard method for the extraction of disordered profiles from RBS/C spectra [59].

4.4.1 Computational details

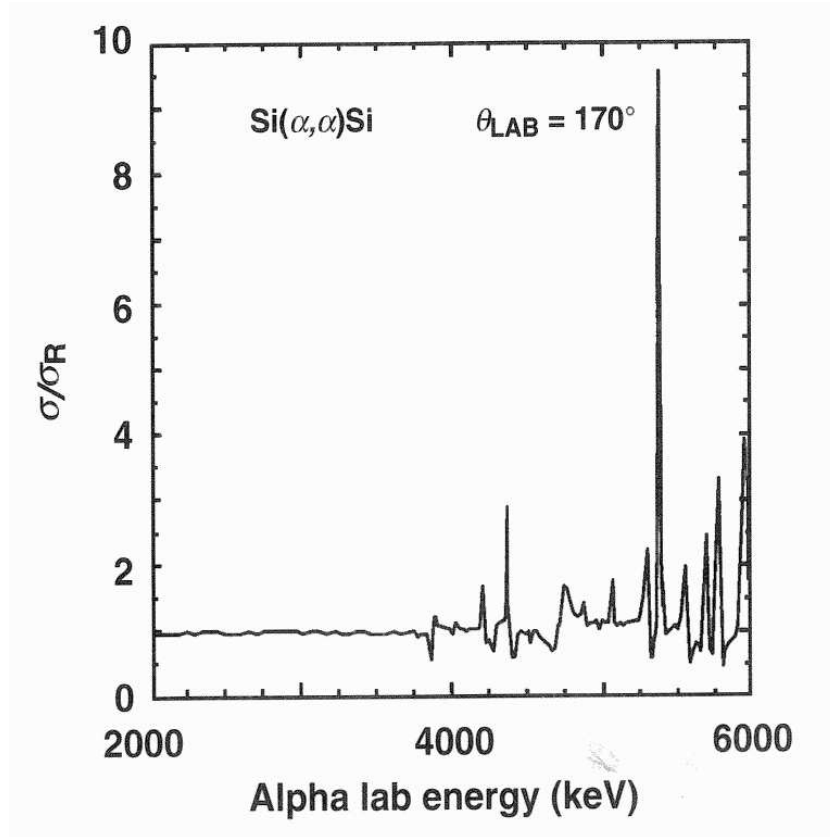


Figure 4.14: Ratio of experimentally measured and Rutherford cross section for He in Si target for the scattering angle of 170° [139].

Using procedure presented in Section 4.3 the simulation cell with a size of $10 \times 10 \times 2000$ unit cells is populated with 2% defect concentration. In order to investigate the im-

part of the different methods for calculation of the coordinates of the atomic defects (ab-initio or empirical potential) on the RBS/C simulation, the original configuration of defects is preserved and the supercell is not relaxed before the RBS analysis is performed. Due to possible overlap of strained regions stemming from neighboring defects, we have limited our analysis to a uniform, rather small concentration of defects, where their mutual interactions are not expected to play important role. The analyzing ions were 3 MeV He^+ beam, with backscattering angle of 170° . In this energy range and for this combination of target and projectile there are no significant deviations of the scattering cross-section from the Rutherford one. Correction to the Rutherford cross section for the case of 3 MeV He^+ ions in Si can be neglected. L'Ecuyer's formula (Eq. 4.5) gives a value of 0.999875, and Bozoian formula (Eq. 4.10) gives E_{NR} of 4 MeV. The experimentally measured cross section for He in Si for the 170° scattering angle is shown in Fig. 4.14 confirming that the ratio between the measured and the Rutherford cross section is rather flat and close to unity up to the energy of about 4 MeV. Therefore, for this ion-target combination in this energy range we can assume that, with negligible error, the scattering is purely Rutherford and can be described with Eq. 4.3.

In order to keep simulation times reasonable, defects are restricted to a columnar domain with lateral dimensions which corresponds to the column width. In BC the starting points of the ion trajectories are randomly generated in the intersection of the surface and the column, but the collision cascade is allowed to develop in the whole target. Defects around the ion trajectories are generated by assuming periodicity in the lateral directions. The size of the column in lateral directions therefore determines the statistical quality of the results and the computation time. Illustration of laterally periodic conditions is shown at Fig. 4.15. The size of the cell can be arbitrary, the here chosen cell size of 1.6 million atoms (10x10x2000 unit cells) is the compromise between the statistical quality of the calculation and the available resources.

4.4.2 Results and discussion

Fig. 4.16 shows the $\langle 001 \rangle$, $\langle 011 \rangle$ and $\langle 111 \rangle$ aligned RBS/C spectra of unrelaxed system cells containing a uniform damage concentration for different defect models. The cell was populated by the defects and their strain fields, the coordinates of which were

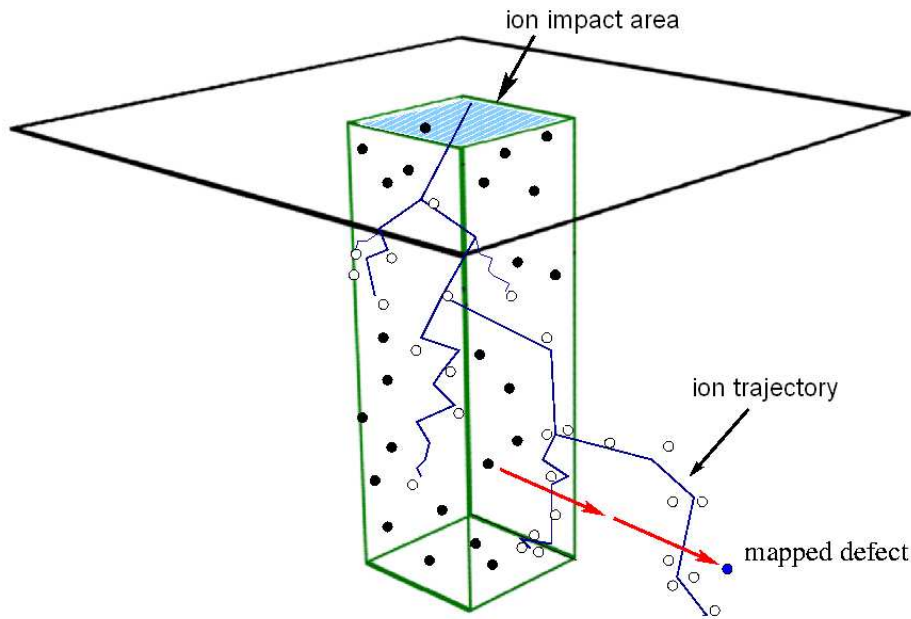


Figure 4.15: *Illustration of lateral periodic conditions used in simulations [47].*

calculated either from ab-initio or classical potential simulations. For each defect type the number of clusters is calculated to give a uniform concentration of 2% of excess atoms in the sample, and an appropriate concentration of vacancies is introduced to balance these excess atoms. For comparison we have also plotted the RBS/C spectra of the model using the random model of damage and of the virgin sample.

From the figures it can be seen that the random model of damage underestimates the RBS/C yield of the split- $\langle 110 \rangle$ and four-interstitial cluster in all investigated channeling directions. This implicitly means that more damage would be necessary to obtain certain RBS/C yield when the damage is in the form of the random interstitial than the split- $\langle 110 \rangle$ or four-interstitial cluster. Since the displacement of atoms randomly placed into the lattice is on average smaller than that characteristic of the split- $\langle 110 \rangle$ and four-interstitial, they give smaller contributions to the increase of the RBS/C signal. In case of the di- and tri-interstitial cluster the efficiency strongly depends on the calculation method. Ab-initio coordinates of di- and tri- interstitials give larger $\langle 001 \rangle$ and $\langle 111 \rangle$ RBS/C efficiency than the random interstitial model, while the results are

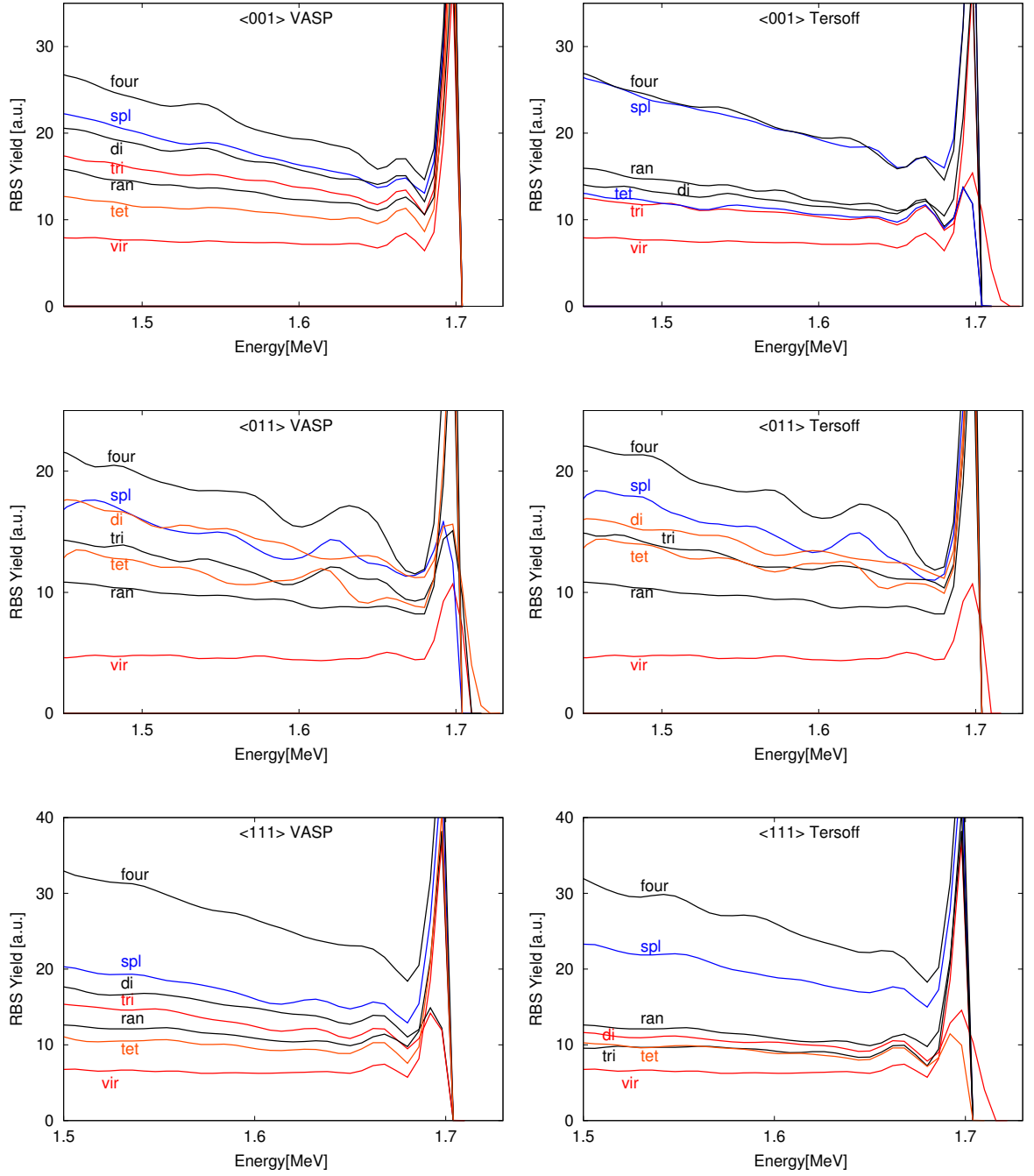


Figure 4.16: RBS/C spectra obtained by 3 MeV He^+ ions in $\langle 001 \rangle$ alignment for different models of self-interstitial clusters: split- $\langle 110 \rangle$ interstitial (spl), di-interstitial (di), tri-interstitial (tri), four-interstitial (four), and tetrahedral interstitial (tet), using atom positions and strain from ab-initio simulations (left) and empirical potential (right). Spectra labeled with 'ran' and 'vir' represent results for the random model of damage and virgin material, respectively.

reverse when the coordinates are calculated with classical potentials. In addition from Fig. 4.16 we conclude that the random interstitial model gives the smallest efficiency among all defect models except for the tetrahedral interstitial, when their coordinates are taken from ab-initio calculations.

It is important to note that the random interstitial model shows its isotropic behavior giving about the same RBS/C signal in all three alignment directions. Since the RBS/C signal is dependent on the actual atom position and its projection in the particular channel a nonisotropic behavior in case of the deterministic defect models can clearly be seen. In particular, each defect gives rise to a different RBS/C signal dependent of the actual alignment. The anisotropy in the RBS/C yield may prevent a multiaxial fitting of RBS/C experiments with a single distribution of one defect type, what should be taken into account when fitting the experimental results. Furthermore, the influence of strained regions is evident in the case of the tetrahedral interstitial, which is shadowed by rows of atoms in $\langle 001 \rangle$ and $\langle 111 \rangle$ direction and would thus give without strain an RBS/C yield close to the virgin sample (See also Fig. 4.22). This leads to the clear conclusion that the influence of the strained atoms around the defects must not be neglected as it is done in the standard approach.

A qualitative difference in the obtained RBS/C yield for the same assumed defect type but calculated with different calculation method is obvious. In order to qualitatively investigate this influence in Fig. 4.17 we compare the normalized RBS/C yield calculated in $\langle 001 \rangle$, $\langle 110 \rangle$ and $\langle 111 \rangle$ alignment of the same system as in Fig. 4.16, when the coordinates of defects and strained regions are calculated either by ab-initio or the Tersoff III potential. The normalized yield is calculated as the integral of the RBS/C spectrum in the energy interval of $1.45 - 1.6 \text{ MeV}$, divided by the integral of the amorphous spectrum.

The results for the case of $\langle 001 \rangle$ and $\langle 111 \rangle$ alignment clearly show that the difference in yield is significant and can be as high as 30%. I_1 gives higher $\langle 001 \rangle$ and $\langle 111 \rangle$ efficiency when their coordinates are calculated with the Tersoff potential, while I_2 and I_3 are more efficient when their configurations are taken from ab-initio calculations. In the case of $\langle 110 \rangle$ alignment the difference is not so pronounced.

Also, for all presented alignments, the RBS/C yield of split- $\langle 110 \rangle$ and four-interstitial is larger than the corresponding yield of di-, tri- and tetrahedral interstitial. This dif-

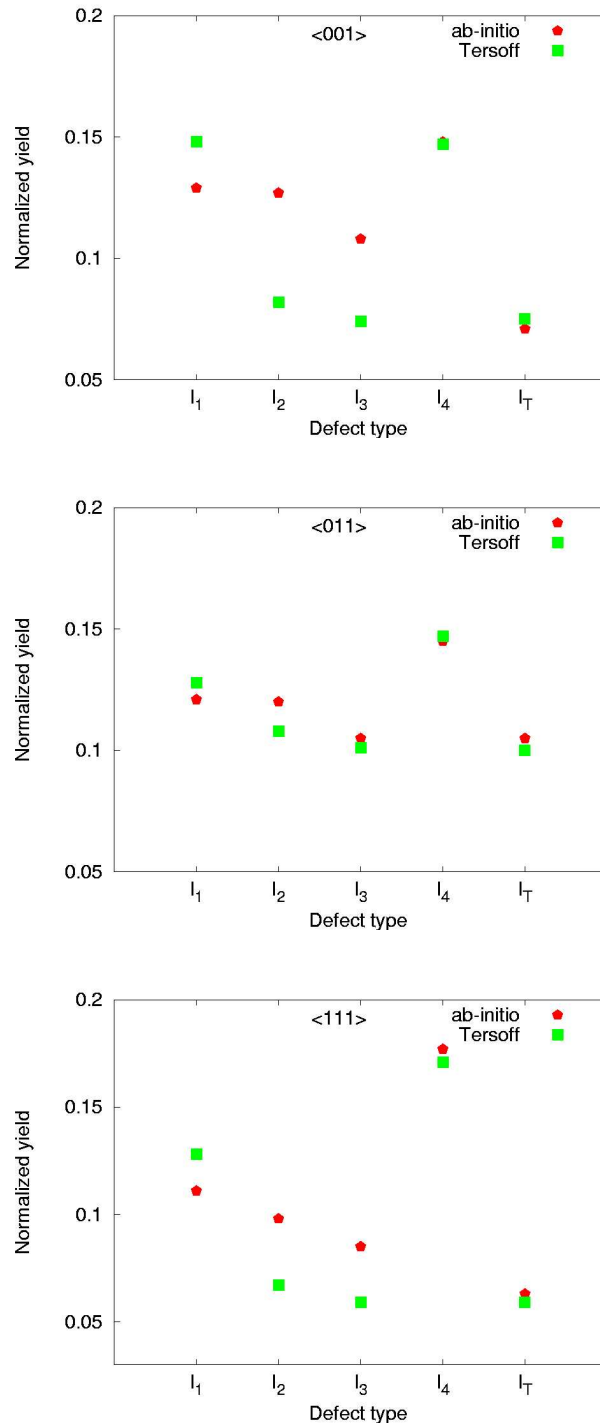


Figure 4.17: Normalized $\langle 001 \rangle$, $\langle 011 \rangle$ and $\langle 111 \rangle$ RBS/C yield of different defect types using two methods to calculate atom positions and strain: classical potentials (Tersoff) and ab-initio. Defect types: split- $\langle 110 \rangle$ interstitial (I_1), di-interstitial (I_2), tri-interstitial (I_3), four-interstitial (I_4), and tetrahedral interstitial (I_T).

ference can be explained by the different number of defective atoms at one lattice site. In case of split- $\langle 110 \rangle$ and four- interstitial we have twice as many defective atoms as excessive atoms, while the di-, and tri-interstitial have 3 or 4 defective atoms with 2 and 3 excess atoms, respectively (see also Fig. 4.11). Therefore, keeping the concentration of excessive atoms constant (in this case 2%) more defective atoms are introduced in the case of split- $\langle 110 \rangle$ and four interstitial than in the case of di- and tri- interstitial.

The difference in the RBS/C efficiency of the assumed defect type when the coordinates are calculated with different method can be illustrated by the slightly different bond lengths. Despite the fact that both methods yield qualitatively the same configurations, the quantitative difference in the bond lengths leads to different projections of the defective atoms into the investigating channels, leading to significantly different RBS/C yields. In the ab-initio calculations the bond lengths between defective atoms for all defect types are in the range of 2.21 - 2.47 Å, which is in the range of the ideal bond lengths in silicon of 2.35 Å. The empirical potential calculations gave us bond lengths up to 3.20 Å.

In order to qualitatively investigate this differences and their influences on RBS/C yields we present and compare in Figs. 4.18, 4.19, 4.20, 4.21, 4.22 the projections of the used defect configurations in the $\langle 100 \rangle$, $\langle 110 \rangle$ and $\langle 111 \rangle$ channel, when the defect coordinates are calculated with both mentioned methods.

As it can be seen the differences in the projection of the defects in the $\langle 100 \rangle$ and $\langle 111 \rangle$ channels are generally larger than in case of the $\langle 110 \rangle$ channel.

From Fig. 4.18 we can see that the defective atoms of the split- $\langle 110 \rangle$ interstitial are more projected into the $\langle 100 \rangle$ and $\langle 111 \rangle$ channel for the case of the Tersoff III potential what leads to the higher corresponding RBS yield in Fig. 4.17. Di-interstitial and tri-interstitial have larger projection of defective atoms into the $\langle 100 \rangle$ and $\langle 111 \rangle$ channel, gained from ab-initio calculations.

In case of the tetrahedral and four-interstitial defect both calculation methods gained almost the same bond lengths which is illustrated in Figs. 4.21 and 4.22. Negligible differences in the corresponding RBS/C yield from Fig. 4.17 can be assigned to the strained atoms.

Also, interesting to point out is that in case of the $\langle 110 \rangle$ channel, which is the most open channel in silicon the difference in atomic configuration does not play such an important role since the differences in RBS/C yield are weak for all defect types. One of the reason can be that the defects are already significantly displaced into $\langle 110 \rangle$ channel, so the further difference in the projection does not significantly enhance the RBS signal.

The presented results confirm the assumption that a direct relationship between the defect projection into the channel and the corresponding RBS/C yield can be established. The bond length influences the projection of the particular defect type in the channel, which in turn affects the corresponding RBS/C yield.

Beside the influence of the bond lengths to the RBS/C yield additional impact of the defective atoms can be found. Although defective atoms of some defect types are placed in the walls of the particular channel, for example split- $\langle 110 \rangle$ interstitial from ab-initio calculations in the $\langle 100 \rangle$ and $\langle 111 \rangle$ direction, they can increase the backscattering yield by means of increasing the dechanneling probability of the ion which change the channel.

From the presented result it can be concluded that the Tersoff potential gives a large variation of the backscattering yield depending on the assumed defect type while ab-initio calculations lead to much less variation in the system studied with the exception of the tetrahedral interstitial and the four-interstitial cluster. Since the split- $\langle 110 \rangle$, di- and tri-interstitial have the same building unit, similar behavior is expected, what is not the case for the tetrahedral and the four interstitial cluster whose building units are different.

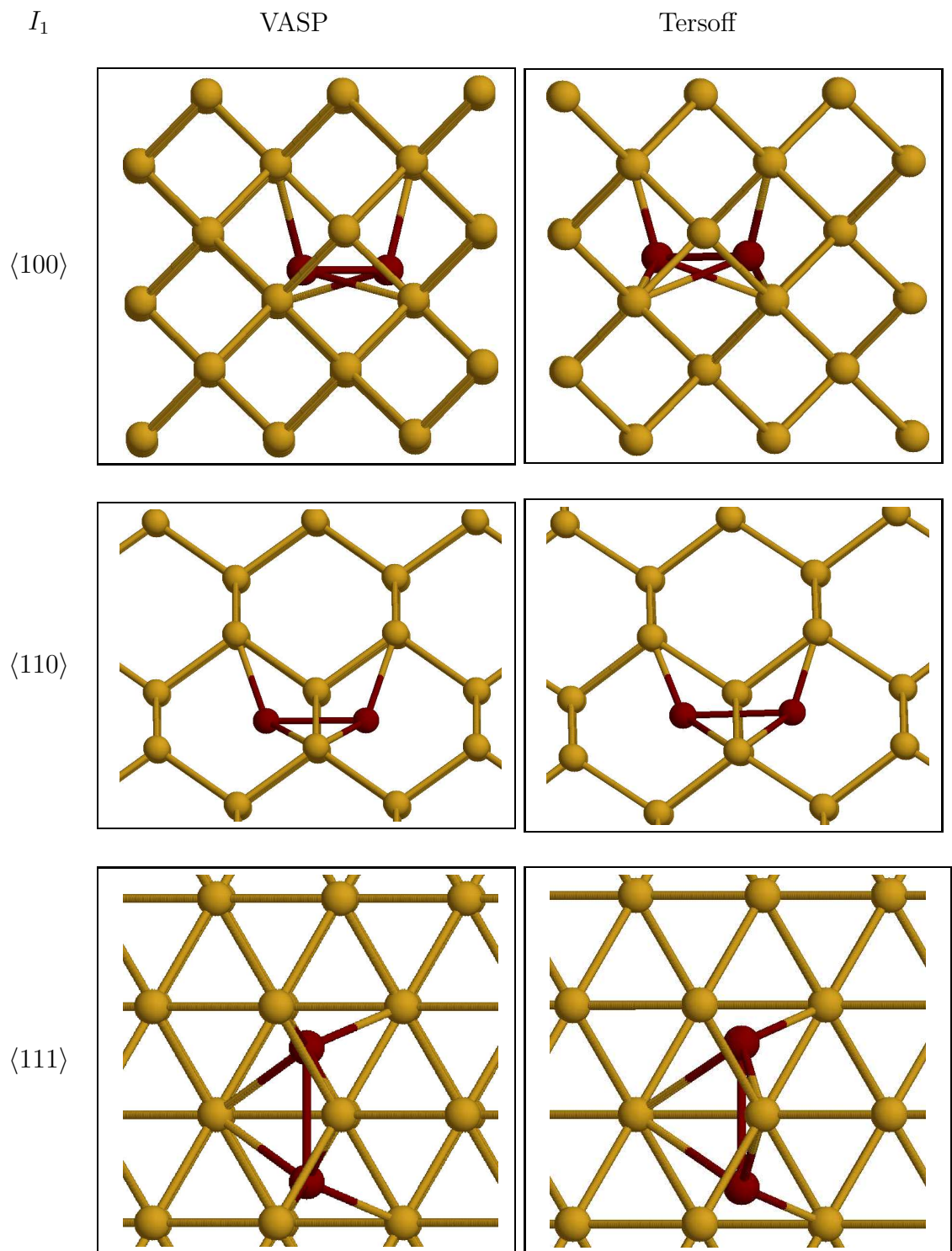


Figure 4.18: *Split- $\langle 110 \rangle$ interstitial showing the differences in projection into $\langle 100 \rangle$, $\langle 110 \rangle$ and $\langle 111 \rangle$ channel when the defect coordinate are calculated with ab-initio (left) and classical potential (right) calculations.*

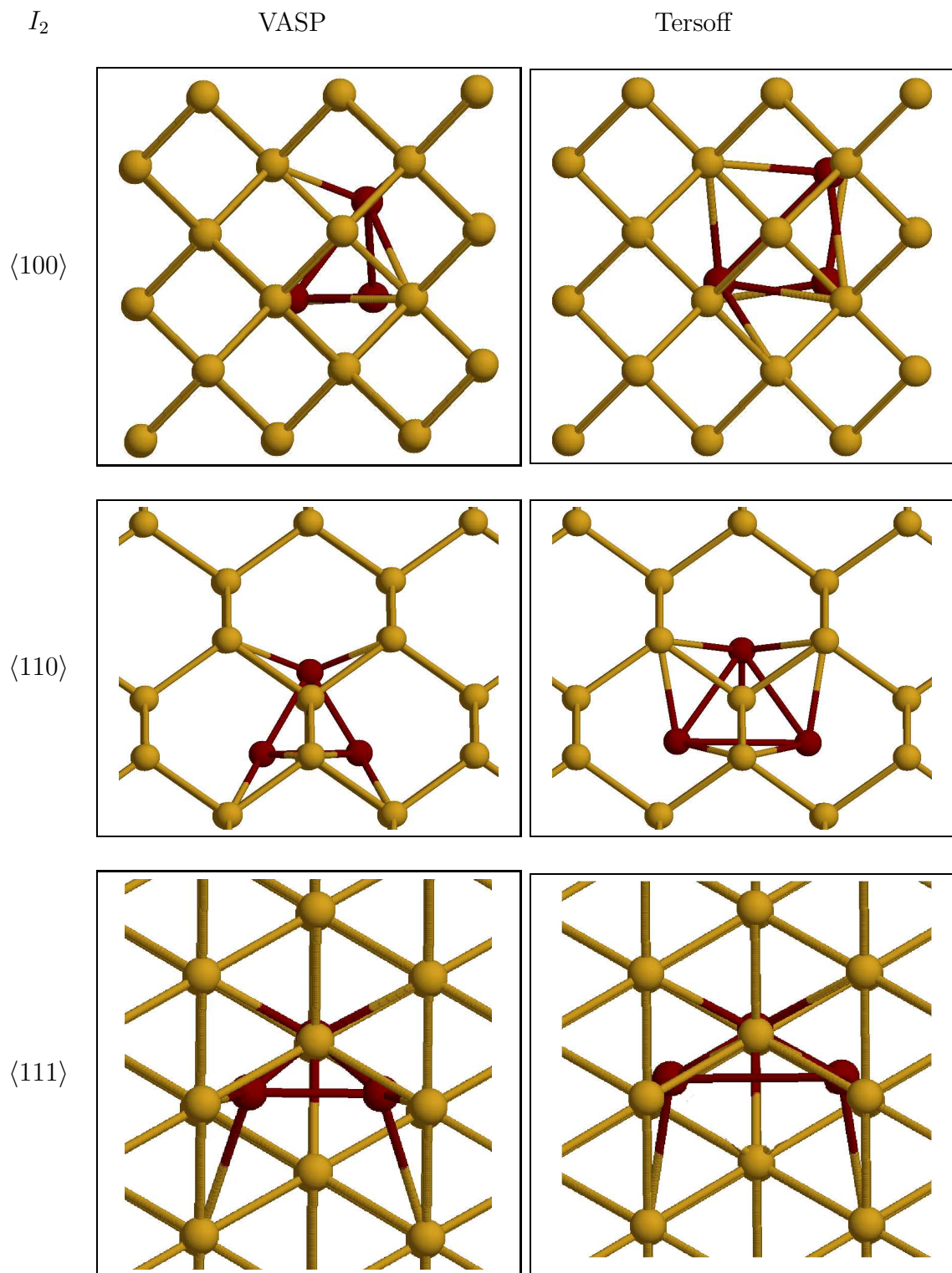


Figure 4.19: Di-interstitial showing the differences in projection into $\langle 100 \rangle$, $\langle 110 \rangle$ and $\langle 111 \rangle$ channel when the defect coordinate are calculated with *ab-initio* (left) and classical potential (right) calculations.

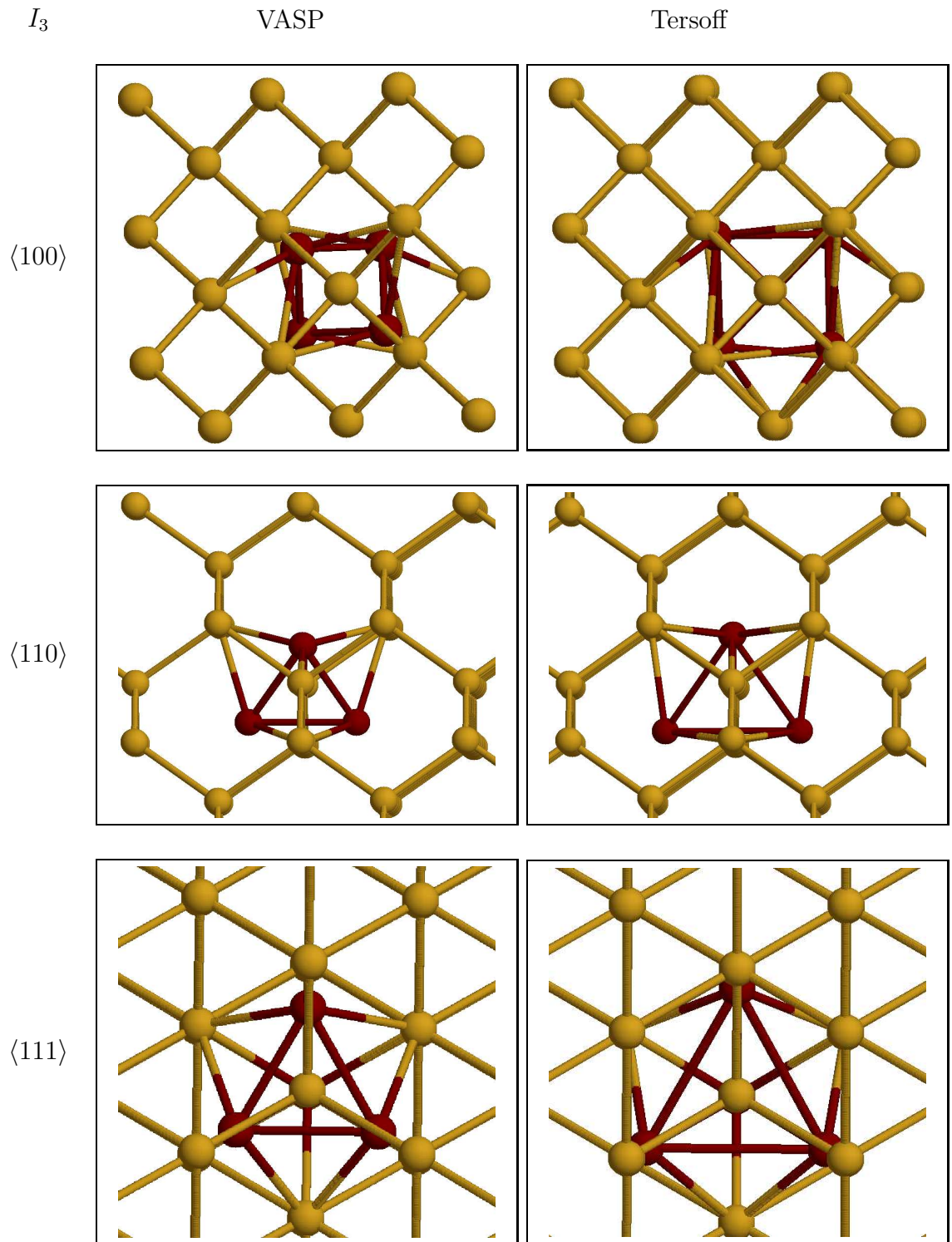


Figure 4.20: Tri-interstitial showing the differences in projection into $\langle 100 \rangle$, $\langle 110 \rangle$ and $\langle 111 \rangle$ channel when the defect coordinate are calculated with ab-initio (left) and classical potential (right) calculations.

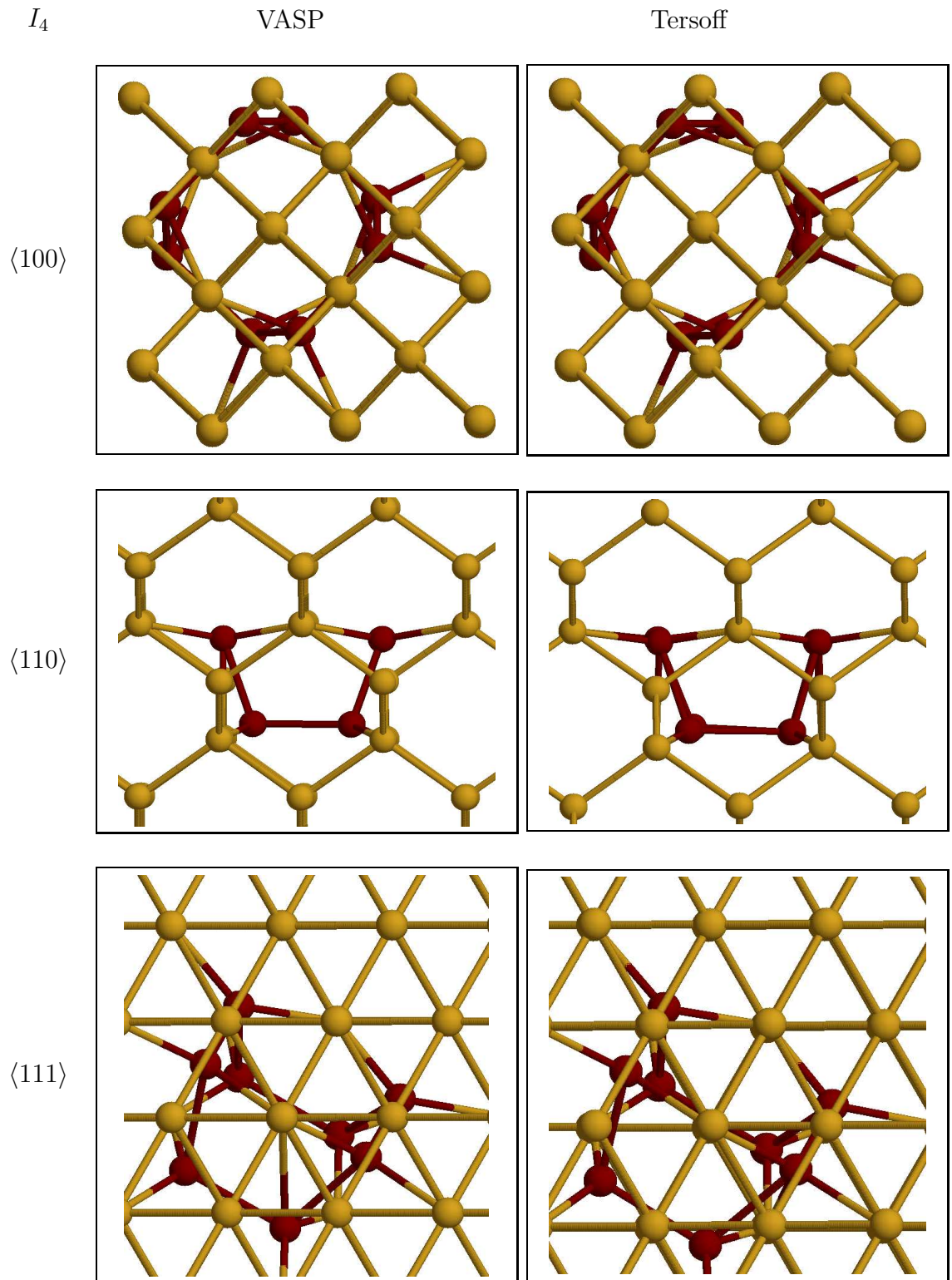


Figure 4.21: Four-interstitial showing the differences in projection into $\langle 100 \rangle$, $\langle 110 \rangle$ and $\langle 111 \rangle$ channel when the defect coordinate are calculated with ab-initio (left) and classical potential (right) calculations.

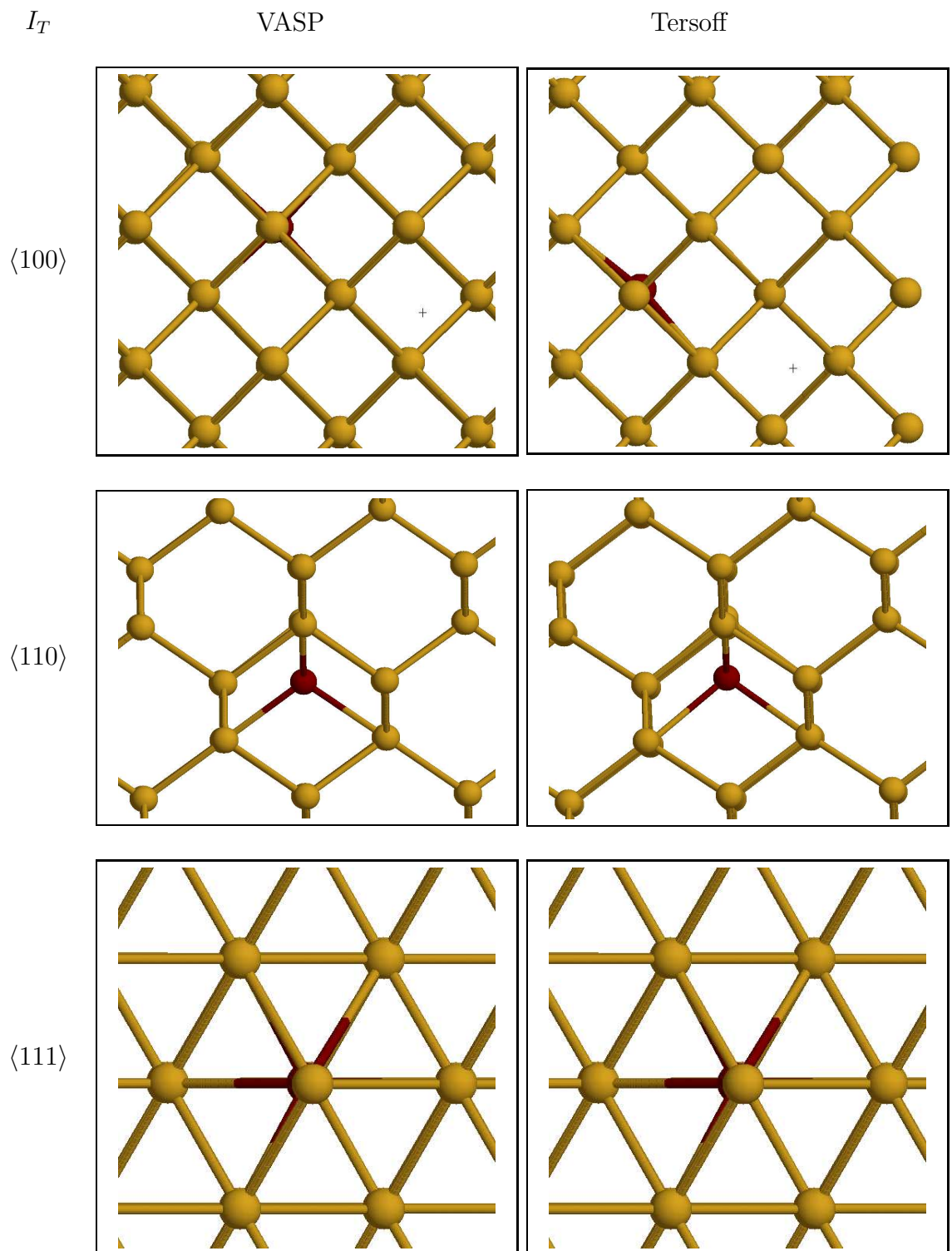


Figure 4.22: Tetrahedral-interstitial showing the differences in projection into $\langle 100 \rangle$, $\langle 110 \rangle$ and $\langle 111 \rangle$ channel when the defect coordinate are calculated with ab-initio (left) and classical potential (right) calculations.

4.5 Influence of defect relaxation and mutual interaction

4.5.1 Introduction

In rather low damaged samples, considered in Section 4.4, the mutual defect interactions are weak and disorder can be presented as a distribution of simple defects, each one surrounded by strained region which does not significantly overlap with the ones generated from neighboring defects. By increasing the damage concentration in the sample the overlapping of the strained regions of nearby defects occurs, which in turn increases the disorder in the originally perfect lattice sites surrounding the defects. By increasing the defect concentration the strain becomes so large that the additional lattice atoms are now being pushed from their lattice positions and therefore displaced, finally giving rise to the sample amorphization.

In order to study the influence of the lattice relaxation and mutual defect interaction on RBS/C spectra for different types of small interstitial clusters we have performed structural relaxation of the supercell populated with varying defect concentrations. The cell is populated with one defect type at the time, adding an appropriate vacancy concentration to balance the excess atoms introduced with particular defect types. The procedure is explained in Section 4.4.1. Although the relaxation of the cell with the ab-initio code VASP would be more accurate, unfortunately such calculation is not computationally feasible. Therefore the simulation supercell is relaxed with the Tersoff III potential by quenching from 300K down to 0K for 5 ps in order to obtain the final configuration.

4.5.2 Results

In Figs. 4.23, 4.24, 4.25, 4.26, 4.27 we compare the normalized $\langle 100 \rangle$ RBS/C spectra of the relaxed and unrelaxed supercell as a function of damage concentration for the different defect types. In addition, for comparison purposes, the results obtained with the random interstitial model are plotted. The normalized yield is calculated as the integral of the RBS/C spectrum in the energy interval of 1.45 – 1.6 MeV, divided

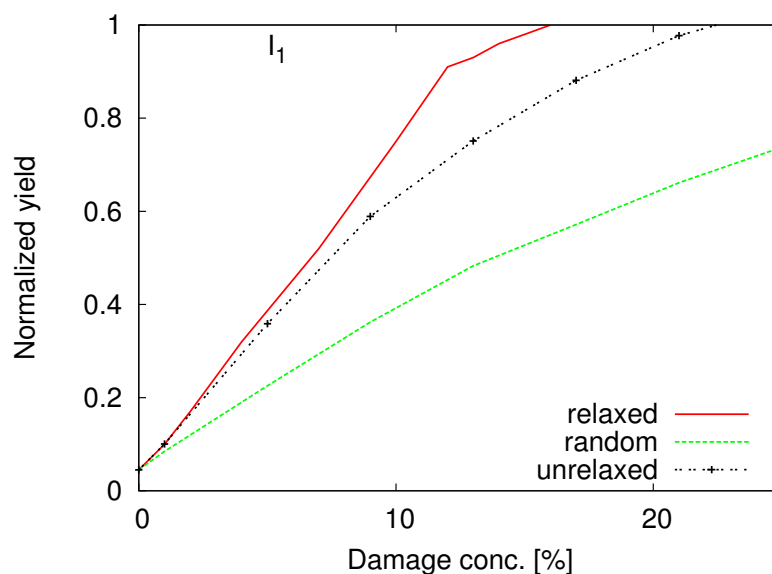


Figure 4.23: Normalized $\langle 100 \rangle$ RBS/C yield of split- $\langle 110 \rangle$ interstitial (I1) compared for relaxed cell (relaxed) and unrelaxed cell (unrelaxed) showing the importance of mutual interaction. The line labeled with “random” represents the yield obtained with random interstitial model.

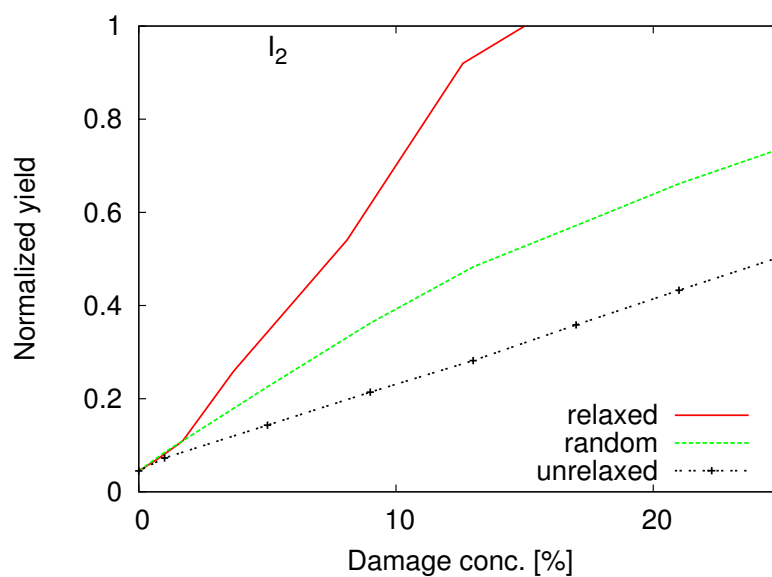


Figure 4.24: Normalized $\langle 100 \rangle$ RBS/C yield of di-interstitial (I2) compared for relaxed cell (relaxed) and unrelaxed cell (unrelaxed) showing the importance of mutual interaction. The line labeled with “random” represents the yield obtained with random interstitial model.

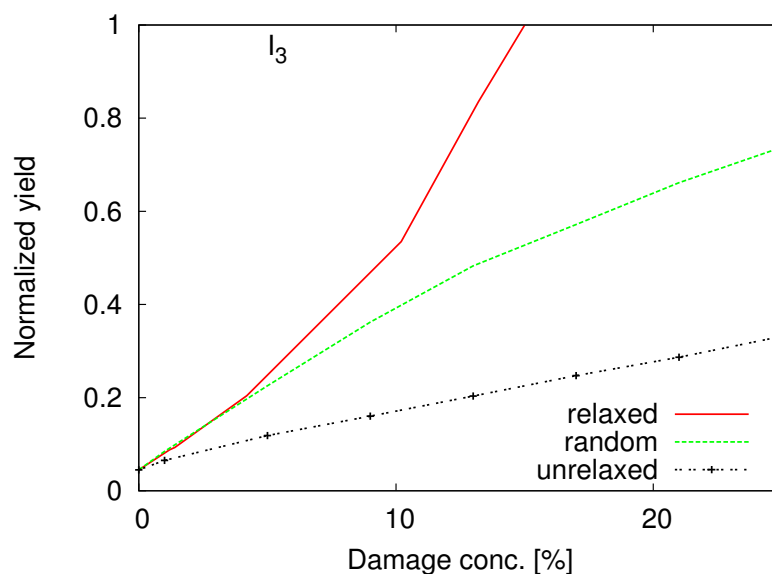


Figure 4.25: Normalized $\langle 100 \rangle$ RBS/C yield of tri-interstitial (I₃) compared for relaxed cell (relaxed) and unrelaxed cell (unrelaxed) showing the importance of mutual interaction. The line labeled with “random” represents the yield obtained with random interstitial model.

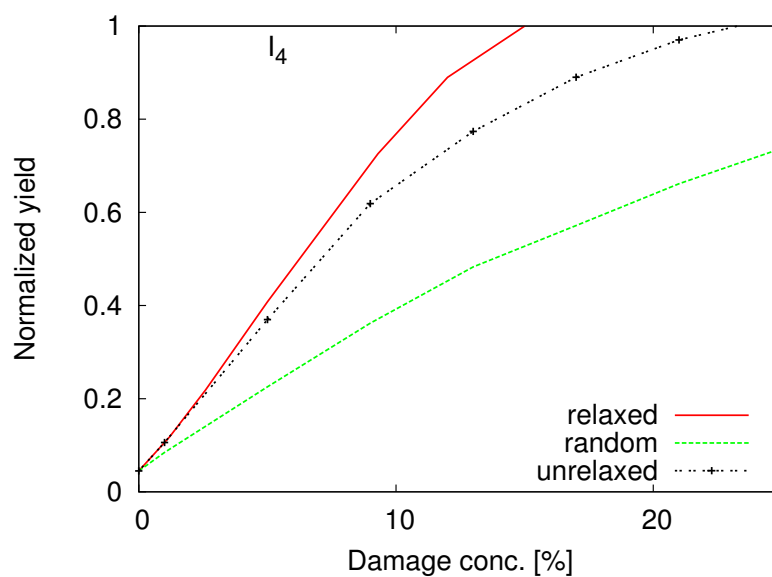


Figure 4.26: Normalized $\langle 100 \rangle$ RBS/C yield of four-interstitial (I₄) compared for relaxed cell (relaxed) and unrelaxed cell (unrelaxed) showing the importance of mutual interaction. The line labeled with “random” represents the yield obtained with random interstitial model.

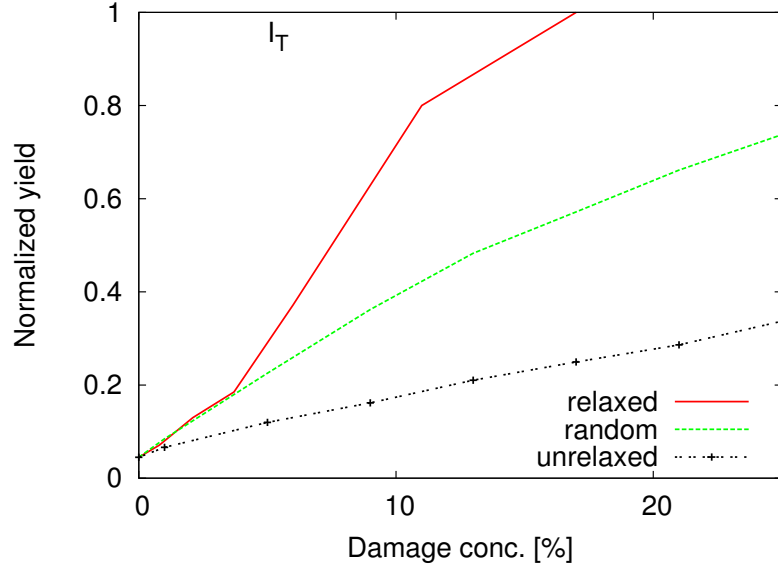


Figure 4.27: Normalized $\langle 100 \rangle$ RBS/C yield of tetrahedral interstitial (I_T) compared for relaxed cell (relaxed) and unrelaxed cell (unrelaxed) showing the importance of mutual interaction. The line labeled with “random” represents the yield obtained with random interstitial model.

by the integral of the amorphous spectrum. As it is expected random interstitial and nonrelaxed deterministic model shows mainly linear dependence of RBS/C yield as a function of defect concentration for almost all defect types. Only in the case of split- $\langle 110 \rangle$ and four-interstitial we have slightly sub-linear behavior. The relaxed supercell shows in general a super-linear trend even at low to middle damage concentration for almost all used defect types. By increasing the defect concentration the superposition of strained fields of nearby defects occurs inducing strong forces displacing more atoms from their lattice positions. In case of the random interstitial and unrelaxed cell the strain is superposed linearly and nonlinear effects cannot occur. For a defect concentration larger than 4-5 % the defects starts to push lattice atoms from their crystallographic positions inducing further displacements and material amorphization, thus contributing to the super-linear dependence of the RBS/C yield. Also strong deviation of the non-relaxed from the relaxed system is significant for the case of di- and tri- and tetrahedral interstitial even at relative defect concentration of about 2-3%, which limits the usability of non-relaxed model in case of these defect types. For the split- $\langle 110 \rangle$ and the four-interstitial cluster the deviation becomes significant at relative

defect concentration of 6-7%.

As a result of the increase of the strain generated by the lattice relaxation we get the super-linear trend of RBS/C disorder versus defect concentration in the range of intermediate damage density. This fact disconfirms the result obtained by usual description of randomly displaced defects surrounded by perfect lattice.

4.6 Conclusions

We can conclude that the model based on the atomic-scale defects improves the physical description of the damage used for the interpretation of RBS/C spectra of ion implanted Si.

The enhancement in RBS/C yield has been shown to be dependent on the calculation method used to calculate the defect structure, and the type of defect, and on the channeling direction.

The damage model based on atomic-scale defects takes into account the strain induced by the presence of these defects, which is not the case in the random interstitial model. The influence of the strained fields is not negligible and is clearly illustrated for the tetrahedral interstitial cluster. The important consequence is if the strain is neglected the amount of damage extracted from RBS/C analysis may be significantly overestimated. Also, the contribution of the deterministic defects like the split- $\langle 110 \rangle$ and four-interstitial to the disorder and RBS/C yield is larger than the contribution obtained from randomly displaced atoms surrounded by the perfect lattice. This is explained with the fact that the defective atoms in these configurations are on average more displaced than in the case of random interstitial, therefore giving higher a contribution to the RBS/C yield. Because of the different projections of the particular defect type into the investigating channel, the atomic-scale models show clear anisotropic behavior dependent on the channeling direction.

Furthermore, the influence of the defect models and their correct coordinates is critical. For the same damage level the difference in RBS yield on the assumed defect type can be up to a factor of two. Also, the RBS/C yield calculated from empiri-

cal interatomic potentials may significantly deviate from that obtained using atomic coordinates from ab-initio calculations. These differences are due to the inherently approximative nature of empirical interatomic potentials. In addition, the variation of the backscattering yield with the assumed defect type is larger with the defect coordinates obtained by the empirical potential than by the ab-initio calculations. Since the structural model plays an essential role in RBS/C simulations, attention should be paid to these models when fitting the experimental results.

Also, using isolated deterministic defects, even together with the strain, has certain limitations when going to larger damage concentrations. We have to note that although VASP is more accurate than the Tersoff empirical potential, the relaxation of such large cell with the VASP is not feasible, and the presented results obtained with relaxed supercell may be influenced by the used empirical potential. For the damage levels of more than about 5% the mutual defect interaction plays an essential role determining the RBS yield, where the isolated defect model begins to cancel off. In this region a super-linear dependence of the RBS/C yield on damage concentration can be seen. The strain induced by lattice relaxation increases its contribution to disorder with increasing the defect concentration leading to the super-linear increase of the RBS/C damage in the low-middle damage concentration regime. Amorphization of the sample occurs at the concentration of about 15% for all used defect types.

Chapter 5

Conclusion and Outlook

Within this thesis we have proposed new simulation methods able to simulate effects that cannot be explained with the classical approach based on the displacement energy. Using existing and developing new models we have improved the physical understanding of ion implantation induced damage.

We have developed a model based on a coupled BC/heat flow approach which describes well the energy and the ion mass dependence of the ion mass as well as the polyatomic effect at cryogenic temperatures. The initial energy distribution is obtained by the existing BC code and the subsequent heat quenching step is simulated by the heat flow simulator that is developed for the purpose of this thesis. From our simulations it can be concluded that considering the lattice collapse once the damage level exceeds a critical value is essential for the prediction of the size of the amorphous pockets. Introduction of the heat of melting and the neighboring atoms in the melting criterion was important but not sufficient to obtain good agreement with experimental results. We have demonstrated that the heat diffusion law, even with both the heat of melting and the requirement that the nearest neighbors meet the melting criterion, is capable to neither quantitatively nor qualitatively account the amorphization process. A significant improvement can be obtained by assuming that the lattice collapses to the amorphous state once the damage density exceeds 10%. With this model we have got the qualitative as well as quantitative agreement for the number of displaced atoms after implantation of various ion species (P, As, Te, Tl) including molecular ions (P_2 , As_2 , Tl_2) and for a wide range of energies.

For the purpose of this thesis a RBS/C simulation code is developed and tested.

The code uses the concepts of the Rutherford backscattering cross section and the close nuclear encounter probability. Atomic-scale modeling of defect structures was used to determine the location of interstitial atoms in the host lattice. A new atomistic model of damage which introduces atomic-scale defects, coordinates of which are calculated with ab-initio or classical MD calculations was proposed. The enhancement in the RBS/C yield has been shown to be dependent on the calculation method used to calculate the defect structure, and the type of defect, and on the channeling direction. We find differences in the RBS/C yields up to of 30% for the same assumed defect type, when the defect coordinates are calculated by two different methods. The RBS/C yield calculated from empirical interatomic potentials significantly deviates from that obtained using atomic coordinates from ab-initio calculation. Also, the dependence of the backscattering yield on the assumed defect type is larger with the defect coordinates obtained by the empirical potential than by the ab-initio calculations. These differences are due to the inherently approximative nature of the empirical potentials. Since the structural model plays a very important role more attention should be paid to these models when fitting the experimental results. The non-negligible role of the strain around the defects is indicated as well as the defect anisotropy when multiaxial measurement of RBS/C spectra is performed. Finally, the approach based on the isolated defect structures and their strained fields is found to be limited to concentrations less than about of 6-7% of the atomic density. The proposed model improves the physical picture of the damage used in RBS/C models and establishes a quantitative correlation between the microscopic defect models and the macroscopic RBS/C yield under the condition of a low concentration of weakly interacting point defects.

The importance of the multiscale modeling is illustrated by the conclusion that the proposed amorphous pocket model may benefit from the investigations of the influences of the atomic-scale defects on the RBS/C signal.

In order to further improve the understanding of the damage physics the following questions should be treated:

- More investigations on the influence on the RBS/C yield of the atoms contained in amorphous pockets should be done. These results could yield a correction to the factor of “+1” used to count the atoms within the amorphous pockets.
- The proposed amorphous pocket model could be incorporated into a complete

multi-scale modeling scheme, as an interim step, gaining its full advantage upon heavy ion implantations at low temperatures. The proposed scheme could be: BCA for the damage generations \rightarrow proposed amorphous pocket model for the heat quenching and detection of displaced atoms \rightarrow kLMC for the subsequent damage annealing at higher temperatures.

- The proposed atomistic model of damage in RBS/C simulations is awaiting the testing and comparison with experimental data. Fitting the experimental data could give more information about the abundance of different defect types in the damaged sample and be used to validate and improve the configurations of the used atomic-scale defects.

Appendix A

Acronyms and Symbols

A.1 List of Acronyms

BC binary collision

BCA binary collision approximation

CM center of mass

CPDD Critical point defect density

EOR End of range

IBIEC ion beam induced epitaxial crystallization

IBIIA ion beam induced interfacial amorphization

kLMC kinetic lattice Monte Carlo

kMC kinetic Monte Carlo

LAB laboratory

LNT liquid nitrogen temperature

MC Monte Carlo

MD molecular dynamics

RBS Rutherford backscattering

RBS/C Rutherford backscattering/channeling

RT room temperature

SIMS secondary ion mass spectrometry

TEM transmission electron microscope

VASP Vienna ab-initio simulation program

A.2 List of Frequently Used Symbols

Symbol	Description
a_{latt}	lattice constant
c_p	specific heat
D	thermal diffusivity
$d\sigma/d\Omega$	differential backscattering cross section
E	energy
E_{melt}	heat of melting
I_1	split- $\langle 110 \rangle$ interstitial
I_2	di-interstitial
I_3	tri-interstitial
I_4	four-interstitial
I_T	tetrahedral-interstitial
m_1	ion mass
m_2	target mass
p	impact parameter
P_{RBS}	RBS reaction probability
\vec{q}	heat flux
T	temperature
$T_{i,j}$	temperature of jth neighbor of atom i
T_m	melting temperature
z_1	ion atomic number
z_2	target atomic number
λ	thermal conductivity
ρ	Si mass density
χ	normalized RBS yield
ψ	laboratory backscattering angle
Ω	detector solid angle

Bibliography

- [1] S. Tian, M. F. Morris, S. J. Morris, B. Obradovic, G. Wand, A. F. Tasch, and C. M. Snell, A detailed physical model for ion implant induced damage in silicon, *IEEE Trans. on Elec. Dev.* **45**, 1226 (1998).
- [2] M. Caturla, T. Diaz de la Rubia, L. Marques, and G. Gilmer, Ion-beam processing of silicon at keV energies: A molecular dynamics study, *Phys Rev.* **B 54**, 16683 (1996).
- [3] S. K. Estreicher, Structure and dynamics of point defects in crystalline silicon, *Phys. Stat. Sol.* **B 217**, 513 (2000).
- [4] International technology roadmap for semiconductors, <http://public.itrs.net>, 2005.
- [5] G. Kinchin and R. Pease, The displacement of atoms in solids by radiation, *Rep. Prog. Phys.* **18**, 1 (1955).
- [6] D. Thompson and R. Walker, Energy spikes in Si and Ge due to heavy ion bombardment, *Radiat Eff.* **36**, 91 (1978).
- [7] G. Hobler and G. Otto, Status and open problems in modeling as-implanted damage in silicon, *Mat. Sci. Semicond. Proc.* **6**, 1 (2003).
- [8] G. Hobler, Monte Carlo simulation of two-dimensional implanted dopant distributions at mask edges, *Nucl. Instr. Meth.* **B 96**, 155 (1995).
- [9] H. Cerva and G. Hobler, Comparison of transmission electron microscope cross sections of amorphous regions in ion implanted silicon with point-defect density calculations, *J. Electrochem. Soc.* **139**, 3631 (1992).
- [10] G. Hobler, A. Simionescu, L. Palmetshofer, C. Tian, and G. Stingeder, Boron channeling implantations in silicon: Modeling of electronic stopping and damage accumulation, *J. Appl. Phys.* **77**, 3697 (1995).
- [11] A. Simionescu, S. Herzog, G. Hobler, R. Schork, J. Lorenz, C. Tian, and G. Stingeder, Modeling of electronic stopping and damage accumulation during arsenic implantation in silicon, *Nucl. Instr. Meth.* **B 100**, 483 (1995).

- [12] G. Otto, Multi-method simulations and transmission electron microscope investigations of ion implantation damage in silicon, PhD Thesis, TU Vienna (2005).
- [13] D. A. Thompson, R. S. Walker, and J. A. Davies, Evidence for spike-effects in low-energy heavy-ion bombardment of Si and Ge, *Radiat Eff.* **32**, 135 (1977).
- [14] D. Thompson, A. Golanski, K. Haugen, and D. Stevanovic, Disorder production and amorphization in ion implanted silicon., *Radiat Eff.* **52**, 69 (1980).
- [15] D. Thompson, High density cascade effects, *Radiat Eff.* **56**, 105 (1981).
- [16] L. Howe, M. Rainville, H. Haugen, and D. Thompson, Collision cascades in silicon, *Nucl. Instr. Meth.* **170**, 419 (1980).
- [17] J. Narayan, O. Oen, D. Fathy, and O. Holland, Atomic structure of collision cascades in ion-implanted silicon and channeling effects, *Mater. Lett.* **67**, 143 (1985).
- [18] L. Howe and M. Rainville, Features of collision cascades in silicon as determined by transmission electron microscopy, *Nucl. Instr. Meth.* **182/183**, 143 (1981).
- [19] A. Grob, J. Grob, and A. Golanski, Damage created by BF_n^+ ($1 \leq n \leq 3$) and PF_n^+ ($1 \leq n \leq 5$) implantations, *Nucl. Instr. Meth.* **B 19/20**, 55 (1987).
- [20] A. Titov, S. Kucheyev, V. Belyakov, and A. Azarov, Damage buildup in Si under bombardment with MeV heavy atomic and molecular ions, *J. Appl. Phys.* **90**, 3867 (2001).
- [21] G. Otto, G. Hobler, L. Palmetshofer, K. Mayerhofer, K. Piplits, and H. Hutter, Dose-rate dependence of damage formation in Si by N implantation as determined from channeling profile measurements, *Nucl. Instr. Meth.* **B 242**, 667 (2006).
- [22] S. Prussin and P. F. Zhang, A physical model for the role of dose and dose rate on amorphous depth generation, in *Ion Implantation Technology-96*, pages 555–558, IEEE, Piscataway, 1997.
- [23] O. W. Holland and C. W. White, Ion-induced damage and amorphization in Si, *Nucl. Instr. Meth.* **B 59/60**, 353 (1991).
- [24] F. H. Eisen, B. Welch, J. E. Westmoreland, and J. W. Mayer, Lattice disorder produced in silicon by boron ion implantation, in *Atomic Collision Phenomena in Solids*, edited by D. W. Palmer, M. W. Thompson, and P. D. Townsend, pages 111–127, North-Holland, 1970.
- [25] O. W. Holland, D. Fathy, J. Narayan, and O. S. Oen, Dose rate dependence of damage clustering during heavy ion irradiation in Si, *Radiat. Eff.* **90**, 127 (1985).

- [26] M. Posselt, L. Bischoff, and J. Teichert, Influence of dose rate and temperature on ion-beam-induced defect evolution in Si investigated by channeling implantation at different doses, *Appl. Phys. Lett.* **79**, 1444 (2001).
- [27] L. Bischoff, J. Teichert, and S. Hausmann, Dwell-time dependence of irradiation damage in silicon, *Nucl. Instr. Meth.* **B 178**, 165 (2001).
- [28] F. Priolo and E. Rimini, Ion-beam-induced epitaxial crystallization and amorphization in silicon, *Mater. Sci. Rep.* **5**, 319 (1990).
- [29] T. Henkel, V. Heera, R. Koeqler, W. Skorupa, and M. Seibt, Kinetics of ion-induced interfacial amorphization in silicon, *Nucl. Instr. Meth.* **B 127/128**, 239 (1987).
- [30] G. Otto, G. Hobler, P. Pongratz, and L. Palmetshofer, Is there an influence of ion-beam-induced interfacial amorphization on the a/c-interface depth in silicon at common implantation energies, *Nucl. Instr. Meth.* **B 253**, 227 (2006).
- [31] A. Leiberich, D. M. Maher, R. V. Knoell, and W. L. Brown, Ion-beam induced crystallization and amorphization at a crystalline/amorphous interface in $\langle 100 \rangle$ silicon, *Nucl. Instr. Meth.* **B 19/20**, 457 (1987).
- [32] A. Battaglia, G. Romano, and S. Campisano, Layer by layer amorphization in Si: Temperature, ion mass and flux effects, *Mat. Res. Symp. Proc.* **316**, 253 (1994).
- [33] J. Westmoreland, J. Mayer, F. Eisen, and B. Welch, Production and annealing of lattice disorder in silicon by 200-keV boron ions, *Appl. Phys. Lett.* **15**, 308 (1969).
- [34] S. T. Picraux, J. E. Westmoreland, J. W. Mayer, R. R. Hart, and O. J. Marsh, Temperature dependence of lattice disorder created in Si by 40 keV Sb ions, *Appl. Phys. Lett.* **14**, 7 (1969).
- [35] F. Morehead. and B. Crowder, A model for the formation of amorphous Si by ion bombardment, *Radiat. Eff.* **6**, 27 (1970).
- [36] K. Nordlund, M. Ghaly, R. Averback, M. Caturla, T. D. de la Rubia, and J. Tarus, Defect production in collision cascades in elemental semiconductors and fcc metals, *Phys Rev. B* **57**, 7556 (1998).
- [37] T. Motooka, Model for amorphization processes in ion-implanted Si, *Phys. Rev.* **B 49**, 16367 (1994).
- [38] T. Motooka, Y. Hiroyama, R. Suzuki, T. Ohdaira, Y. Hirano, and F. Sato, Role of defects during amorphization and relaxation processes in Si, *Nucl. Instr. Meth.* **B 106**, 198 (1995).

- [39] T. Motooka, The role of defects during amorphization and crystallization processes in ion implanted Si, *Mat. Sci. Eng.* **A253**, 42 (1998).
- [40] M. Jaraiz, G. H. Gilmer, J. M. Poate, and T. D. de la Rubia, Atomistic calculations of ion implantation in Si: point defect and transient enhanced diffusion phenomena, *Appl. Phys. Lett.* **68**, 409 (1996).
- [41] L. Pelaz, L. A. Marques, G. H. Gilmer, M. Jaraiz, and J. Barbolla, Atomistic modeling of the effects of dose and implant temperature on dopant diffusion and amorphization in Si, *Nucl. Instr. Meth.* **B 180**, 12 (2001).
- [42] L. Pelaz, L. A. Marques, M. Aboy, J. Barbolla, and G. H. Gilmer, Atomistic modeling of amorphization and recrystallization in silicon, *Appl. Phys. Lett.* **82**, 2038 (2003).
- [43] P. Lopez, L. Pelaz, L. A. Marqués, I. Santos, M. Aboy, and J. Barbolla, Atomistic modeling of defect evolution in Si for amorphizing and subamorphizing implants, *Mat. Sci. Eng.* **B 114-115**, 82 (2004).
- [44] L. A. Marques, L. Pelaz, P. Lopez, M. Aboy, I. Santos, and J. Barbolla, Atomistic simulations in Si processing: Bridging the gap between atoms and experiments, *Mat. Sci. and Eng.* **B 124-125**, 72 (2005).
- [45] G. Otto, D. Kovač, and G. Hobler, Coupled BC/kLMC simulations of the temperature dependence of implant damage formation in silicon, *Nucl. Instr. Meth.* **B 228**, 256 (2005).
- [46] G. Hobler and G. Otto, Amorphous pocket model for silicon based on molecular dynamics simulations, *Nucl. Instr. Meth.* **B 206**, 81 (2003).
- [47] G. Hobler, G. Otto, D. Kovač, L. Palmetshofer, K. Mayerhofer, and K. Piplits, Multiscale approach for the analysis of channeling profile measurements of ion implantation damage, *Nucl. Instr. Meth.* **B 228**, 360 (2005).
- [48] G. Lulli, M. Bianconi, A. Parisini, and E. Napolitani, Structural characterization and modeling of damage accumulation in In implanted Si, *J. Appl. Phys.* **95**, 150 (2004).
- [49] G. Lulli, E. Albertazzi, M. Bianconi, A. Satta, S. Balboni, and L. Colombo, Interpretation of ion-channeling spectra in ion-implanted Si with models of structurally relaxed defects and clusters, *Phys. Rev.* **B 69**, 165216 (2004).
- [50] G. Lulli, E. Albertazzi, M. Bianconi, and S. Balboni, Computer simulation of ion channeling in Si containing structurally relaxed point defects, *Nucl. Instr. Meth.* **B 211**, 50 (2003).

- [51] G. Lulli, E. Albertazzi, M. Bianconi, A. Satta, S. Balboni, L. Colombo, and A. Uguzzoni, Investigation of heavily damaged ion implanted Si by atomistic simulation of Rutherford backscattering channeling spectra, *Nucl. Instr. Meth.* **B 230**, 613 (2005).
- [52] S. Balboni, E. Albertazzi, M. Bianconi, and G. Lulli, Atomistic modeling of ion channeling in Si with point defects: The role of lattice relaxation, *Phys. Rev.* **B 66**, 045202 (2002).
- [53] A. Satta, E. Albertazzi, M. Bianconi, G. Lulli, S. Balboni, and L. Colombo, Atomistic simulation of ion channeling in heavily doped Si:As, *Nucl. Instr. Meth.* **B 230**, 112 (2005).
- [54] M. Bianconi, E. Albertazzi, S. Balboni, L. Colombo, G. Lulli, and A. Satta, Channeling characterization of defects in silicon: an atomistic approach, *Nucl. Instr. Meth.* **B 230**, 185 (2005).
- [55] K. Mok, M. Jaraiz, I. Martin-Bragado, J. Rubio, P. Castrillo, R. Pinacho, M. P. Srinivasan, and F. Benistant, Comprehensive modeling of ion-implant amorphization in silicon, *Mat. Sci. Eng.* **B 124-125**, 383 (2005).
- [56] K. Mok, M. Jaraiz, I. Martin-Bragado, J. Rubio, P. Castrillo, R. Pinacho, M. P. Srinivasan, and F. Benistant, Comprehensive modeling of ion-implant amorphization in silicon, *Mat. Sci. Eng.* **B 124-125**, 386 (2005).
- [57] K. Mok, M. Jaraiz, I. Martin-Bragado, J. Rubio, P. Castrillo, R. Pinacho, J. Barbolla, and M. P. Srinivasan, A physical model based on the amorphous pocket population, *J. Appl. Phys.* **98**, 046104 (2005).
- [58] I. Santos, L. A. Marqués, L. Pelaz, and P. Lopés, Molecular dynamics study of amorphous pocket formation in Si at low energies and its application to improve binary collision models, *Nucl. Instr. Meth.* **B 255**, 110 (2006).
- [59] E. Bogh, Defect studies in crystals by means of channeling, *Can. J. Phys.* **46**, 653 (1968).
- [60] D. A. Richie, J. Kim, S. A. Barr, K. R. A. Hazzard, R. Hennig, and J. W. Wilkins, Complexity of small silicon self-interstitial defects, *Phys. Rev. Lett.* **92**, 045501 (2004).
- [61] W. K. Leung, R. J. Needs, G. Rajagopal, S. Itoh, and S. Ihara, Calculations of silicon self-interstitial defects, *Phys. Rev. Lett.* **83**, 2351 (1999).
- [62] M. Kohayama and S. Takeda, First-principle calculations of the self-interstitial cluster I_4 in Si, *Phys. Rev.* **B 60**, 8075 (1999).

- [63] S. J. Clark and G. J. Ackland, Ab initio calculations of the self-interstitial in silicon, *Phys. Rev. B* **56**, 47 (1997).
- [64] N. Arai, S. Takeda, and M. Kohoyama, Self-interstitial clustering in crystalline silicon, *Phys. Rev. Lett.* **78**, 4265 (1997).
- [65] A. Bongiorno, L. Colombo, F. Cargnoni, C. Gatti, and M. Rossati, Evolution of energetics and bonding of compact self-interstitial clusters in silicon, *Europhys. Lett.* **50**, 608 (2000).
- [66] C. Z. Wang, C. T. Chan, and K. M. Ho, Tight-bonding molecular-dynamics study of defects in silicon, *Phys. Rev. Lett.* **66**, 189 (1991).
- [67] J. Kim, F. Kirchoff, J. Wilkins, and F. Khan, Stability of Si-defects: From point to extended defects., *Phys. Rev. Lett.* **84**, 503 (2000).
- [68] L. Colombo, Native defects and their interactions in silicon, *Physica B* **273-274**, 458 (1999).
- [69] R. J. Needs, First-principles calculations of self-interstitial defect structures and diffusion paths in silicon, *J. Phys. Condens. Matter* **11**, 10437 (1999).
- [70] L. Colombo, Tight-binding theory of native point defects in silicon, *Annu. Rev. Mat. Res.* **32**, 271 (2002).
- [71] R. Jones, T. A. G. Eberlein, N. Pinho, B. J. Coomer, J. P. Goss, P. R. Briddon, and S. Öberg, Self-interstitial clusters in silicon, *Nucl. Instr. Meth. B* **186**, 10 (2002).
- [72] M. Posselt, F. Gao, and D. Zwicker, Migration of di- and tri-interstitials in silicon, *Nucl. Instr. Meth. B* **228**, 212 (2005).
- [73] G. Götz and G. Sommer, Location of self-interstitial atoms in boron-implanted silicon by means of Rutherford backscattering of channeled ions, *Radiat. Eff.* **41**, 195 (1979).
- [74] B. Weber, E. Wendler, K. Gärtner, D. Stock, and W. Wesch, Investigation of weakly damaged $\langle 110 \rangle$, $\langle 111 \rangle$ and $\langle 100 \rangle$ silicon by means of temperature dependent dechanneling measurements, *Nucl Instr Meth B* **118**, 113 (1996).
- [75] D. Young, *Computational Chemistry: A Practical Guide for Applying Techniques to Real World Problems*, Wiley-Interscience, New-York, USA, 2001.
- [76] P. Hohenberg and W. Kohn, Inhomogeneous electron gas, *Phys. Rev.* **136 B**, 864 (1964).
- [77] D. Kovač and G. Hobler, Investigation of the impact of defect models on Monte Carlo simulations of RBS/C spectra, *Nucl. Instr. Meth.* **249**, 776 (2006).

- [78] G. Hobler and G. Kresse, Ab-initio calculations of the interaction between native point defects in silicon, *Mater. Sci. Eng.* **B 124/125**, 368 (2005).
- [79] G. Kresse and J. Furthmüller, Efficient iterative schemes for ab initio total-energy calculations using a plane-wave basis set, *Phys. Rev. B* **54**, 11169 (1996).
- [80] G. Kresse and J. Furthmüller, Efficiency of ab-initio total energy calculations for metals and semiconductors using a plane-wave basis set, *Comput. Mater. Sci.* **6**, 15 (1996).
- [81] M. Robinson and I. Torrens, Computer simulation of atomic-displacement cascades in solids in the binary-collision approximation, *Phys. Rev.* **B 9**, 5008 (1974).
- [82] J. F. Ziegler, J. P. Biersack, and U. Littmark, *The Stopping and Range of Ions in Solids*, Pergamon Press, New York, 1985.
- [83] M. Posselt, Computer simulation of channeling implantation at high and medium energies, *Nucl. Instr. Meth.* **B 80/81**, 28 (1993).
- [84] K. Gärtner et al., Round robin computer simulation of ion transmission through thin crystalline layers, *Nucl. Instr. Meth.* **B 102**, 183 (1995).
- [85] G. Hobler and G. Fehlmann, A study of ultra-shallow implanted dopant profiles in silicon using BC and MD simulations, *Radiat. Eff. Def. Sol.* **141**, 113 (1997).
- [86] G. Hobler and G. Betz, On the useful range of application of molecular dynamics simulations in the recoil interaction approximation, *Nucl. Instr. Meth.* **B 180**, 203 (2001).
- [87] K. Nordlund, Molecular dynamics simulation of ion ranges in the 1-100 keV energy range, *Comp. Mat. Sci.* **3**, 448 (1995).
- [88] T. D. de la Rubia and G. H. Gilmer, Structural transformations and defect production in ion implanted silicon: A molecular dynamics simulation study, *Phys. Rev. Lett.* **74**, 2507 (1995).
- [89] G. Otto, G. Hobler, and K. Gärtner, Defect characterization of low-energy recoil events in silicon using classical molecular dynamics simulation, *Nucl. Instr. Meth.* **B 202**, 114 (2003).
- [90] F. Stillinger and T. Weber, Computer simulation of local order in condensed phases of silicon, *Phys. Rev. B* **31**, 31 (1985).
- [91] K. Gärtner and K. Hehl, Theoretical description of elastic atom - atom scattering, *Phys. Stat. Sol.* **B 94**, 231 (1979).

- [92] J. Tersoff, Empirical interatomic potential for silicon with improved elastic properties, *Phys. Rev. B* **38**, 9902 (1988).
- [93] L. Verlet, Computer "experiments" on classical fluids. I. thermodynamical properties of Lennard-Jones molecules, *Phys. Rev.* **159**, 98 (1967).
- [94] A. Touzik, H. Hermann, and K. Wetzig, General-purpose distributed software for Monte Carlo simulations in materials design, *Comp. Mat. Sci.* **28**, 134 (2003).
- [95] G. Otto and G. Hobler, Coupled kinetic Monte Carlo and molecular dynamics simulations of implant damage accumulation in silicon, *Mat. Res. Soc. Symp. Proc.* **792**, R6.5.1 (2003).
- [96] T. Zahel, G. Otto, and G. Hobler, Atomistic simulation of hydrogen implantation for SOI wafer production, in *EUROSOI 2005, Book of Abstracts*, pages 35–36, Departamento de Electrónica de la Universidad de Granada, 2005.
- [97] T. Zahel, G. Otto, and G. Hobler, Atomistic simulation of the isotope effect on defect formation in H/D-implanted Si, in *Silicon-on-Insulator Technology and Devices XII*, edited by G. K. Celler, S. Cristoloveanu, J. G. Fossum, F. Gamiz, K. Izumi, and Y.-W. Kim, pages 179–184, The Electrochem. Soc., Pennington, 2005.
- [98] G. Carter, A nucleation and growth model for ion-bombardment induced phase changes in Si, *Vacuum* **49**, 337 (1998).
- [99] K. A. Jackson, A defect model for ion-induced crystallization and amorphization, *J. Mater. Res.* **3**, 1218 (1988).
- [100] G. Hobler, L. Pelaz, and C. S. Rafferty, Continuum treatment of spatial correlation in damage annealing, *Nucl. Instr. Meth.* **B 153**, 172 (1999).
- [101] O. W. Holland, C. W. White, M. K. El-Ghor, and J. D. Budai, MeV, self-ion implantation in Si at liquid nitrogen temperature; a study of damage morphology and its anomalous annealing behavior, *J. Appl. Phys.* **68**, 2081 (1990).
- [102] M.-J. Caturla, T. D. de la Rubia, and G. H. Gilmer, Point defect production, geometry and stability in silicon: A molecular dynamics simulation study, in *Mat. Res. Soc. Symp. Proc.*, volume 316, pages 141–146, MRS, Pittsburgh, 1994.
- [103] W. Windl, T. J. Lenosky, J. D. Kress, and A. F. Voter, First-principles investigation of radiation induced defects in Si and SiC, *Nucl. Instr. Meth.* **B 141**, 61 (1998).
- [104] I. Santos, L. A. Marqués, L. Pelaz, P. Lopés, M. Aboy, and J. Barbolla, Molecular dynamics characterization of as-implanted damage in silicon, *Mat. Sci. and Eng.* **B 124-124**, 372 (2006).

- [105] M. Y. Tsai and B. G. Streetman, Recrystallization of implanted amorphous silicon layers. i. electrical properties of silicon implanted with BF_2^+ or $Si^+ + B^+$ implants, J. Appl. Phys. **50**, 183 (1979).
- [106] D. Kovač, G. Otto, and G. Hobler, Modeling of amorphous pocket formation in silicon by numerical solution of the heat transport equation, Nucl. Instr. Meth. **B 228**, 226 (2005).
- [107] J. R. Dennis and E. B. Hale, Crystalline to amorphous transformation in ion-implanted silicon: a composite model, J. Appl. Phys. **49**, 1119 (1978).
- [108] G. H. Vineyard, Thermal spikes and activated processes, Radiation Effects **29**, 245 (1976).
- [109] H. Hensel and H. Urbassek, Implantation damage under low-energy Si self-bombardment, Phys Rev. B **B 57**, 4756 (1998).
- [110] I. Santos, L. A. Marqués, and L. Pelaz, Modeling of damage generation mechanisms in silicon at energies below the displacement threshold, Phys. Rev. B **74**, 174115 (2006).
- [111] M. Chester, Second sound in solids, Phys. Rev. **131**, 2013 (1963).
- [112] J. M. Haile, *Molecular Dynamics Simulations*, John Wiley and Sons, New York, 1992.
- [113] M. N. Ozisik, *Heat Conduction*, John Wiley and Sons, New York, 1993.
- [114] P. J. Antaki, Solution for non-Fourier dual phase lag heat conduction in a semi-infinite slab with surface heat flux, Int. J. Heat Mass Transfer **41**, 2253 (1998).
- [115] H. S. Carslaw and J. C. Jaeger, *Conduction of heat in solids*, Oxford scientific publications, 1995.
- [116] D. C. Rapaport, *The Art of Molecular Dynamics Simulation*, Cambridge University Press, 2002.
- [117] M. Levinstein, S. Rumyantsev, and M. Shur, *Handbook Series on Semiconductor Parameters*, World Scientific Publishing Co. Pte. Ltd., 1996.
- [118] J. Philibert, *Atom movements : Diffusion and mass transport in solids*, Les Éditions de physique, France, 1991.
- [119] J. P. Stark, *Solid State Diffusion*, John Wiley and Sons, New York, 1976.
- [120] R. F. Wood and G. E. Giles, Macroscopic theory of pulsed-laser annealing. I. thermal transport and melting, Phys. Rev. B **23**, 2923 (1981).

- [121] P. Sigmund, On the number of atoms displaced by implanted ions or energetic recoil atoms, *Appl. Phys. Lett.* **14**, 114 (1969).
- [122] J.-Y. Cheng and J. M. Gibson, A damage model for disordered structures in ion irradiated silicon, *Mat. Res. Soc. Symp. Proc.* **647**, O14.1.1 (2001).
- [123] N. A. Marks, Evidence for subpicosecond thermal spikes in the formation of tetrahedral amorphous carbon, *Phys. Rev. B* **56**, 2441 (1997).
- [124] C. Cattaneo, Sur une form de l'équation de la chaleur éliminant le paradoxe d'une propagation instantanée, *C. R. Acad. Sci.* **247**, 431 (1958).
- [125] P. Vernotte, Les paradoxes de la theorie continue de l'équation de la chaleur, *C. R. Acad. Sci.* **246**, 2103 (1958).
- [126] S. Volz, J. Saulnier, M. Lallemand, B. P. adn P. Depondt, and M. Mareschal, Transient fourier-law deviation by molecular dynamics in solid argon, *Phys. Rev. B* **54**, 340 (1996).
- [127] D. W. Tang and N. Araki, Non-fourier heat conduction in a finite medium under periodic surface thermal disturbance, *Int. J. Heat Mass Transfer.* **39**, 1585 (1996).
- [128] A. Haji-Sheikh, W. J. Minkowycz, and E. M. Sparrow, Certain anomalies in the analysis of hyperbolic heat conduction, *Journal of Heat Transfer* **124**, 307 (2002).
- [129] S. Moon, M. Hatano, M. Lee, and C. P. Grigoropoulos, Thermal conductivity of amorphous silicon thin films, *Int. J. of Heat and Mass Trans.* **45**, 2439 (2002).
- [130] Z. Zhou, S. Mukherjee, and W.-K. Rhim, Measurement of thermophysical properties of molten silicon using an upgraded electrostatic levitator, *J. of Crystal Growth* **257**, 350 (2003).
- [131] E. Yamasue, M. Susa, H. Fukuyama, and K. Nagata, Thermal conductivities of silicon and germanium in solid and liquid states measured by non-stationary hot wire method with silica coated probe, *Jour. of Crystal Growth* **234**, 121 (2002).
- [132] H. V. Swygenhoven and A. Caro, Nanoscale phase transitions induced by heat spikes in collision cascades, *Phys. Rev. Lett.* **70**, 2098 (1993).
- [133] G. B. Arfken and H. J. Weber, *Mathematical methods for physicist: Fourth Edition*, Academic Press, San Diego, USA, 1995.
- [134] W. H. Press, S. A. Teukolsky, W. T. Vetterling, and E. Brian P. Flannery, *Numerical Recipes*, Cambridge University press, New York, 1992.
- [135] R. Hull, editor, *Properties of Crystalline Silicon*, INSPEC, London, United Kingdom, 1999.

- [136] D. Maroudas, M. E. Barone, and B. Meng, Atomic-scale simulation of defect-induced amorphization of crystalline silicon, *Electrochem. Soc. Proc.* **4**, 387 (1996).
- [137] D. S. Gemmell, Channeling and related effects in the motion of charged particles through crystals, *Rev. of Modern Phys.* **46**, 129 (1974).
- [138] W. K. Chu, J. W. Mayer, and M. A. Nicolet, *Backscattering Spectrometry*, Academic Press, 1978.
- [139] J. R. Tesmer and M. Nastasi, *Handbook of Modern Ion Beam Materials Analysis*, Materials Research Society, Pittsburg, Pennsylvania, 1995.
- [140] P. E. J. Flewitt and R. K. Wild, *Physical Methods for Material Characterization*, Institute of Physics Publishing, London, 1994.
- [141] A. Stonert, A. Turos, L. Nowicki, and B. Breeger, Analysis of defects in multicomponent crystals by ion channeling, *Nucl. Instr. Meth.* **B 161-163**, 496 (2000).
- [142] A. Kling, H. Krause, R.-H. Flagmeyer, J. Vogt, and T. Butz, Channeling investigations of MeV Zn implanted InP, *Nucl. Instr. Meth.* **B 96**, 302 (1995).
- [143] C. Cohen and D. Dauvergne, High energy ion channeling. principles and typical applications, *Nucl. Instr. Meth.* **B 225**, 40 (2004).
- [144] A. Das and T. Ferbel, *Introduction to Nuclear and Particle Physics*, World Scientific, 2003.
- [145] L. Shao and M. Nastasi, Methods for the accurate analysis of channeling Rutherford backscattering spectrometry, *Appl. Phys. Lett.* **87** (2005).
- [146] J. H. Barrett, Monte Carlo channeling calculations, *Phys. Rev.* **B 3**, 1527 (1971).
- [147] T. Fuse, O. Ishiyama, M. Shinohara, and Y. Kido, Monte Carlo simulation of angular-scan spectra for coaxial impact collision ion scattering spectroscopy (CASSIS), *Surface Science* **372**, 350 (1997).
- [148] A. Kling, Cassis - a new Monte-Carlo computer program for channeling simulation of RBS, NRA and PIXE., *Nucl. Instr. Meth.* **B 102**, 141 (1995).
- [149] G. Lulli, E. Albertazzi, M. Bianconi, G. G. Bentini, R. Nipoti, and R. Lotti, Determination of the electronic energy loss in crystalline Si by Monte-Carlo simulation of Rutherford backscattering-channeling spectra, *Nucl. Instr. Meth.* **B 170**, 1 (2000).
- [150] R. Smith, M. Jakas, D. Ashworth, B. Owen, and M. Bowyer, *Atomic and ion collisions in solids and at surfaces*, Cambridge University Press, 1997.

- [151] M. Mayer, *SIMNRA*, Max-Planck-Institut für Plasmaphysik, Garching, Germany, 2006.
- [152] J. L'Ecuyer, J. A. Davies, and N. Matsunami, How accurate are absolute Rutherford backscattering yields, *Nucl. Instr. Meth.* **160**, 337 (1979).
- [153] H. H. Andersen, F. Besenbacher, P. Loftager, and W. Möller, Large-angle scattering of light ions in the weakly screened Rutherford region, *Phys. Rev. A* **21**, 1891 (1980).
- [154] A. F. Gurbich, Evaluation of non-Rutherford proton elastic scattering cross section for silicon, *Nucl. Instr. Meth.* **B 145**, 578 (1998).
- [155] M. Bozoian, A useful formula for departures from Rutherford backscattering, *Nucl. Instr. Meth.* **B 82**, 602 (1979).
- [156] G. Hobler, Critical angles and low-energy limits to ion channeling in silicon, *Radiat. Eff. Def. Sol.* **139**, 21 (1996).
- [157] P. Bauer, E. Steinbauer, and J. P. Biersack, Rutherford backscattering beyond the single scattering model, *Nucl. Instr. Meth.* **B 79**, 443 (1993).
- [158] W. Eckstein and M. Mayer, Rutherford backscattering from layered structures beyond the single scattering model, *Nucl. Instr. Meth.* **B 153**, 337 (1999).
- [159] J. Tersoff, Empirical interatomic potential for carbon, with applications to amorphous carbon, *Phys. Rev. Lett.* **61**, 2879 (1988).

List of Publications

G. Hobler, D. Kovač, G. Otto, L. Palmetshofer, K. Mayerhofer, K. Piplits, "Multiscale approach for the analysis of channeling profile measurements of ion implantation damage", Nucl. Instr. Meth. B 228, p.360, 2005.

D. Kovač, G. Otto, G. Hobler, "Modeling of amorphous pocket formation in silicon by numerical solution of the heat transport equation", Nucl. Instr. Meth. B 228, p.226, 2005.

G. Otto, D. Kovač, G. Hobler, "Coupled BC/kLMC simulations of the temperature dependence of implant damage formation in silicon", Nucl. Instr. Meth. B 228, p.256, 2005.

D. Kovač, G. Hobler, "Investigation of the impact of defect models on Monte Carlo simulations of RBS/C spectra", Nucl. Instr. Meth. B 249, p.776, 2006.

D. Kovač, G. Hobler, L. Palmetshofer, "Amorphous pocket model based on the modified heat transfer equation and local lattice collapse", to be published.

Curriculum Vitae

11. 8. 1977 born in Foča, Bosnia and Herzegovina
- 1984 - 1992 Elementary school in Foča
- 1992 - 1996 Gymnasium in Foča
20. 6. 1996 Matriculation
- 1996 - 2003 Faculty of Electrical Engineering at the University of Belgrade
16. 6. 2003 Dipl. Ing. title in the field of Telecommunication
Title of the diploma thesis “Ultrafast nonlinear
processes in Semiconductor Optical Amplifiers”
1. 12. 2003 - PhD studies at the Solid State Electronics Institute
at the Vienna University of Technology
- Title of the thesis ”Multiscale Modeling
of Ion Implantation Damage in Silicon”